1-2022

Fluid structure interactions within a common rail diesel injector.

Russell Prater
University of Louisville

FLUID STRUCTURE INTERACTIONS WITHIN A COMMON RAIL DIESEL INJECTOR

By

Russell Prater
M.S. Eng., University of Louisville,

A Dissertation
Submitted to the Faculty of the
University of Louisville
J.B. Speed School of Engineering
in Partial Fulfillment of Requirements
for the Professional Degree

Doctor of Philosophy
in Mechanical Engineering

Department of Mechanical Engineering
University of Louisville
Louisville, Kentucky
May, 2022

FLUID STRUCTURE INTERACTIONS WITHIN A COMMON RAIL DIESEL INJECTOR

By

Russell Prater
B.A, University of Louisville, 2011
M.S., University of Louisville, 2011

A Dissertation Approved on

April 24, 2022

by the following Dissertation Committee:

_____
Dr. Yongsheng Lian, Thesis Director
Mechanical Engineering

_____
Dr. Bersen
Chemical Engineering

_____
Dr. Bradshaw
Mechanical Engineering

_____
Dr. Brehob
Mechanical Engineering

_____
Dr. Frank Husmeier
Cummins Fuel Systems

DEDICATION

This Dissertation is dedicated to my daughter Wren Coraline Prater.

ACKNOWLEDGMENTS

I would like to thank my advisor Dr. Lian for his guidance, patience and never giving up on me. I would like to thank my other committee members for patience and assistance with this work. I would like to thank Frank for being a mentor and a friend. I would like to thank my wife Becca and my daughter Wren both of whom provided the strength to finish this work.

ABSTRACT

FLUID STRUCTURE INTERACTIONS WITHIN A COMMON RAIL DIESEL INJECTOR

Russell B. Prater

April 24, 2022

The internal flow of a high-pressure diesel injector is simulated numerically to investigate the complex transient flow structures and the unsteady forces imparted to the injector needle that result from the asymmetric flow fields developed during operation. The gas-liquid two phase flow is simulated using a mixture model with the cavitation numerically modeled using the Zwart-Gerber-Belamri model. Both the k-ε model and the detached eddy simulation (DES) model are used, and the numerical results are compared. This dissertation looks at the internal flow of a generic injector at different lifts and characterizes the flow parameters at high lift and low lifts. This paper shows that the DES model captures the important unsteady flow features missed by the k-ε model. A DES simulation of a dual gain orifice injector is performed and the impact of a unique vortical structure that is generated by the gain orifices on the flow characteristics is discussed. The fluid-structure interactions of an injector at hover are simulated and the behavior of this injector and the impact of the resulting lateral bending motion of the needle is discussed. This paper identifies the geometric feature that creates the asymmetrical flow that leads to the bending motion. In the final portion of this dissertation the fluid-structure interactions are simulated over the entire injection cycle. This dissertation discusses how the bending motion of the needle is initiated and develops over the injection cycle and discusses the impact of this motion on the fuel quantity injected and the vapor formed during operation by comparing the FSI simulation to a simulation where the lateral motion is artificially limited.

TABLE OF CONTENTS

Page

ABSTRACT v
LIST OF TABLES vii
LIST OF FIGURES ix
I. INTRODUCTION 1
Background 1
Objectives 5
II. FLUID SOLVER NUMERICAL METHODS 6
Navier-Stokes System of Equations 6
Solving the Navier Stokes equations 8
Cavitation Models 13
III. TURBULENCE MODELS 19
RANS Turbulence Models 19
LES Turbulence Models 22
DES TURBULENCE Model 24
IV. STRUCTURAL SOLVER 26
Equations of motion 26
Solid Contact Modeling 28
Needle Lift Profile 29
Coupling Method 30
V. GRID UPDATE METHODS 33
Smoothing Methods 33
Remeshing Methods 34
VI. CODE VALIDATION 36
Numerical Code Validation 36
Spatial Sensitivity 37
Temporal 39

VII. STEADY STATE RESULTS 40
Simulation Settings 40
Low Lift Results 43
High Lift Results 48
Low and High Lift Comparison 53
VIII. TRANSIENT HOVERING RESULTS 57
Surface 1 Lateral Forces 64
Surface 2 and 3 Lateral Forces 66
Spray Hole Vapor 66
Outlet Mass Flow Rates 69
IX. FSI SIMULATION AT HOVER 70
Vertical Compression 73
Lateral Displacement 74
Mass Flow Rates 81
Vapor Volume Fraction 84
X. FSI SIMULATION INCLUDING OPENING AND CLOSING NEEDLE MOTION 88
Motion Profile 88
lateral motion 91
mass flow rate 101
vapor volume 112
XI. CONCLUISONS 119
REFERENCES 121
APPENDICES 127
CURRICULUM VITA 129

LIST OF TABLES

TABLE PAGE

1. Sphere Simulation Summary 36
2. Force Amplitude for Grid sensitivity Analysis. 37
3. Summation of the magnitudes of the deviation from the center for the inception points at the points shown in Figure 33. 62

LIST OF FIGURES

FIGURE PAGE

1. Recent Emission Standards (Source: Cummins Emission Solutions) 1
2. Schematic of the tip of the fuel injector....3
3. Cell Centered Staggered Grid....8
4. SIMPLEC algorithm procedure [48] 12
5. Phase diagram with cavitation and boiling processes[49] 13
6. Visualization of the different DES Regions[75]....24
7. Surfaces that can come into contact during the bending motion 28
8. Two surfaces a) not in contact and b) in contact (Ansys Theory) 29
9. Lift profile for the vertical needle motion....29
10. Non-matching interface[81]....30
11. Vertex distance to boundaries. [48] 34
12. Size function interpolation. [48] 35
13. Locations for the bottom three surfaces of the injector needle....37
14. Lateral force magnitudes on surface 3 from the temporal sensitivity analysis....39
15. The injector with dual gain orifices and the sac. A) The injector body with the needle darkened. B) Zoomed in view of the sac with pressure outlets. The lift is defined as the vertical distance of the needle tip between its highest and lowest position. 41
16. Low Lift Pressure....44
17. Low Lift Velocity Contours....45
18. Low Lift Streamlines 46
19. Low Lift Vapor Volume Fraction....47
20. Lift Vs. Pressure....48
21. High Lift Pressure....49
22. High Lift Velocity Contours....50
23. High Lift Vapor Volume Fraction 51
24. High Lift Stream Lines 52
25. Average Spray Hole Velocity vs. Lift....53
26. Mass Flow Rate vs. Lift....53

27. Total Lift Force vs. Lift 54
28. Bottom Surfaces Lift Forces vs. Lift.....54
29. Top Surfaces Lift Forces vs. Lift 55
30. Sac Vapor Volume vs. Lift 55
31. Spray Hole Vapor Volume vs. Lift 56
32. Comparison of the lateral force for the DES and RANS simulations on a) surface 1 and b) the summation over all the surfaces.....57
33. Lateral force history on the needle tip with points marked for figure 12 58
34. Pressure contours on surface 1 showing the correlation between the offset inception point and the lateral force magnitude in the DES and RANS simulations. For these simulations the inception point predicted using the RANS turbulence model deviates much less from the center than in the DES simulation. 59
35. RANS and DES comparison of the lifting force on surface 1 show that the DES simulation predicts a lower lifting force due to the lower minimum pressure 60
36. Comparison of iso-surface of the Q criteria (>0.01) between the DES and RANS at time instances of a) high lifting force, b) middling lifting force and c) minimum lifting force with the orientations marked for spray hole 1 and 5. The greyscale is based on the vorticity magnitude. 61
37. Out of Plane Vorticity Magnitude showing the persistent vertical axis of rotation in the RANS simulation that is not present in the DES simulation
38. Comparison between the lateral force in the RANS and DES for surfaces 2 and 3 63
39. Comparison between the lateral force in the RANS and DES for surfaces 2 and 3 with a moving average window of 2.5 microseconds applied to the DES simulation.....64
40. Comparison between the lateral forces on surfaces 2 and 3 and the swirling speed inside the sac showing that the swirling speed is proportional to the magnitude of the force 64
41. Comparison between the vapor generated in a single spray hole in the DES and RANS simulations. From this graph it was determined that there is no significant difference between the predicted vapor generation. 65
42. Vapor Volume in spray holes 1 and 3 and 5 for the DES simulation. 66
43. Vapor volume within spray holes on opposite sides of the sac over a singular peak with markers indicating the time instances used for figure 18 67
44. Side-by-side plots of the velocity and vapor volume fraction at time instances indicated in figure 18 showing fluctuations in the vapor volume as the vortical rollup passes over the spray hole. 68
45. Vapor Volume and Mass Flow Rate for spray hole 1 in the DES simulation showing an inverse relationship between the two flow variables 69
46. Unbalanced injector gain orifice. 70

47. Comparison of the forces in line with the gain orifice (X-direction) and perpendicular to the gain orifice (Z-direction) on surfaces a) 3 and b) 6. On both surfaces the magnitude of the forces are much larger in the x direction. 71
48. Boundary conitions imposed on the points in the XY plane. 72
49. Vertical displacment measured at the injector tip over the full cycle. 73
50. Vertical displacement measured at the injector tip over the full cycle 73
51. Lateral displacement measured at the tip over the full cycle. 74
52. Displacement of the needle compared to the undeformed wire frame at a 1x scale. 74
53. Displacement of the needle compared to the undeformed wire frame at a 5x scale. 75
54. Diagram showing the locations of surfaces 4-6. 76
55. Force in the X direction on surface 1. 77
56. Force in the X direction on surface 2. 77
57. Force in the X direction on surface 3. 78
58. Force in the X direction on surface 4. 78
59. Force in the X direction on surface 5. 79
60. Force in the X direction on surface 6. 79
61. Unfiltered mass flow rate for spray hole 1 81
62. Filtered mass flow rate for spray hole 1 compared with the distance between the tip and the center of the spray hole entrance 82
63. Filtered mass flow rate for spray hole 5 compared with the distance between the tip and the center of the spray hole entrance 82
64. Comparison between the mass flow rate out of spray hole 1 with and without the structural displacement. 83
65. Comparison between the mass flow rate out of spray hole 5 with and without the structural displacement. 83
66. Vapor volume fraction for spray hole 3, which is perpendicular to the needle motion, with and without the needle motion. 84
67. Vapor volume fraction for spray hole 7, which is perpendicular to the needle motion, with and without the needle motion. 85
68. Vapor volume fraction for spray hole 5, which is in the plane of the needle motion, with and without the needle motion. 85
69. Vapor volume fraction for spray hole 1, which is in the plane of the needle motion, with and without the needle motion. 86
70. Sac flow without the structural displacement. 86
71. Sac flow with the needle bent away from spray hole 5. 87

72. Vapor volume fraction a) without structural displacements and b) with structural displacement. With the displacement the separation height is reduced decreasing the amount of vapor formed. The flow from the bottom of the sac into the spray hole creates additional vapor on the bottom of the spray hole. 87
73. Needle position at a) low lift and b) high lift....89
74. Extreme of lateral displacement from needle bending 89
75. Vertical and lateral displacement of the needle tip during the injection cycle 91
76. Force in the x direction and the tip Displacement during the initial portion of the injection cycle 93
77. Pressure contour at the initial opening of the needle 93
78. Velocity contour at the initial opening of the needle....94
79. Pressure contour at a low lift when the needle is deflected to one side.....95
80. Velocity contour at the midpoint of surface 3 at 95
81. Mass flow rate versus needle lift. 96
82. Pressure contour at a high lift when the needle is biased to one side. 97
83. Velocity contour at the midpoint of surface 3 at a high lift 98
84. Forces on surfaces 1-6 over the entire injection cycle.....99
85. Forces on needle surfaces 1-3 with and without the lateral motion simulated. 100
86. Total Mass flow rate with and with the lateral motion 101
87. Percentage change of the mass flow rate when the lateral motion is simulated.....102
88. Individual spray hole mass flow rates with and without lateral motion 106
89. Percentage of excess mass flow rate for individual spray holes. 111
90. Tip distance measurement at two different time steps....112
91. Spray hole vapor with and without lateral motion and the tip distance for spray holes 1-8. 116
92. Vapor formation at hover with a) the needle centered b) offset 118

I. INTRODUCTION

A. Background

Modern diesel engines are capable of running efficiently, generating large amounts of power while meeting emissions and mileage regulations that are much more stringent than those of just a few years ago (Figure 1). These improvements are due to advances in techniques such as turbocharging, exhaust gas recirculation (EGR), charge air cooling and an advanced fuel injection systems that can operate on over periods as short as a millisecond while delivering precisely metered fuel to the combustion chamber [1]. The injector plays an important role in reducing emissions during operation, however, it is difficult to pinpoint the contribution of each variable due to the large number of geometric, and fluid parameters that affect combustion [2]. Emission formation rates are determined by the local temperature during combustion [3] which is highly dependent on the spray pattern that is determined by the injector geometry, fuel properties, needle motion, rate shapes, and injection pressure [4-6] [7-9].

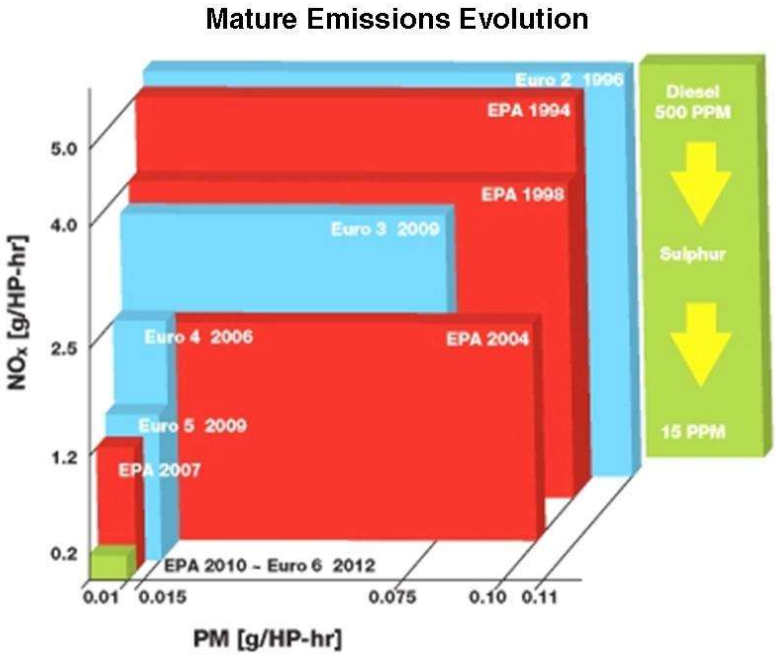

Figure 1. Recent Emission Standards (Source: Cummins Emission Solutions)

Low speed flow studies by Chaves [10] and Hiroyasu [11] of real sized injectors have shown that the internal geometry of the injector has a significant influence on the inception point and the size of the cavitation zones within the flow which in turn influences the spray pattern. Scaled-up fuel injectors have been used to investigate the role cavitation has on the spray [12] and have shown that cavitation is beneficial to spray dispersion and fuel jet break-up which increases spray atomization [10], and promotes better mixing of fuel and oxygen in the combustion chamber leading to a more efficient and complete combustion process [13-15]. Studying the internal flow of real-sized injectors remains difficult because the flow operates on small temporal and spatial scales and exists as a two-phase flow which is difficult to observe experimentally at scales adequate to observe all the relevant flow features. Scaled-up injector studies are problematic because the Reynolds number, Weber number, and Cavitation number, all of which affect the spray pattern [16], cannot be matched simultaneously. Additionally scaled and non-scaled injector studies are not completely analogous because the inception of cavitation is heterogeneous and along the wall [17] but in scaled-up injectors the cavitation is caused by the bulk flow homogenous nucleation [16, 18]. Owing to these issues the life and residence time of the cavitated flow, which depend on the local pressure, have yet to be matched for large scale injectors [19, 20].

The advancement in both computers and numerical algorithms has made it feasible to perform injector studies that are currently impossible to replicate experimentally. Previous numerical studies of the inception of cavitation in the sac and spray holes (Figure 2) have found that internal geometry affects the both the size and location of the cavitation zones [21-26]. Other numerical studies [27, 28] have shown that the region of significant cavitation shifts from the top of the orifice to the bottom as the needle position changes from fully open to nearly closed. The presence of cavitation can cause large variations in the mass flow rates out of the spray holes [29] and can lead to a Kelvin-Helmholtz instability throughout the entire spay hole length [30] and contribute to fluctuating flow characteristics.

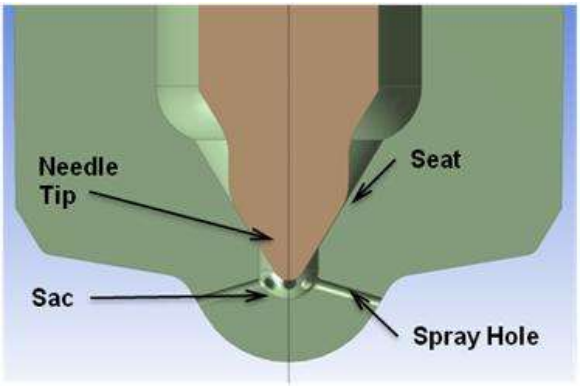

Figure 2. Schematic of the tip of the fuel injector

These numerical studies usually do not consider the transient lateral movement of the injector needle which has been observed in high speed x-ray studies and can significantly alter the flow pattern into the sac playing a role in the evolution of the cavitation zones within a diesel injector [31]. Kilic et al. [32] have shown that when the needle is off-center there are large variations in the flow velocity through different holes which leads to asymmetrical spray penetration. Additional studies have shown [33, 34] that the needle motion changes the flow structures within the sac which create hole to hole variations that vary with the motion of the needle.

While the presence of the lateral needle motion has been observed, the underlying mechanism and its impact on hole-to-hole variations are not well understood. Study of this problem involves addressing several challenges. The model needs to resolve the flow on very small spatial and temporal scales in order to accurately resolve both the formation and dissipation of the cavitated flow and the resultant Kelvin-Helmholtz instability [30] that and contributes to the fluctuating flow characteristics. The high supply pressure of the fuel injector often causes highly unsteady turbulent internal flows with velocities on the order of hundreds of meters per second [35] and a Reynolds number that varies between 0 and 20,000 [36]. Additionally RANS simulations often under-predict the maximum amplitudes in force fluctuations and miss high frequency fluctuations in the forces [37, 38] and transient fluctuations of the vapor formation [39] which dictates the use of a higher fidelity turbulence model in order to capture the needle forces driving the lateral motion.

This dissertation numerically looks at the transient forces that act on the injector needle as well as the geometric influence of the gain orifice. Pure RANS simulations were ran but they fail to capture the transient flow features of the internal flow which has been

observed before by Payri et al. [39]. This paper used a hybrid DES model to resolve the flow because the size of the model is prohibitive to using a full LES simulation. The DES model resolved transient flow features not evidenced in the RANS simulations, these differences in the internal flow patterns lead to differences on the order of a magnitude in the lateral forces predicted by the solver. This dissertation shows that RANS turbulence models under predict the lateral forces that act on the needle and don't capture the transient changes in the location of the cavitation zone. Additionally, this paper shows that the gain orifice plays a significant role in creating the internal flow and the flow balanced injector creates a swirling motion that leads to higher lateral forces that exhibit a sinusoidal trend. The non-flow balanced orifice creates a unidirectional force imbalance during operation. A coupled fluid-structure simulation is run on an injector both at hover and undergoing the entirety of an injection cycle. The simulation at hover was able to match experimental lateral displacements and the frequency of these fluctuations. This dissertation discusses the way that these fluctuations impact the mass flow rates for the individual spray holes as well as the vapor formation within the spray holes. This data was compared to simulations that were run without structural deformations and it was concluded that the motion of the needle at hover was insufficient to cause significant variations in most of the spray holes. The exception was the spray hole that the needle bent towards. This spray hole exhibits a decrease in the vapor generated due to the change in how the flow enters this spray hole. This dissertation discusses in detail the changes in the flow field entering the spray hole caused by the needle deflection.

B. Objectives

This dissertation numerically studies the flow features within a diesel injector over the full sweep of the lifts experienced during normal operation. The flow features are investigated and tied to the lifting forces developed during operation, the vapor formation that can lead to cavitation damage over the injector's lifetime, and fuel delivery during nominal operation. This dissertation then looks at the transient behavior of the injector during the hover phase of the injection event. The lateral forces that act on the needle are examined and their dependence on the flow fields that are developed due to the orientation and geometry of the gain orifice are determined. The results indicate that the single gain orifice tends to limit the magnitude of the lateral forces developed when compared to the dual gain orifice needle. Finally, this dissertation looks at the motion of an injector needle over an entire injection cycle. The source of the transient lateral motion is identified, and the resulting flow characteristics are compared to an injection cycle where the lateral motion is artificially restricted in order to isolate the impact of the lateral motion on the mass flow rates and vapor formation.

II. FLUID SOLVER NUMERICAL METHODS

A. Navier-Stokes System of Equations

The equations which model the fluid flow are derived from the equations for the conservation of mass and momentum. The vector form of the continuity equation describes the time rate of change of the mass of a system as

$$\frac{\partial \rho}{\partial t} + \nabla \cdot \left(\rho \vec{u} \right) = 0 \tag{1}$$

where ρ is the fluid density, $\vec{u}$ is the fluid velocity.

$$\frac{\partial}{\partial t}\left(\rho \vec{u} \right) + \nabla \cdot \left(\rho \vec{u} \vec{u} \right) = -\nabla P + \mu \nabla^2 \vec{u} \tag{2}$$

The equation 2 can be expressed as by a general differential equation in the form of

$$\frac{\partial \left(\rho \phi \right)}{\partial t} + \nabla \cdot \left(\rho \vec{u} \phi \right) = \nabla \cdot \left(\Gamma \nabla \phi \right) + q_\phi \tag{3}$$

where ϕ is any dependent variable, Γ is the diffusion coefficient, and q_ϕ is the source term for variable ϕ. Discretization of this equation over a control volume yields

$$A_{i,j}^{\phi} \phi_{i,j} = \sum A_{nb}^{\phi} \phi_{nb} + b_{i,j} \tag{4}$$

where the coefficient A represents the coefficient governing the algebraic dependence of the variable ϕ at the cell (i, j) and the neighbors (nb) and the term b represents the local source term for ϕ. The momentum equations are discretized in the form of equation 5 as

$$A_{i,j}^{u} \vec{u}_{i,j} = \sum A_{nb}^{u} \vec{u}_{nb} + b^{\vec{u}}{}_{i,j} - V(\nabla P) \tag{5}$$

where V is the volume of cell (i, j). This can be simplified to notion used by Moukalled et al. [40] that gives equation 13 as

$$\vec{u}_{i,j} - H\left[\vec{u} \right]_{i,j} = -D_{i,j} \left(\nabla P \right)_{i,j} \tag{6}$$

where

$$H\left[\phi\right] = \frac{\sum A_{nb}^{\phi}\phi_{nb} + b_{i,j}}{A_{i,j}^{\phi}}$$

$$D_{i,j} = \begin{bmatrix} \frac{V}{A_{i,j}^{u}} & 0 \\ 0 & \frac{V}{A_{i,j}^{v}} \end{bmatrix} \tag{7}$$

$$\left(\nabla P\right)_{i,j} = \frac{1}{V}\int_{V} \nabla P dV$$

The continuity equation is expressed in terms of surface fluxes using the divergence theorem as

$$\frac{\partial \rho_{i,j}}{\partial t}\vec{u}_{i,j} + \Delta\left[\rho\vec{u}\cdot S\right]_{i,j} = 0 \tag{8}$$

where the first term represents the time variance of the density multiplied by the local velocity and second term represents the density change due to the facial velocities. The velocities at the faces are generated by selectively interpolating terms in equation 6 to generate

$$\vec{u}_{f} - \bar{H}\left[\vec{u}\right]_{f} = -\bar{D}_{f}\left(\nabla P\right)_{f} \tag{9}$$

where an over bar represents an averaged value between two adjacent cell centers between facial surface f.

B. Solving the Navier Stokes equations

For this study the Navier-Stokes equations and the continuity equations are solved using the SIMPLEC algorithm[41], which is a modification of the SIMPLE algorithm [42, 43]. It uses a segregated predictor corrector that couples together the velocity, pressure and density through the continuity and momentum equations using an iterative predicator-corrector method. In these algorithms the velocity fields are initially predicted using the corrected pressures from the previous iteration. In the corrector step a pressure correction is derived and used to update the pressures. These steps are repeated iteratively to drive the velocity, density and pressure terms to a converged state that satisfies the momentum and continuity equations. The algorithms make use of cell centered staggered grids (Figure 3) developed by Rhie and Chow[44] and extended by Zang et al[45] to incorporated compatibility with 3-D time dependent problem formulations.

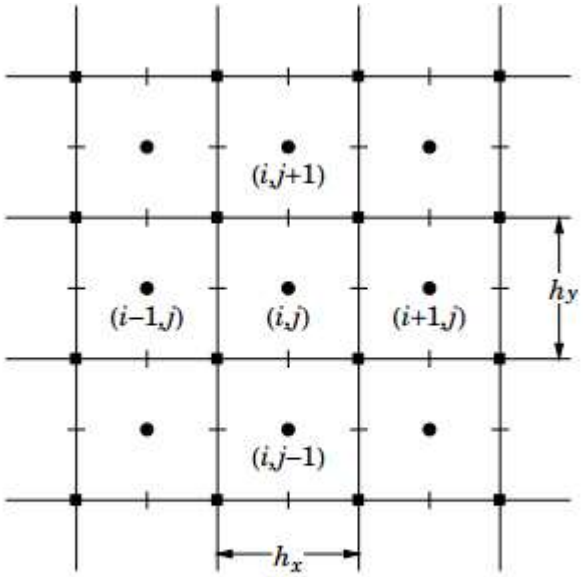

Figure 2.12: Cell-centered, unstaggered grid.

Figure 3. Cell Centered Staggered Grid

The algorithms introduce predictor terms (denoted by *) and corrective terms (denoted by ‘) for the terms

$$\begin{aligned} \rho &= \rho^n + \rho' \\ \vec{u} &= \vec{u}^* + \vec{u}' \\ P &= P^n + P' \end{aligned} \tag{10}$$

The equations solved in the predictor stage are therefore

$$\vec{u}^{*}_{i,j} - H\left[\vec{u}^{*}\right]_{i,j} = -D_{i,j}\left(\nabla P^{n}\right)_{i,j} \tag{11}$$

And the final solution satisfies

$$\vec{u}_{i,j} - H\left[\vec{u}\right]_{i,j} = -D_{i,j}\left(\nabla P\right)_{i,j} \tag{12}$$

By subtracting these two equations the corrective terms can be related using

$$\vec{u}'_{i,j} - H\left[\vec{u}'\right]_{i,j} = -D_{i,j}\left(\nabla P'\right)_{i,j} \tag{13}$$

this equation doesn't satisfy mass conservation unless equation 8 is also satisfied. Substituting in the corrective terms and then linearizing about this equation time n yields

$$\frac{\left(\rho^{n}{}_{i,j} - \rho^{n-1}{}_{i,j}\right)}{\partial t} V + \Delta\left[\left(\rho\vec{u}^{*} + \rho^{*}\vec{u} + \rho^{*}\vec{u}^{*} + \rho'\vec{u}'\right)\cdot S\right]_{i,j} = 0 \tag{14}$$

which can be rewritten using equation 13 as

$$\begin{aligned} &\frac{V\rho(P'_{i,j})}{\partial t} + \Delta\left[\left(\left(\rho(P'_{i,j})\vec{u}^{*}\right)\cdot S\right)\right]_{i,j} - \Delta\left[\rho^{n} D\left(\nabla P'\right)\cdot S\right]_{i,j} = \\ &\frac{(\rho^{n}_{i,j} - \rho^{n-1}_{i,j})}{\partial t} V - \Delta\left[\left(\rho^{n}\vec{u}^{*}\right)\cdot S\right]_{i,j} - \Delta\left[\rho^{n} H\left(\vec{u}'\right)\cdot S\right]_{i,j} - \Delta\left[\left(\rho'\vec{u}'\right)\cdot S\right]_{i,j} \end{aligned} \tag{15}$$

where the dependence of the density on the pressure is formerly connected with the pressure connected term. The SIMPLE algorithm can thus be summarized in the symbolic form, as

Predictor:

$$\vec{u}^{*}_{i,j} - H\left[\vec{u}^{*}\right]_{i,j} = -D_{i,j}\left(\nabla P^{n}\right)_{i,j} \tag{16}$$

Corrector:

$$\begin{aligned} &(\vec{u}', P', \rho')(\vec{u}^{**} = \vec{u}^{*} + \vec{u}', P^{*} = P^{n} + P', \rho^{*} = \rho^{n} + \rho') \\ &\vec{u}'_{i,j} = H\left[\vec{u}'\right]_{i,j} - D_{i,j}\left(\nabla P'\right)_{i,j} \\ &\rho' = \rho(P') \end{aligned} \tag{17}$$

Conditions:

$$\frac{\partial \rho_{i,j}}{\partial t} V + \Delta\left[\left(\rho^{*}\vec{u}^{**}\right)\cdot S\right]_{i,j} = 0$$

$$\frac{\left(\rho^{n} + \rho' - \rho^{n-1}\right)_{i,j}}{\partial t} V + \Delta\left[\left(\rho^{n} + \rho'\right)\left(\vec{u}^{*}_{i,j} + H\left[\vec{u}'\right]_{i,j} - D_{i,j}\left(\nabla P'\right)_{i,j}\right)\cdot S\right]_{i,j} = 0 \quad (18)$$

$$\frac{V\rho(P'_{i,j})}{\partial t} + \Delta\left[\left(\left(\rho(P'_{i,j})\vec{u}^{*}\right)\cdot S\right)\right]_{i,j} - \Delta\left[\rho^{n} D\left(\nabla P'\right)\cdot S\right]_{i,j} =$$

$$\frac{(\rho^{n}_{i,j} - \rho^{n-1}_{i,j})}{\partial t} V - \Delta\left[\left(\rho^{n}\vec{u}^{*}\right)\cdot S\right]_{i,j} - \Delta\left[\rho^{n} H\left(\vec{u}'\right)\cdot S\right]_{i,j} - \Delta\left[\left(\rho'\vec{u}'\right)\cdot S\right]_{i,j}$$

Approximations:

$$Neglect: H\left[\vec{u}'\right]_{i,j}, \Delta\left[\left(\rho'\vec{u}'\right)\cdot S\right]_{i,j} \quad (19)$$

These approximations are valid and have no impact on the final solution because at a converged solution the corrective terms are 0. What these approximations do impact is the convergence rate. Additionally, because the $H\left[\vec{u}'\right]_{i,j}$ term is dropped the pressure correction term is overestimated and an under-relaxation term must be added giving

$$P^{*} = P^{n} + \alpha P' \quad (20)$$

The SIMPLEC [46] algorithm improves on the SIMPLE algorithm by neglecting $H\left[\vec{u}' - \vec{u}'_{i,j}\right]_{i,j}$ instead of just $H\left[\vec{u}'\right]_{i,j}$ which has the effect of approximating the adjective corrective terms from the neighboring cells as being proportional to the velocity correction at cell (i,j) and the nodal separation. This is done by introducing the term

$$\tilde{H}[1] = \frac{\sum A_{nb}}{A_{i,j}} \quad (21)$$

then subtracting $\tilde{H}[1]\vec{u}'_{i,j}$ from equation 13. The SIMPLEC algorithm can be summarized as

Predictor:

$$\vec{u}^{*}_{i,j} - H\left[\vec{u}^{*}\right]_{i,j} = -D_{i,j}\left(\nabla P^{n}\right)_{i,j} \quad (22)$$

Corrector:

$$(\vec{u}', P', \rho')(\vec{u}^{**} = \vec{u}^{*} + \vec{u}', P^{*} = P^{n} + P', \rho^{*} = \rho^{n} + \rho')$$

$$\vec{u}'_{i,j} = \frac{H\left[\vec{u}' - \vec{u}'_{i,j}\right]_{i,j}}{\left(1 - \tilde{H}(1)_{i,j}\right)} - \frac{D_{i,j}}{\left(1 - \tilde{H}(1)_{i,j}\right)}\left(\nabla P'\right)_{i,j} \tag{23}$$

$$\rho' = \rho(P')$$

Conditions:

$$\frac{\partial \rho_{i,j}}{\partial t} V + \Delta\left[\left(\rho^{*}\vec{u}^{**}\right) \cdot S\right]_{i,j} = 0$$

$$\frac{\left(\rho^{n} + \rho' - \rho^{n-1}\right)_{i,j}}{\partial t} V + \Delta\left[\left(\rho^{n} + \rho'\right)\left(\vec{u}^{*}_{i,j} + \frac{H\left[\vec{u}' - \vec{u}'_{i,j}\right]_{i,j}}{\left(1 - \tilde{H}(1)_{i,j}\right)} - \frac{D}{\left(1 - \tilde{H}(1)_{i,j}\right)}\left(\nabla P'\right)_{i,j}\right) \cdot S\right]_{i,j} = 0$$

$$\frac{V\rho(P'_{i,j})}{\partial t} + \Delta\left[\left(\left(\rho(P'_{i,j})\vec{u}^{*}\right) \cdot S\right)\right]_{i,j} - \Delta\left[\rho^{n} \frac{D}{\left(1 - \tilde{H}(1)_{i,j}\right)}\left(\nabla P'\right) \cdot S\right]_{i,j} = \tag{24}$$

$$\frac{(\rho^{n}_{i,j} - \rho^{n-1}_{i,j})}{\partial t} V - \Delta\left[\left(\rho^{n}\vec{u}^{*}\right) \cdot S\right]_{i,j} - \Delta\left[\rho^{n} \frac{H\left[\vec{u}' - \vec{u}'_{i,j}\right]_{i,j}}{\left(1 - \tilde{H}(1)_{i,j}\right)} \cdot S\right]_{i,j} - \Delta\left[\left(\rho'\vec{u}'\right) \cdot S\right]_{i,j}$$

Approximations:

$$Neglect: H\left[\vec{u}' - \vec{u}'_{i,j}\right]_{i,j}, \Delta\left[\left(\rho'\vec{u}'\right) \cdot S\right]_{i,j} \tag{25}$$

The better approximation for the advective terms means that the pressure doesn't have to be under relaxed and therefore a higher convergence rate is obtained [47]. The SIMPLE and SIMPLEC algorithms have the same procedure to generate convergence as shown in Figure 4.

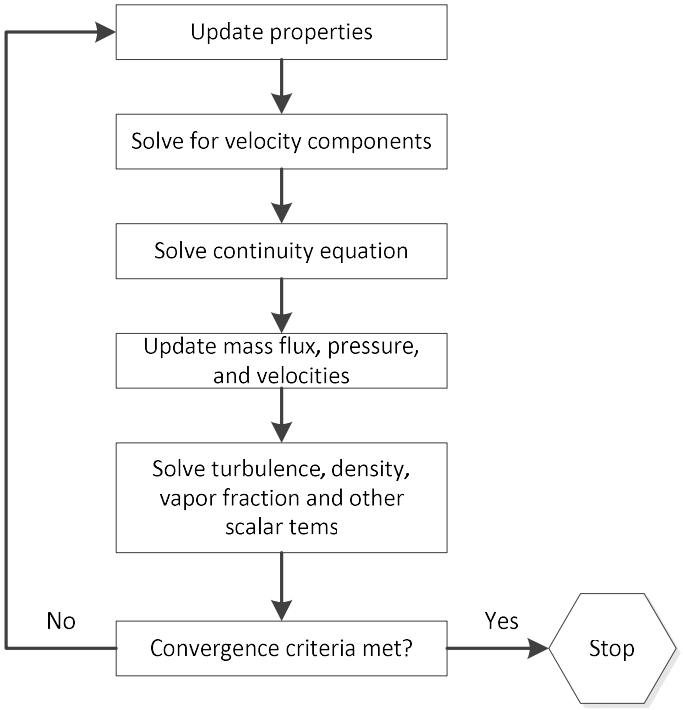

Figure 4. SIMPLEC algorithm procedure [48]

C. Cavitation Models

Cavitation is the process of a phase change from liquid to gas that is similar to boiling a liquid with the distinction that boiling typically refers to a phase change that is initiated by an isobaric temperature increase whereas cavitation is typically thought of as an isothermal process driven by local pressure drops.

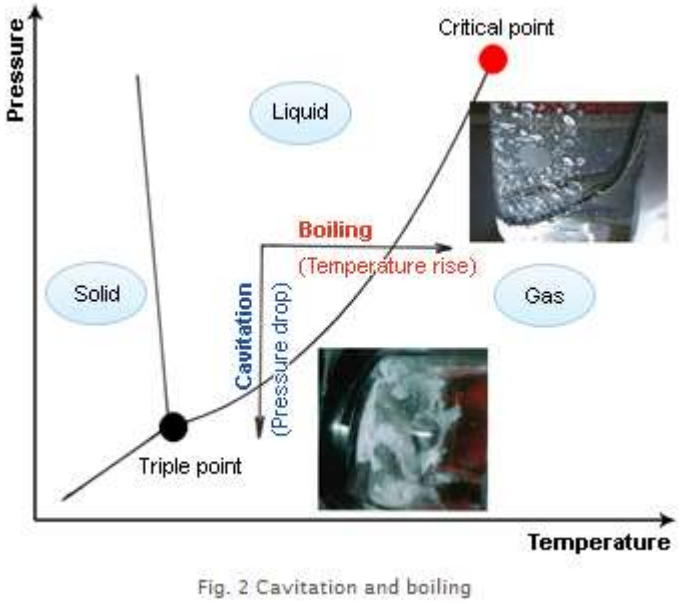

Figure 5. Phase diagram with cavitation and boiling processes[49]

The cavitation number σ is the ratio between the difference of the far field pressure and vaporization pressure and the volumetric kinetic energy and is given by

$$\frac{P_{inlet} - P_v}{P_{inlet} - P_{outlet}} \tag{26}$$

where P_∞ is the far field pressure P_v is the vaporization pressure at the temperature T_∞. This number describes the potential of a flow to cavitate. If the cavitation number is significantly large, indicative of an operational pressure is much greater than the vaporization pressure or that the velocities are very small, then it is unlikely for cavitation inception to occur. As the cavitation number decreases the likely hood of inception and proliferation of cavitation increases.

For this study the large velocity magnitudes, especially those present at low injector lifts, makes the inception of cavitation inevitable introducing a need to model the impact

of the phase change on the local fluid properties. The two broad categories of numerical methods used to model multiphase flows are differentiated by whether they assume the phases exist within an interpenetrating continuum or those that do not.

There are several methods used that do not assume an interpenetrating continuum and model the interface between the vapor and liquid. These include interface tracking, front capturing, level set, and bubble tracking methods. The small scale of cavitation bubbles makes it computationally expensive to resolve and track the interfacial region. This has led to these methods not being widely adopted beyond 2D simulations.

The alternative approach assumes an interpenetrating continuum between the phases and that the local cell properties can be described via volumetric averaging based on the phase volume. These models can be categorized as either single or multi-fluid models[50]. Multi-phase models are usually applied to separated and non-equilibrium dispersed models where there are no clearly defined flow structures, and the different phases can have different velocities and temperatures. These models are not widely used in injector simulations because the validation for the cavitation closure is difficult due to the experimental difficulties discussed in the prior sections.

Single fluid approaches only apply the conservation equation to the primary mixture phase. In these models the continuity equation is rewritten for the mixture, vapor phase and liquid phase as

$$\frac{\partial}{\partial t}\left(\rho_m\right) + \nabla \cdot \left(\rho_m \vec{u}\right) = 0 \tag{27}$$

$$\frac{\partial}{\partial t}\left(\rho_v\right) + \nabla \cdot \left(\rho_v \vec{u}\right) = R_e - R_c \tag{27b}$$

$$\frac{\partial}{\partial t}\left(\rho_l\right) + \nabla \cdot \left(\rho_l \vec{u}\right) = -R_e + R_c \tag{27c}$$

Under these assumptions the local density and viscosity terms and velocity terms become

$$\rho_m = \sum_{k=1}^{n} \alpha_k \rho_k \tag{28}$$

$$\mu_m = \sum_{k=1}^{n} \alpha_k \mu_k \tag{29}$$

where α_k represents the volume fraction of phase k. With these modifications a new term, volume fraction, is introduced and provides the closure for the vapor fraction. These models assume that both phases are, inside the local cells, uniformly mixed and no interphase boundaries can be identified.

The approache used to model the vapor generation and dissipation for single fluid models are barotropic models, models derived from the transport equation and models derived from the Rayleigh-Plesset equation. Barotropic models assume the local pressure has an instantaneous effect on the density of the homogenous mixture. Barotropic models have been developed by Dellanoy and Kueney [51] , Avva, et al. [52], Schmidt, et al. [35] and Dumont et al. [53] and are derived by simplifying the energy equation to

$$c_m^2 \frac{D\rho}{Dt} = \frac{DP}{Dt} \tag{30}$$

where c_m is the mixture speed of sound and can be modeled using the equation of Wallis [54]

$$\frac{1}{c_m^2}\frac{\partial \rho_m}{\partial P} = \rho_m \left(\frac{\alpha}{\rho_v c_v^2} + \frac{1-\alpha}{\rho_l c_l^2} \right) \tag{31}$$

which is integrated to produce the pressure density relationship

$$P(\rho_m) = P_{vap} + \frac{\rho_v - \rho_l}{\rho_v \rho_l} \frac{1}{\left(\rho_l c_l\right)^{-2} + \left(\rho_v c_v\right)} \log\left[\left(\frac{\rho_m c_m}{\rho_l c_l} \right)^2 \right] \tag{32}$$

which provides an explicit algebraic pressure-density relationship for the mixture that determines the volume fraction. These models have a few distinct disadvantageous. They cannot model the impact of the quality of the liquid on the cavitating flow and are unable to model the baroclinic nature of cavitating flows.

Models based on the transport equation are based on the conservative form of the vapor phase of the mixture (27b), model the source term using different equations. Chen and Heister [55] modeled the source term as

$$S_a = C\frac{\rho_l^2}{\rho_m(\rho_l - \rho_v)}\frac{P_v - P}{\rho_l u_\infty^2} \tag{33}$$

where C is an empirical rate constant. The predictive qualities of the model are extremely dependent on the empirical constant C and, for a given C, applicable only over a small range of flows. Additionally, the cavitation formation rates are steady rather than transient. Other models have been developed by Kunz et al [56], Ahuja et al. [57], Yuan et al. [58] and Singhal et al. [59] but they exhibit the same limitations where they are only valid over the small ranges that they were tuned for and exhibit steady formation rates. Additionally, the models can produce rates that vary be orders of magnitude over the same flow condition. It was the conclusion of Sauer [60] that these limitations in accurately describing the formation rates and the transient effects of cavitation require a move to models based on the Rayleigh-Plesset equation.

Rayleigh-Plesset bubble equations [61] are the basis for the third approach for modeling the volume fraction and the interphase mass transfer.

$$R_B\frac{D^2R_B}{Dt^2} + \frac{3}{2}\left(\frac{DR_B}{Dt}\right)^2 = \left(\frac{P_B - P}{\rho_l}\right) - \frac{4\upsilon_l}{R_B}\frac{DR_B}{Dt} + \frac{2S}{\rho_l R_B} \tag{34}$$

Here R_B is the bubble radius, $P_{B,}$ is the pressure of the bubble and is assumed to be equal to the vaporization pressure, ν_l is the liquid kinematic viscosity and S is the surface tension. This equation is simplified by omitting the higher order terms as well as the viscous and surface terms reducing the equation to the following equation.

$$\frac{DR_B}{Dt} = \sqrt{\frac{2}{3}\left(\frac{P_B - P}{\rho_l}\right)} \tag{35}$$

This describes the void propagation of a bubble and can be used to derive relations for the mixture density. There are different models that use this equation as a basis for modeling the effects of cavitation. The model used in these studies is the Zwart-Gerber-Bellarmi model which assumes that all the bubbles within a system have the same size and models the mass transfer rate, R, per unit volume as

$$R = n\left(4\pi R_B^2 \rho_v \frac{DR_B}{Dt}\right)/V \tag{36}$$

which is recognizable as the surface area of a bubble, its growth rate, and the number of bubbles (n) multiplied by the density of the vapor phase. The vapor faction can be calculated from the ratio between the volume occupied by the vapor and the total volume.

$$\alpha = n\left(\frac{4}{3}\pi R_B^3\right)/V \tag{37}$$

These two equations can be combined to form an expression for the net mass transfer that is only a function of the local pressure.

$$R = \frac{3\alpha_v \rho_v}{R_B}\sqrt{\frac{2}{3}\left(\frac{P_V - P}{\rho_l}\right)} \tag{38}$$

This form of the equation works well for condensation; however, since it's based on the assumption that the cavitation bubbles won't interact with each other it is invalid for evaporation because. except at the initial stages of cavitation, there is a decrease in possible nucleation sites for the inception of a bubble as the vapor volume fraction increases. This is accounted for by replacing α_v with $\alpha_{nuc}\left(1-\alpha_v\right)$ where α_{nuc} is an empirical correlation that describes the rate the number of possible nucleation sites decreases at as the vapor volume fraction rises during evaporation. The final form for the mass transfer rates become

$$\begin{aligned}
&\text{If } P \le P_v \\
&R_e = F_{evap}\frac{3\alpha_{nuc}\left(1-\alpha_v\right)\rho_v}{R_B}\sqrt{\frac{2}{3}\left(\frac{P_v - P}{\rho_l}\right)} \\
&\text{If } P \ge P_v \\
&R_c = F_{cond}\frac{3\alpha_v \rho_v}{R_B}\sqrt{\frac{2}{3}\left(\frac{P_v - P}{\rho_l}\right)}
\end{aligned} \tag{39}$$

where F_{cond} and F_{evap} are empirical correlation terms. The condensation rates and the volume fractions are constrained by the following equations.

$$\sum_{k=1}^{N} \alpha_k = 1$$
$$R_e - R_c = 0 \tag{40}$$

Alternative formulations of cavitation models such as those by Schneer and Sauer [62] differ by correlating the bubble radius to the local volume fraction, or by assuming a geometric size distribution. Other models, such as the Singhal et al. model[59], includes the surface tension term. However studies by Kozubkova et al. [63], and Bily et al. [64] found that the models that omitted the surface tension terms better matched experimental data in venturi tube tests and were numerically more stable.

This study, which has it focus on the transient flow features during injector operation, uses a Rayleigh-Plesset based model because it is the only group that can capture the phase transition at transient rates. The specific model used is the zwart-gerber-bellarmi which is the most numerically stable over the largest flow regimes.

III. TURBULENCE MODELS

Two different approaches were used to model the turbulence within the simulation. A base RANS model was originally used prior to the observation that a pure RANS model was not able to accurately capture the flow fields at which time a DES model was used.

A. RANS Turbulence Models

The RANS turbulence model utilizes the realizable k-ε formulation of Shih et al. [65] which modifies the base k-ε formulation of Jones and Launder [66] and Launder and Spalding [67] based on turbulent constitutive relations [68] to create a generalized relationship for the Reynolds stresses based only on the mean velocity gradients and using k and ε to characterize the turbulence length scales. Application of rapid distortion theory [69] shows that rapid mean rotation has no impact on isotropic turbulence which provides a constraint for the strain rates. Turbulent realizability principles[70-72] imposes a requirement of non-negativity for the turbulent normal stresses and produces constraints for the coefficients within the Reynolds stress equations that limits the situations under which the model will produce non-physical results. The modeled transport equations for k and ε are

$$\frac{\delta}{\delta t}\left(\rho k\right)+\frac{\delta}{\delta x_j}\left(\rho k u_j\right)=\frac{\delta}{\delta t}\left[\left(\mu+\frac{\mu_t}{\sigma_k}\right)\frac{\delta k}{\delta x_j}\right]+G_k+G_b-\rho\varepsilon-Y_m+S_k \quad (41)$$

And

$$\frac{\partial}{\partial t}\left(\rho\varepsilon\right)+\frac{\partial}{\partial x_j}\left(\rho\varepsilon u_j\right)=\frac{\partial}{\partial t}\left[\left(\mu+\frac{\mu_t}{\sigma_\varepsilon}\right)\frac{\partial\varepsilon}{\partial x_j}\right]+ \rho C_1 S_\varepsilon-\rho C_2\frac{\varepsilon^2}{k+\sqrt{\upsilon\varepsilon}}+C_{1\varepsilon}C_{3\varepsilon}G_b+S_\varepsilon \quad (42)$$

where Y_m is the contribution of the fluctuating dilation in compressible turbulence to the overall dissipation rate, G_k is the generation of turbulence kinetic energy due to mean velocity gradients given by

$$Gk = -\rho\overline{u_i' u_j'}\frac{\partial u_j}{\partial x_i} \tag{43}$$

G_b is the generation of turbulence kinetic energy due to buoyancy and S_ε and S_k are source terms. The constant C_1 is defined as

$$C_1 = \max\left[0.43, \frac{\eta}{\eta+5}\right], \eta = S\frac{k}{\varepsilon}, S = \sqrt{2S_{ij}S_{ij}} \tag{44}$$

The realizable k-ε turbulence model calculates the eddy viscosity as:

$$\mu_t = \rho C_\mu \frac{k^2}{\varepsilon} \tag{45}$$

which is the same as the standard k-ε model. The realizable formulation differs by treating the eddy viscosity constant as a function that is dependent on the mean strain and rotation rates, the angular velocity of the system rotation and the local turbulence fields. It is calculated using

$$C_\mu = \frac{1}{A_0 + A_s\dfrac{kU^*}{\varepsilon}} \tag{46}$$

where the dimensionless velocity U* is given by

$$U^* = \sqrt{S_{ij}S_{ij} + \tilde{\Omega}_{ij}\tilde{\Omega}_{ij}} \tag{47}$$

S is the mean strain rates and the $\tilde{\Omega}$ is the mean rate of rotation tensor viewed in a moving reference frame with angular velocity ω_k. The constant A_0 and A_S are

$$A_0 = 4.04, A_S = \sqrt{6}\cos\phi \tag{48}$$

where

$$\phi = \frac{1}{3}\cos^{-1}\left(\sqrt{6}W\right), W = \frac{S_{ij}S_{jk}S_{ki}}{\tilde{S}^3}, \tilde{S} = \sqrt{S_{ij}S_{ij}}, S_{ij} = \frac{1}{2}\left(\frac{\partial u_j}{\partial x_i} + \frac{\partial u_i}{\partial x_j}\right) \tag{49}$$

and the model constants, calibrated for the model with canonical flows, are

$$C1_{\varepsilon} = 1.44, C_2 = 1.9, \sigma_k = 1.0, \sigma_{\varepsilon} = 1.2 \tag{50}$$

B. LES Turbulence Models

The LES model seeks to resolve the larger scale eddies that are of a smaller scale than the local grid size as a stress tensor. Large eddy simulation techniques were first proposed by Smaginosky [73]. The LES flow equations are produced by filtering the general flow equations, the filtering is implicitly provided by the volume discretization of the computational area to the scale of a singular computational cell. The filtered momentum and continuity equations are:

$$\frac{\partial \rho}{\partial t} + \frac{\partial}{\partial x_i}\left(\rho \overline{u}_i\right) = 0 \tag{51}$$

and

$$\frac{\partial}{\partial t}\left(\rho \overline{u}_i\right) + \frac{\partial}{\partial x_i}\left(\rho \overline{u}_i \overline{u}_j\right) = \frac{\partial}{\partial x_j}\left(\sigma_{ij}\right) - \frac{\partial \overline{P}}{\partial x_i} - \frac{\partial \tau_{ij}}{\partial x_j} \tag{52}$$

where an over bar denotes a filtered variable averaged over the cell form with the generalized form of

$$\overline{\phi}(x) = \frac{1}{V}\int_V \phi(x')dx', x' \in V \tag{53}$$

here V is the cell volume and x' represents special filter cutoff where the filter function, $G(x,x')$, implicitly given by the volume discretization is

$$G(x,x') = \begin{cases} 1/V, x' \in v \\ 0, x' \in otherwise \end{cases} \tag{54}$$

and σ_{ij} denotes a stress tensor arising from molecular viscosity described by

$$\sigma_{ij} = \left[\mu\left(\frac{\partial \overline{u}_i}{\partial x_j} + \frac{\partial \overline{u}_j}{\partial x_i}\right)\right] - \frac{2}{3}\mu\frac{\partial \overline{u}_i}{\partial x_i}\delta_{ij} \tag{55}$$

and τ_{ij} is the sub grid scale stress defined by

$$\tau_{ij} = \overline{\rho} u_i \tilde{u}_j - \overline{\rho} \tilde{u}_i \tilde{u}_j \tag{56}$$

where the general form of the density weighted filter is:

$$\tilde{\phi} = \frac{\overline{\rho\phi}}{\overline{\rho}} \tag{57}$$

The sub grid scale stress is split into the isotropic and deviatoric parts

$$\tau_{ij} = \underbrace{\tau_{ij} - \frac{1}{3}\tau_{kk}\delta_{ij}}_{deviatoric} + \underbrace{\frac{1}{3}\tau_{kk}\delta_{ij}}_{isotropic} \tag{58}$$

where the isotropic portion is small enough to be neglected and the deviatoric portion is modeled using

$$\tau_{ij} - \frac{1}{3}\tau_{kk}\delta_{ij} = -2\mu_t \left(S_{ij} - \frac{1}{3} S_{kk}\delta_{ij} \right) \tag{59}$$

where S_{ij} is the strain rate tensor in direction ij. The eddy viscosity, μ_t, is modeled as

$$\mu_t = \rho L_s^2 \left| \overline{S} \right| \tag{60}$$

where L_s is the mixing length for the sub-grid scales and $\left|\overline{S}\right|$ is computed using:

$$\left| \overline{S} \right| \equiv \sqrt{2\overline{S}_{ij}\overline{S}_{ij}} \tag{61}$$

C. DES Turbulence Model

The delayed eddy simulation [74] is a turbulence model that makes use of RANS methods at near wall location where the boundary layer is assumed to be sufficiently fine to resolve the local flow fields while making use of LES methods in the far field where the mesh is coarser and unlikely to be sufficient to correctly resolve the flow fields. Figure 6 shows the different flow regions considered in a DES simulation.

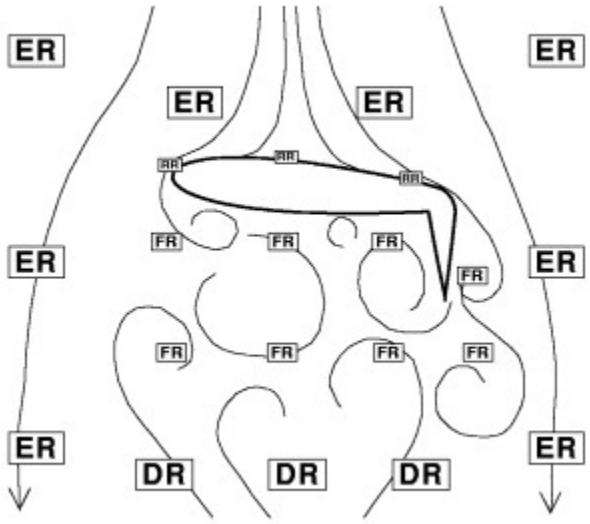

	Eularian Region (ER)
RANS	RANS Region (RR)
LES	Departure Region (DR)
LES	Focus Region (FR)

Figure 6. Visualization of the different DES Regions[75]

The Eularian region is a region far enough away from a boundary that the turbulence generated by flows over the solid body never enters. The RANS region is the region closest to the body where the grid is assumed to be refined enough to be able to capture the flow features with a spatially averaged turbulence scheme. The focus region is the region close enough to the body that the turbulence must be fully resolved to capture the correct flow features but where the grid tends to be too coarse to resolve the turbulence using spatially averaged methods. Refinement of this region can allow DNS simulations; however, this comes at the cost of greatly enhanced computational costs. The departure

region is the regions far enough away from solid bodies that the full resolution of the turbulence becomes irrelevant to the solution.

To link the two equations the mechanism modeling the turbulence in the region where the model transitions from RANS based turbulence to an LES based turbulence model needs to be modified to ensure that there is no numerical divergence. To ensure this the dissipation term is modified to use

$$Y_m = \frac{\rho k^{\frac{3}{2}}}{l_{des}} \tag{62}$$

where

$$l_{des} = \min\left(l_{rke}, l_{les}\right), l_{rke} = k^{\frac{3}{2}}, \mathrm{l_{les}} = \mathrm{C_{des}}\,\Delta_{\max} \tag{63}$$

where C_{des} is a calibration constant of 0.61 and Δ_{max} is the maximum local grid spacing.

IV. STRUCTURAL SOLVER METHODOLOGY

A. Equations of motion

This work makes use of the ANSYS software package to solve the matrix equations of motion

$$M\ddot{u} + Ku = F \tag{64}$$

where M is the mass matrix, K is the stiffness matrix, F is the known vector of external forces and u is the displacement vector. The solution for this equation must solve the initial values

$$\begin{aligned} u(0) &= d \\ \dot{u}(o) &= v \end{aligned} \tag{65}$$

where d and v are the initial displacements and velocities and, for these simulations are 0. The solver makes use of the HHT time integration method[76] which modifies Newmark's approximation[77] improving the numerical stability. Equation 64 is linearized using one step difference methods as

$$\begin{aligned} & Ma_{n+1} + (1+\alpha)Kd_{n+1} - \alpha Kd_n = F_{n+1} \\ & d_n + 1 = d_n + \Delta t v_n + \Delta t^2 \left[\left(\frac{1}{2} - \beta \right) a_n + \beta a_{n+1} \right] \\ & v_n + 1 = v_n + \Delta t \left[(1-\gamma) a_n + \gamma a_{n+1} \right] \end{aligned} \tag{66}$$

where n is the number of time step, Δt is the time increment between n and n+1, d_n, v_n, and a_n are the approximations for $u(t_n)$, $\dot{u}(t_n)$ and $\ddot{u}(t_n)$ where $F_n = F(t_n)$ and α, β, and γ are free parameters that govern the stability and numerical dissipation of the algorithm.

In these simulations the dampening matrix K is estimated using Rayleigh Damping[78] which gives K as

$$K = \frac{\alpha}{2\omega} + \frac{\beta\omega}{2} \tag{67}$$

where α and β are the Rayleigh damping coefficients and ω is the natural frequency.

B. Solid Contact Modeling

This model makes use of contact tools native to ANSYS structural. The contact can occur between the bottom of the needle (surfaces 1-3) and the seating face of the nozzle (surface 4) in Figure 7. There is a 10 micron offset for contact because the fluent solver is limited and always requires at least 1 cell in a gap to avoid numerical instabilities that arise from zero volume spaces.

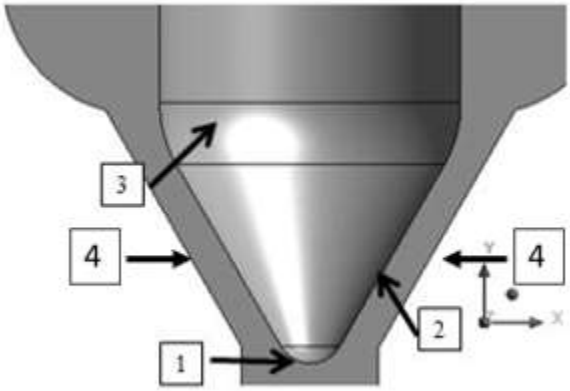

Figure 7. Surfaces that can come into contact during the bending motion

Contact occurs when there is penetration between the faces of the two solid bodies (Figure 8).

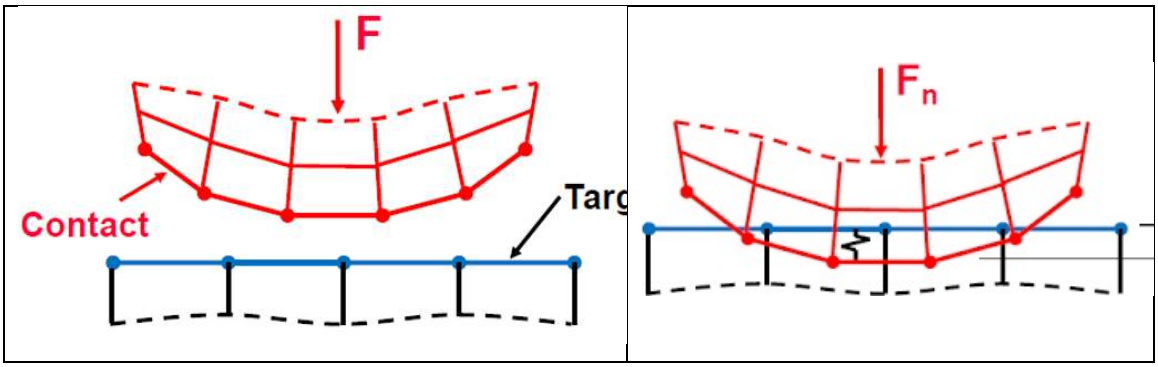

Figure 8. Two surfaces a) not in contact and b) in contact (Ansys Theory)

The penetration is resolved by applying a normal force that is proportional to the stiffness and the penetration.

$$F_{normal} = K_{normal} x_{Pentration} \tag{68}$$

C. Needle Lift Profile

This model uses a lift profile for the movement of the needle along the vertical axis. This is required because the rigid body motion of the needle along the vertical axis is driven by a force balance that extends beyond the domain considered in this study. To include all the surfaces necessary to explicitly model this motion would require a domain that is four times the current size. The lift profile that is used is shown in Figure 9 and was experimentally measured from a production Cummins injector at Argonne national lab.

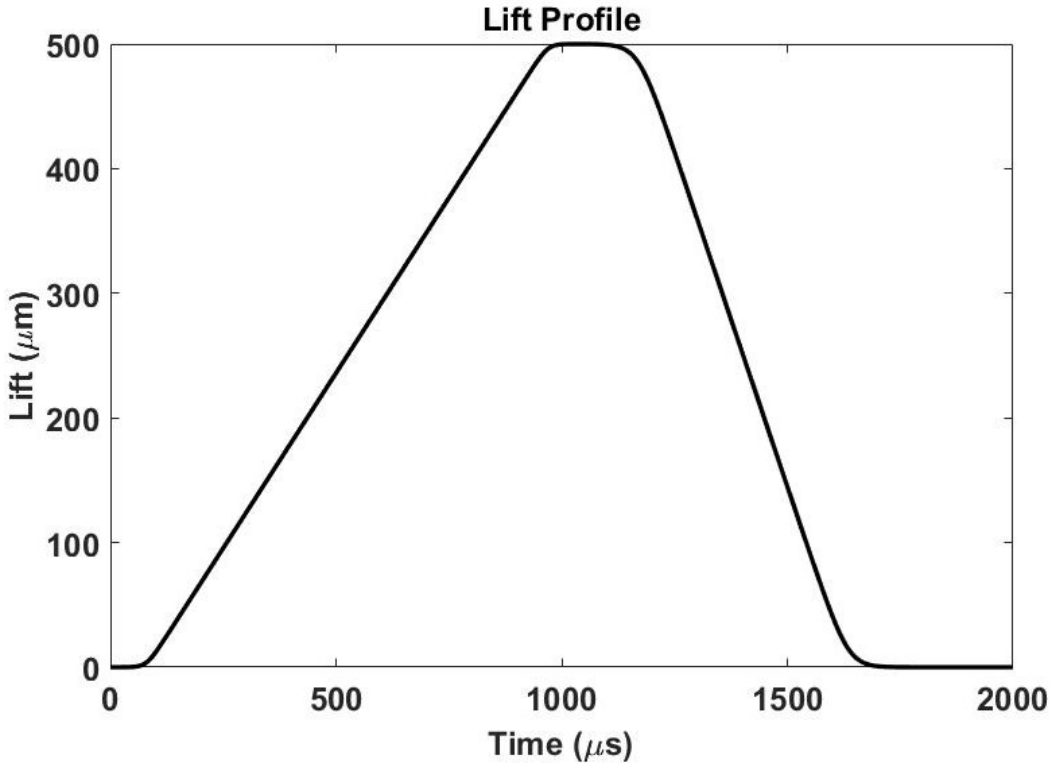

Figure 9. Lift profile for the vertical needle motion.

This motion is described by the following equation

$$A_1 \log\left(\frac{\cosh\left(a_1\left(t-T_1\right)\right)}{\cosh\left(a_1\left(t-T_2\right)\right)}\right) - A_2 \log\left(\frac{\cosh\left(a_2\left(t-T_3\right)\right)}{\cosh\left(a_2\left(t-T_4\right)\right)}\right) \tag{69}$$

Where t is the current time and the specific coefficients for this profile are

$$\begin{aligned} A1 &= 5.62 \\ A2 &= -21.5 \\ a1 &= 0.05 \\ a2 &= 0.025 \end{aligned} \tag{70}$$

D. Coupling Method

The solver uses a coupling method based on the conservation of energy along the continuous fluid structure interface[79] [80], Γ, where the virtual displacement of the interface, δu, and the forces are given by

$$\begin{aligned} \delta u_f &= \delta u_s \\ F_f &= F_s \end{aligned} \tag{71}$$

and the subscripts s,f denotes the fluid or solid side of the interface. In cases where the meshes discrete interfaces do not match (most often due to the differences in the number of grid elements needed to resolve the structural and fluid domains as seen in Figure 10) $\Gamma_f \neq \Gamma_s$ and the displacements are instead described by

$$\partial u_f = H \partial u_s \tag{72}$$

where H is a transformation function that is dependent on the coupling method. The forces can be represented as

$$F_s = H^T F_f$$

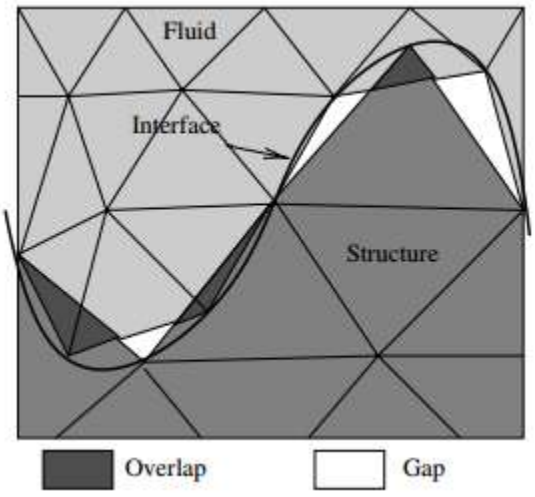

Figure 10. Non-matching interface[81]

The coupling used in this study is based on nearest neighbor interpolation[82] where the displacements are written as

$$u_s(x) = \sum_{i=1}^{n_s} N_s^i(x) u_{si}$$
$$u_f(x) = \sum_{i=j}^{n_f} N_f^k(x) u_{fj} \tag{73}$$

and N is the basis function at the interface. A weighting equation N_α is introduced and integrated over the interface. The equations from 58 are then equated to generate:

$$\sum_{i=1}^{n_s} \underbrace{\left[\int_\Gamma N_\alpha^k N_s^i dx \right]}_{A_{\alpha s}^{ki}} u_{si} = \sum_{j=1}^{n_f} \underbrace{\left[\int_\Gamma N_\alpha^k N_f^j dx \right]}_{A_{\alpha f}^{kj}} u_{fj} \tag{74}$$

When a Galerkin method is used N_α must either assume the basis function for the fluid or solid side. Because the displacements are known on the structural side the basis function for the fluid side is chosen (α=f) so the matrix $A_{\alpha f}$ can be inverted, and the fluid displacements can be obtained using:

$$u_f = A_{ff}^{-1} A_{fs} u_s \tag{75}$$

The matrix A_{fs} is evaluated using Gauss integration[83],[84] where

$$A_{fs}^{ki} = \int_\Gamma N_f^k(x) N_s^i(x) dx \approx \sum_{j=1}^{n_f} \sum_{g=1}^{n_{gp,j}} w_g N_f^k(x_{g,j}) N_s^i\left(\Pi_s\left(x_{g,j}\right)\right) \tag{76}$$

And $n_{gp,j}$ is the number of Gauss quadrature points x_g in cell j. w+ is the weight of the g^{th} quadrature point and $\Pi_s\left(x_{g,j}\right)$ is the projection of $x_{g,i}$ from the fluid mesh onto the solid mesh. To transfer the forces Nα instead assumes form of the basis function of the solid side and equation 57 is rewritten as:

$$F_s = A_{ss}^{-1} A_{sf} F_f \tag{77}$$

and the matrix A_{sf} is evaluated as

$$A_{sf}^{kj} = \int_{\Gamma} N_s^k(x) N_j^f(x) dx \approx \sum_{j=1}^{n_s} \sum_{g=1}^{n_{gp,j}} w_g N_s^k(x_{g,j}) N_f^i\left(\Pi_f\left(x_{g,j}\right)\right) \tag{78}$$

V. GRID UPDATE METHODS

To accommodate the displacement of the solid needle in the fluid computational domain two mesh deformation methods were used in tandem. For smaller mesh deformations smoothing methods are employed. As these smaller deformations accumulate the local mesh quality can degrade, for cases such as these local cells are remeshed, and the data interpolated onto new mesh.

A. Smoothing Methods

The smoothing scheme employed in these studies are governed by the diffusion equation

$$\nabla \cdot \left(\gamma \nabla \vec{u} \right) = 0 \tag{79}$$

Where $\vec{u}$ is the mesh displacement velocity and γ is the diffusion coefficient and is a function of the normalized boundary distance d and a user input α.

$$\gamma = \frac{1}{d^{\alpha}} \tag{80}$$

For a constant diffusion coefficient (i.e., α = 0) the mesh is deformed uniformly, for non-constant diffusion coefficients the cells that have high diffusion tend to move together in unison. For these simulations a value of α = 0.5 was used. This has the effect of moving the mesh in a way that preserves boundary layers on the face that is moving and deforming cells that are further away from the boundary layers.

B. Remeshing Methods

Remeshing is performed dynamically to avoid highly skewed and/or negative cell volumes that might otherwise result from the movement of the solid body. In this study the remeshing was controlled by a sizing function that limited the growth rate of the cells as you move away from boundary walls as well as provides a minimum allowable size of a cell. This is accomplished by sub-dividing the fluid domain into different background grids whose size is determined by the local minimum feature length and a user specified resolution. The local size function SF_I is evaluated at the vertices of the background grids (see figure below) using the equation

$$SF_I = \left(\frac{\sum \frac{1}{D_J} \Delta S_J}{\sum \frac{1}{D_J}} \right) \tag{81}$$

where D_J is the distance from vertex I on the background grid to the centroid of boundary cell J and ΔS_J is the mesh size of boundary cell J (Figure 11).

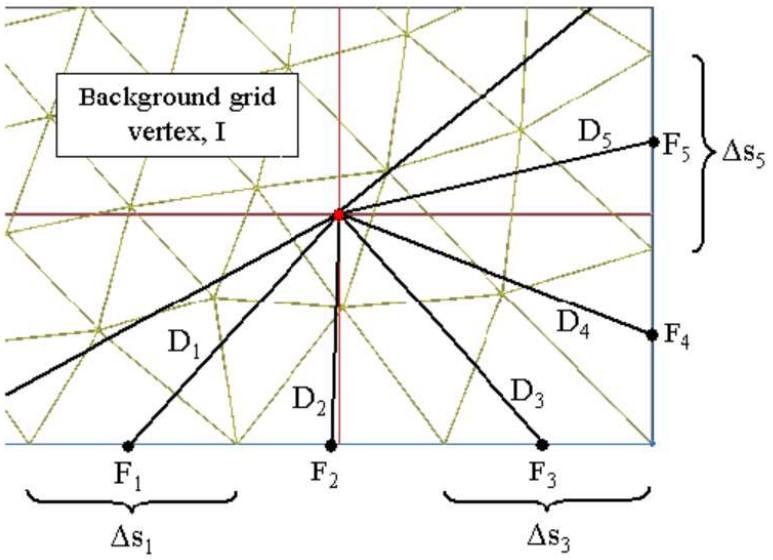

Figure 11. Vertex distance to boundaries. [48]

The intermediate value of the size function $size_b$ at cell centroid P is then calculated by averaging the size functions at the vertices after they've been weighted (Figure 12) by the distance between the vertices and the cell centroid P (L_I) using

$$size_b = \left(\frac{\sum SF_I \frac{1}{L_I}}{\sum \frac{1}{L_I}} \right) \tag{82}$$

The normalized distance for point P is given by

$$d_b = \frac{d_{\min}^P}{d_{\max}} \tag{83}$$

where $d_{\min}^P$ is the minimum boundary distance at point P. The size function at point P can be defined as

$$size_P = size_b(1 + \alpha \times d_b^{1+2\beta}) \tag{84}$$

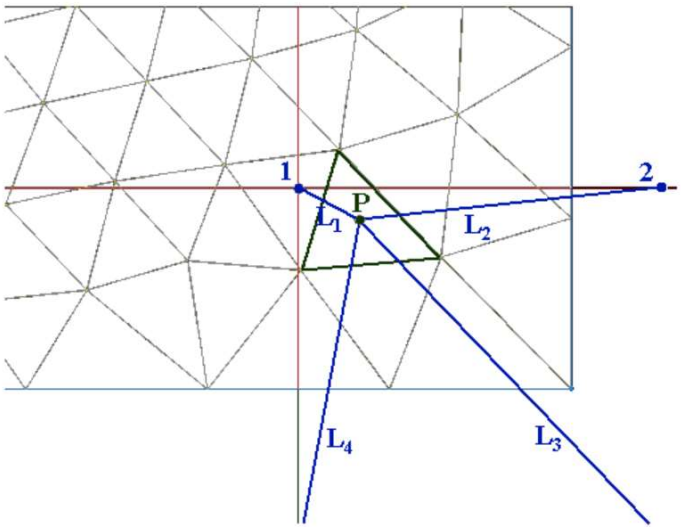

Figure 12. Size function interpolation. [48]

where α is the size function variation and defines the maximum cell size in relation to its closest boundary cell and β is the size function rate and controls the speed with which the cells can grow as you move away from the boundary. These are user defined variables. As the mesh deforms if the cell size is larger than the specified size the cell is remeshed into smaller cells to satisfy the size functions

VI. CODE VALIDATION

A. Numerical Code Validation

This study was performed using the ANSYS Fluent environment to simulate the flow within an injector using a detached eddy simulation (DES) turbulence model to achieve turbulence closure. The DES model has been validated against of several different canonical cases. To validate this approach to modeling the internal flow of the injector the numerical code was validated for the canonical case of flow over an immersed sphere. There have been a number of studies that sought to specifically validate the DES turbulence model over a wide range of Reynolds numbers ([85], [86]) as well as the specific code used within ANSYS Fluent [87]. The results presented below were performed at a Reynolds number of 10,000 which is approximately the maximum Reynolds number within the injector and is a case studied in the previously mentioned papers. The Simulation was able to match the Strouhal number drag coefficient and the fluctuating portion of the lift coefficient (Table 1).

Source	C_d	S_t	C_l'
Constantinescu et al. [37]	0.393	0.195	Not Reported
Kim [88]	0.438	0.181	Not Reported
Achenbach [89] (Experimental)	0.40+/- 0.01	Not Reported	Not Reported
Jones and Clarke [87]	0.387	0.191	0.07
CFD Results	0.435	0.190	0.07

Table 1. Sphere Simulation Summary

B. Spatial Sensitivity Study

A grid sensitivity analysis was conducted using the DES model. The baseline mesh contained approximately 8.5 million cells and had a maximum y+ of 3.1. The coarse mesh contained approximately 6 million cells and had a maximum y+ of 6.5. The refined mesh had about 10 million cells and a maximum y+ of 2.2. These simulations were carried out with a time step of 0.05 microseconds as was chosen from the time sensitivity analysis. Table 2 shows the maximum amplitude of the force in the X-direction on the first three needle surfaces (Figure 13) and the principle force variation frequency on each of these three surfaces.

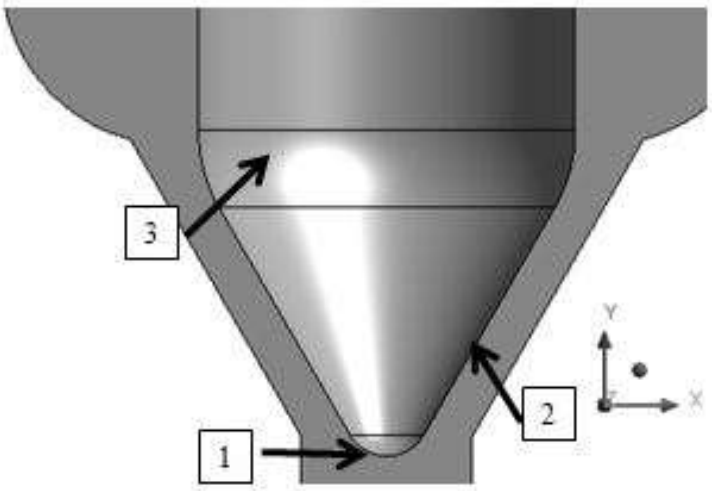

Figure 13. Locations for the bottom three surfaces of the injector needle

	Coarse	Baseline	Fine
Surface 1 Force Amplitude (N)	0.32	0.38	0.38
Surface 2 Force Amplitude (N)	2.25	2.88	2.75
Surface 3 Force Amplitude (N)	1.10	0.98	0.93

Table 2. Force Amplitude for Grid sensitivity Analysis.

The difference in the force magnitude between the baseline and fine mesh is at most 5% on all surfaces and there is a significant decrease in computational time required

compared to the fine mesh. Because of the negligible force difference and significant decrease in computational time his study was performed using the baseline mesh sizing.

C. Temporal Sensitivity

A temporal sensitivity analysis using the DES turbulence model was performed to choose the time step required to resolve the relevant flow features. Three time steps were chosen: 0.1, 0.05 and 0.025 microseconds. Figure 14 shows the lateral force magnitude on surface 3 which was chosen to be discussed because it experiences relatively large fluctuations in the force magnitude over a short time. This figure was limited to a 5 microsecond timeframe rather than the 40 used later in this study so the trends for each simulation can be seen clearly.

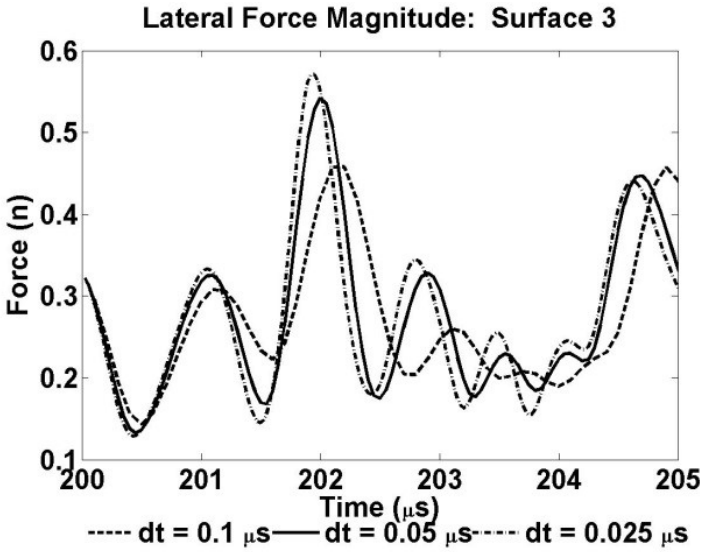

Figure 14. Lateral force magnitudes on surface 3 from the temporal sensitivity analysis

From the analysis the largest time step was found to be inadequate in capturing the frequency and amplitudes of the fluctuations in the lateral forces. The two smaller time steps capture all the fluctuations of the forces over the time shown although there are slight discrepancies in the magnitude. The time step of 0.05 microseconds was picked for the simulations because the discrepancies were found to be small enough to not warrant the much larger computational resources necessary to use the smallest time step.

VII. STEADY STATE RESULTS

A study of the results of the injector under steady state conditions can give a quick understanding of the general flow characteristics exhibited during the operation of the injector. These different lifts can be roughly divided into two groups based upon the height of the lift. A cutoff can be established by characterizing what the major flow restriction is. High lifts are defined as those above which the cross-sectional area at the inlet of the spray hole is greater than the minimal cross-sectional plane in the direction normal to the flow path between the needle and the seat of the injector body.

A. Simulation Settings

The injector used for this study has 8 spray holes with a 19° exit angle, $\theta_{sprayhole}$, and a *K* factor of zero. The *K* factor describes the conicity and is defined as follows

$$K = \frac{D_{inlet} - D_{outlet}}{L_{sprayhole}} \tag{82}$$

where D_{inlet} and D_{outlet} are the diameters at the inlet and outlet of the spray holes and $L_{sprayhole}$ is the spray hole length. Figure 15 shows the entire fluid domain and close of the sac with the inlets and outlets marked as well as the relevant geometrical features.

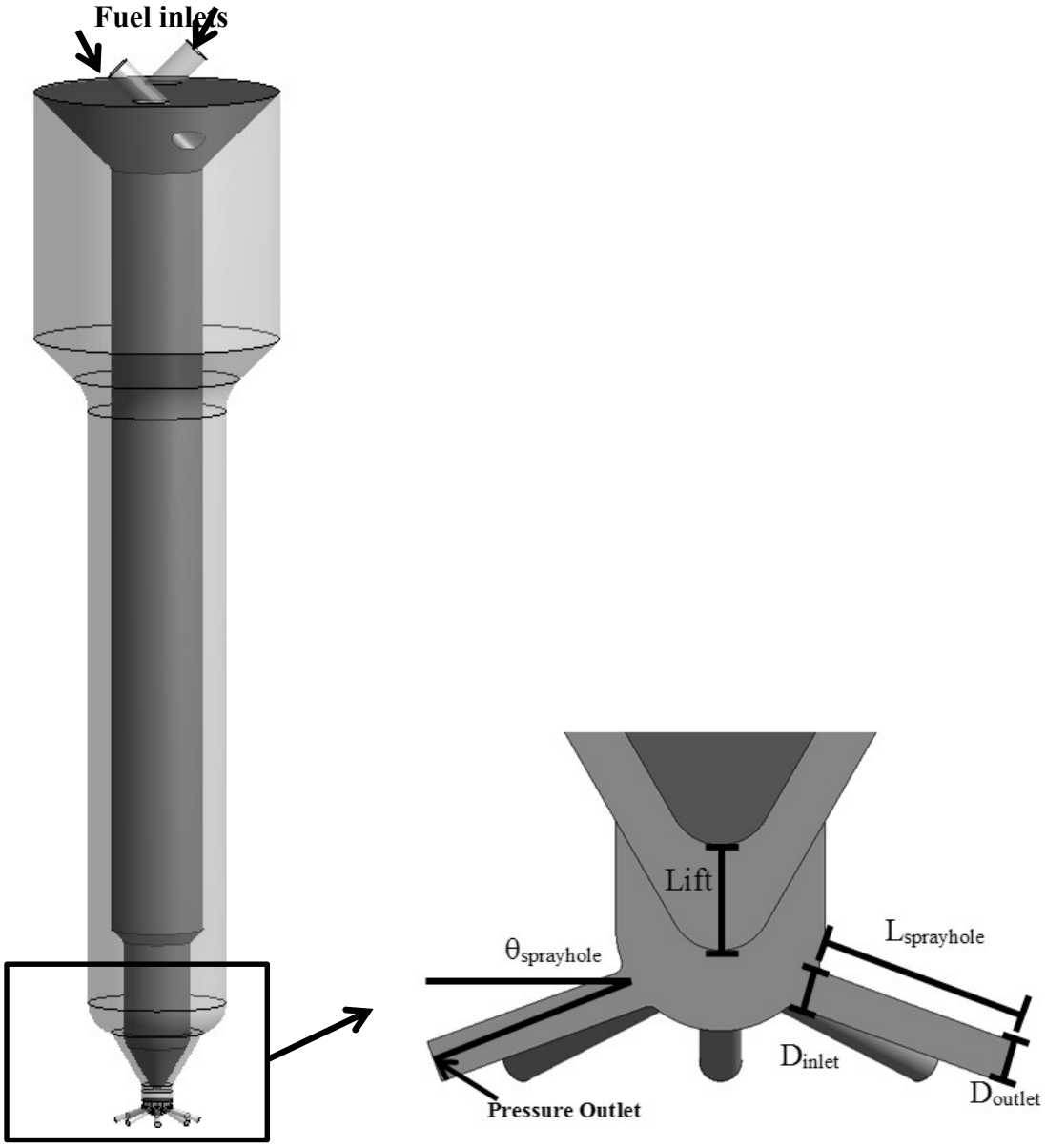

a) Fuel injector b) Close-up view of the sac

Figure 15. The injector with dual gain orifices and the sac. A) The injector body with the needle darkened. B) Zoomed in view of the sac with pressure outlets. The lift is defined as the vertical distance of the needle tip between its highest and lowest position.

In this paper the needle was at its highest lift position of 500 microns where the needle hovers and spends the majority of an injection cycle. The inlet has a specified a total pressure of 2400 bar. The k and ε are determined by the following equations [48]:

$$k = \frac{3}{2}(\vec{u}_{avg} I)^2 \tag{83}$$

$$I = 0.16(\mathrm{Re})^{-1/8} \tag{84}$$

$$\varepsilon = C_{\mu}^{3/4} \frac{k^{3/2}}{l} \tag{85}$$

$$l = 0.09D \tag{86}$$

here I is the turbulent intensity, Re is the Reynolds number based on the inlet orifice diameter and the averaged fuel injection velocity, C_{μ} is an empirical constant of and l is the turbulent length scale based on the inlet diameter D. Macian et al. [25] showed that for injector simulations variations between 1 and 20% for the inlet turbulence intensity has no impact on the results. A pressure outlet boundary condition is used at the exit of the spray holes and the pressure is specified as atmospheric pressure.

The fluid properties are based on the calibrated diesel fuel Viscor 1487 at a constant temperature of 150°C. The density and viscosity are assumed to be dependent only on the local pressure. The vapor phase is treated as an ideal gas undergoing isothermal expansion and compression. Both the DES and RANS simulations used the realizable k-epsilon model for the near wall treatment.

B. Low Lift Results

Low lift flows are characterized by a lower sac pressure (Figure 16) resulting from the higher viscous frictional loses through the tighter seated area and subsequently lower lifting forces are present. The lowered sac pressure increases the penetration of the flow from the seated area into the sac in an almost jet like shape (Figure 17) with the lowest lifts having the furthest penetration before the flow turns toward the spray hole. The deep penetration and large turn create a flow separation along the bottom of the spray hole (Figure 18). As the lift increases the penetration lessens until the flow turns and enters the spray hole at the approximate center when the lift is about 100 microns. This minimizes the amount of separated flow which in turn lessens the amount of vapor formed within the spray hole (Figure 19). For the lower lifts the flow separation along the bottom of the spray hole (Figure 18) creates low pressure zones (Figure 16) which creates cavitation (Figure 19). Within the sac the large penetration at the lower lifts create a recirculation zone above the spray hole along the wall furthest from the needle (Figure 18) that leads to a cavitation zone within the sac that leads to string cavitation (Figure 19).

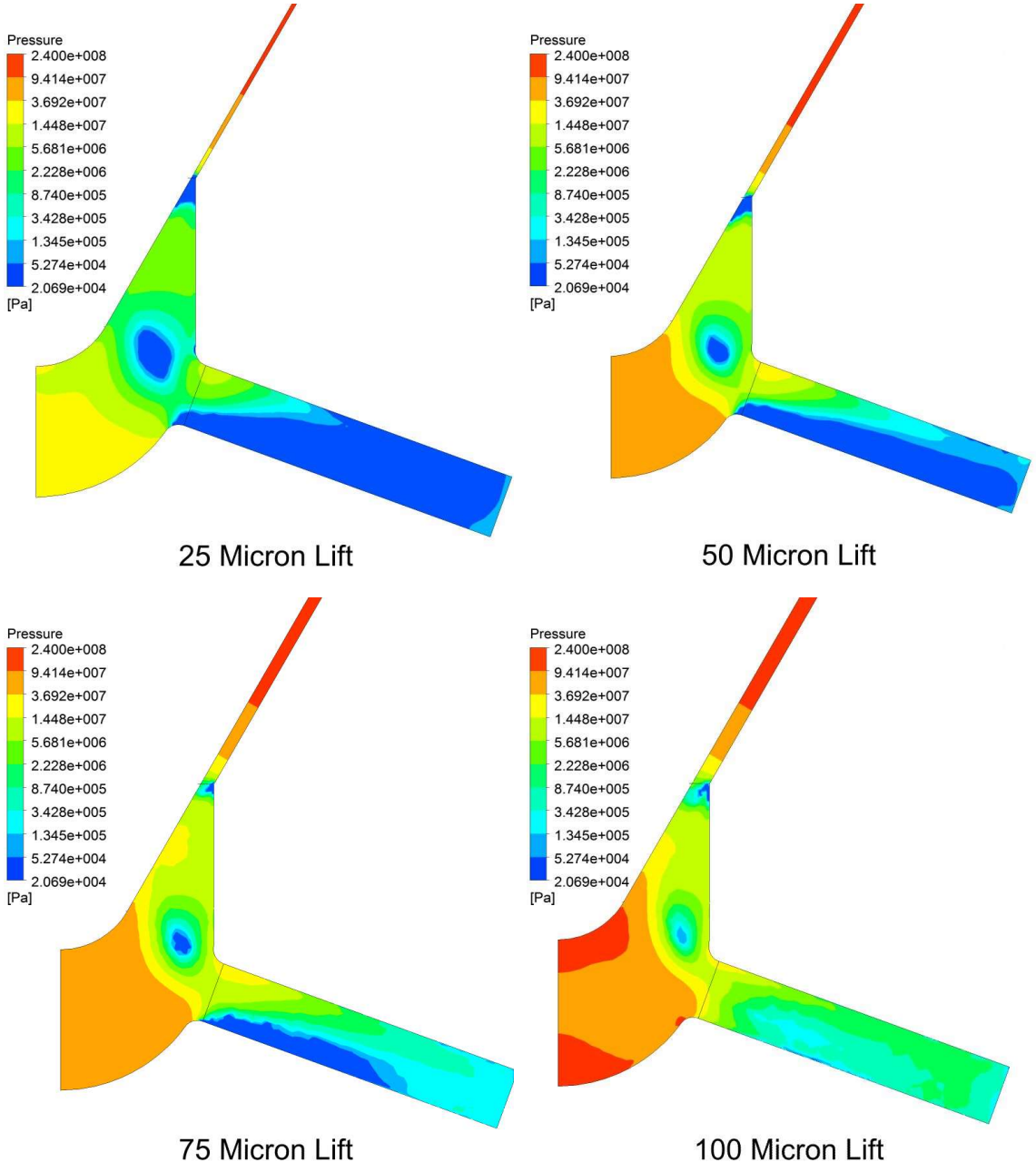

Figure 16. Low Lift Pressure

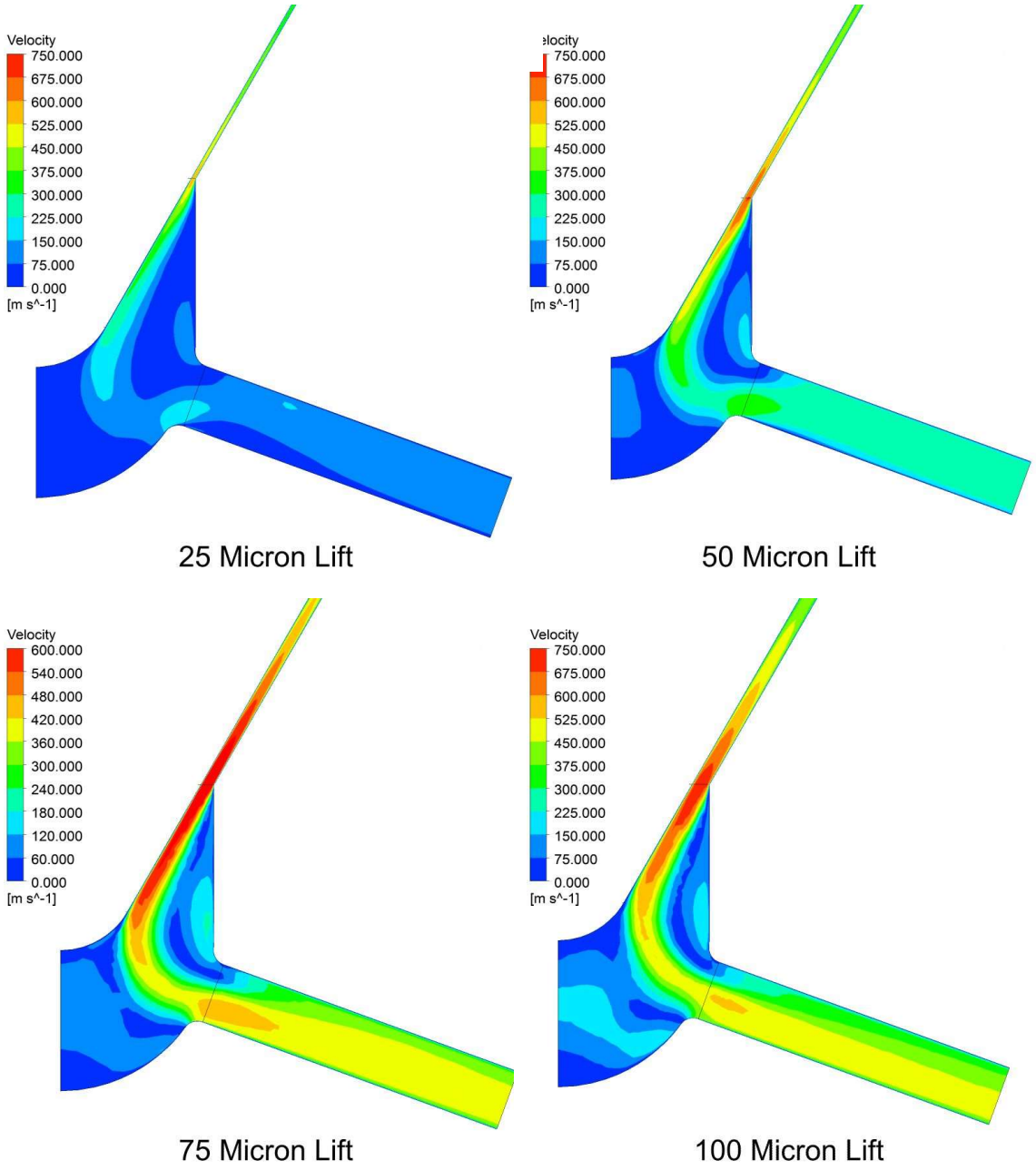

Figure 17. Low Lift Velocity Contours

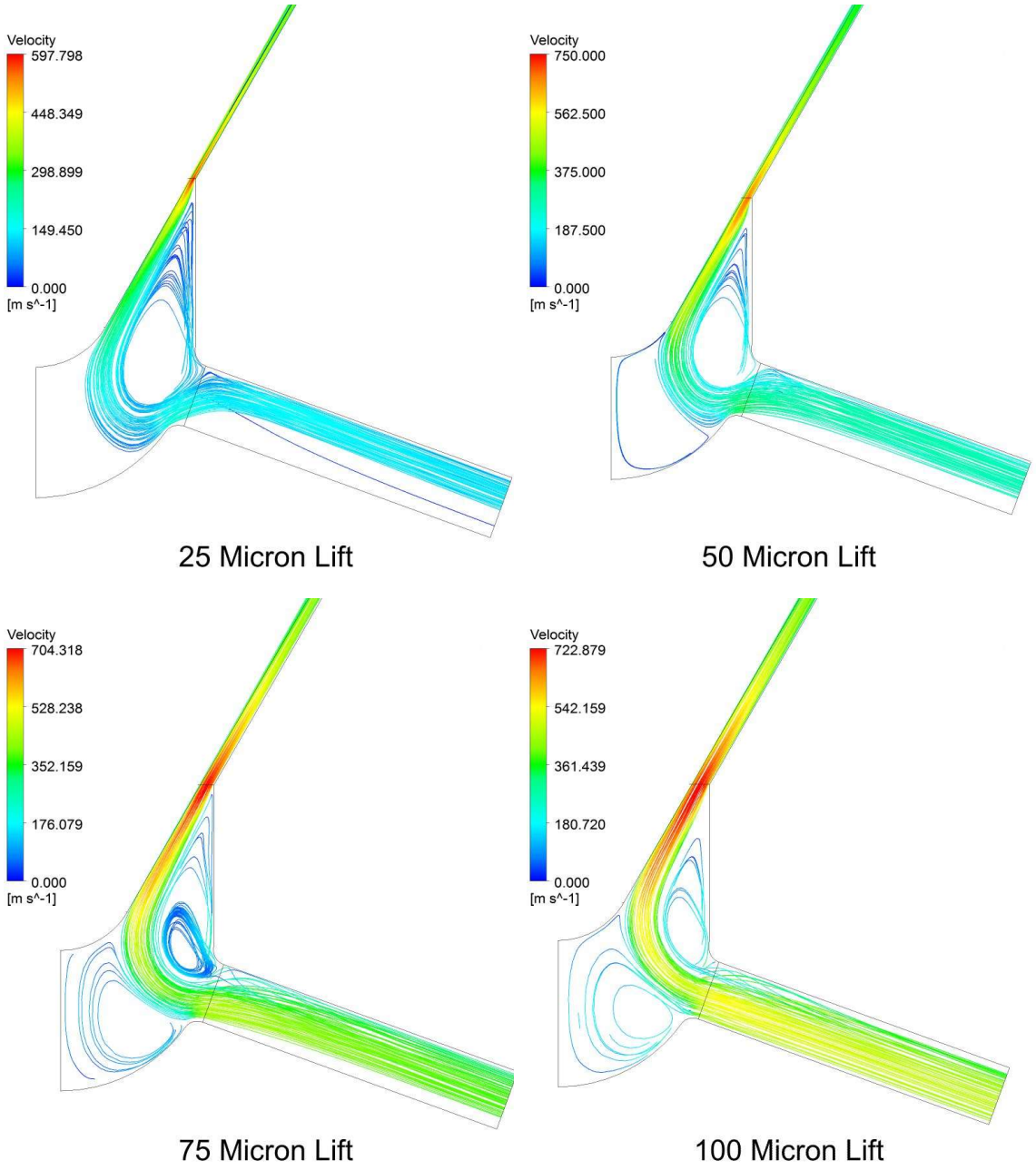

Figure 18. Low Lift Streamlines

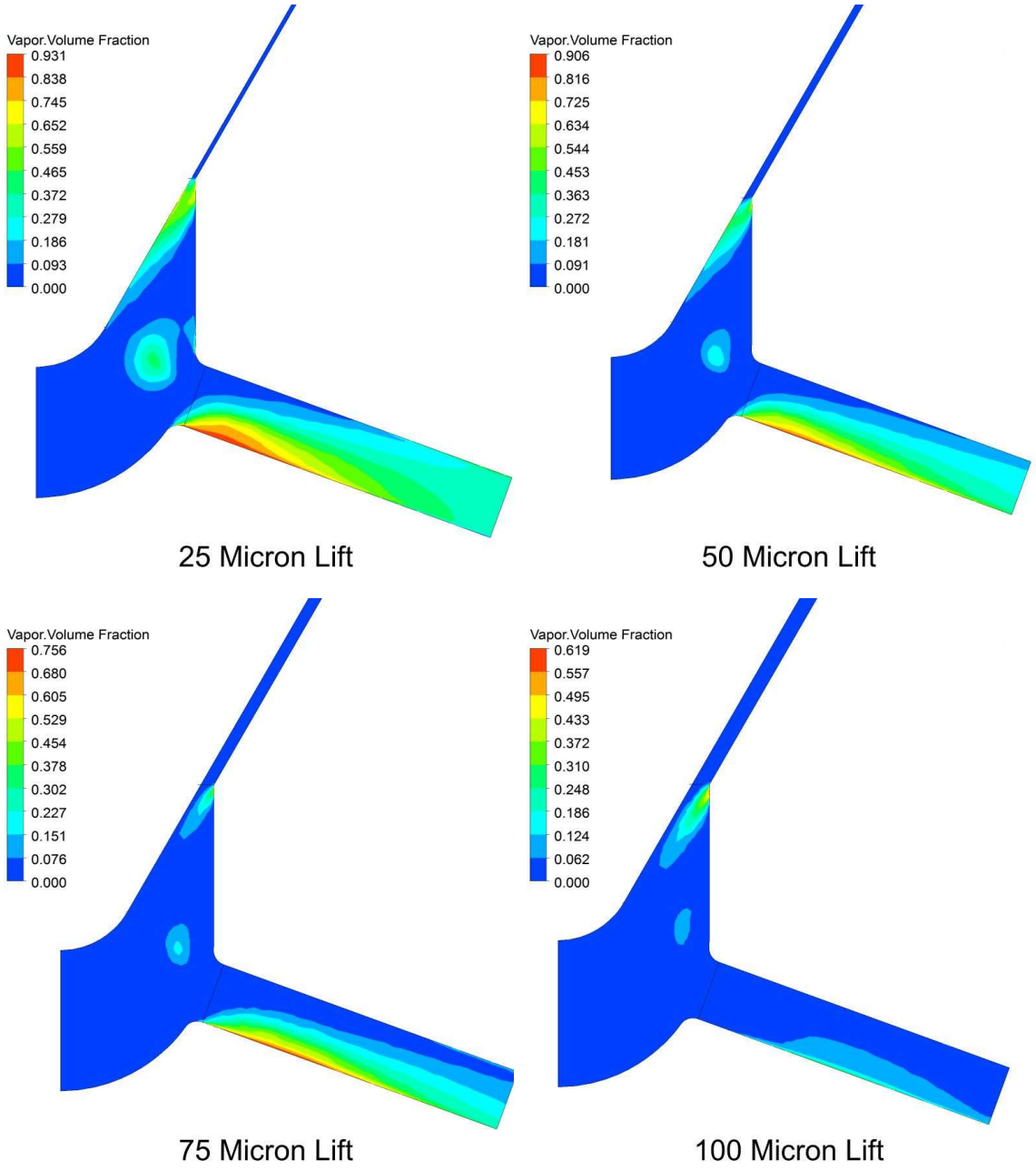

Figure 19. Low Lift Vapor Volume Fraction

C. High Lift Results

The higher lifts are characterized by lower pressure losses over the seat than the lower lifts (Figure 20) which leads to a maintained high pressure within the sac (Figure 21) throughout the higher lifts.

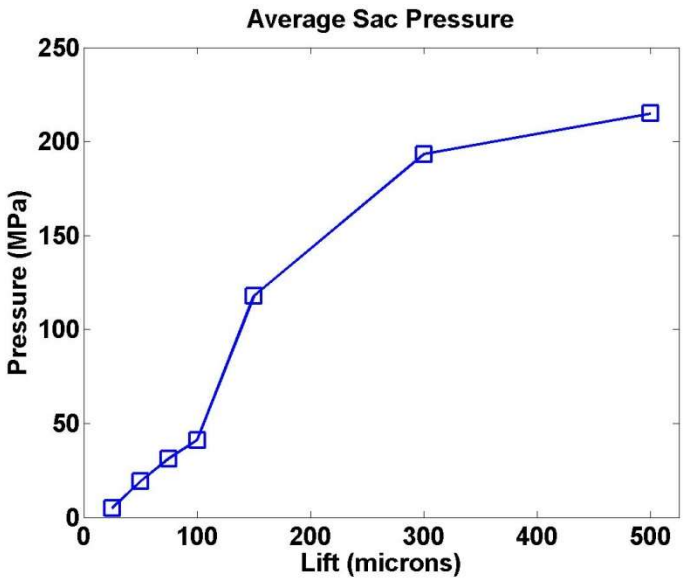

Figure 20. Lift Vs. Pressure

The higher pressure within the sac stops the formation of sac cavitation (Figure 23) at these higher lifts even in the presence of recirculation zones (Figure 24) as well as limiting the velocity over the seat into the sac as the pressure difference between the upstream portion of the needle is less and the cross sectional flow area is greater. The maximum velocity now occurs in the spray hole (Figure 22) due to the increased back pressure creating a greater pressure drop between the sac and the pressure outlet than at the low lifts. The formation of vapor now occurs along the upper side of the spray hole (Figure 23) as the flow separates as it passes the upper radius leading into the spray hole (Figure 24). As the pressure increases with the higher lifts the length and height of the separated flow decreases leading to minimum spray hole vapor at the highest lift.

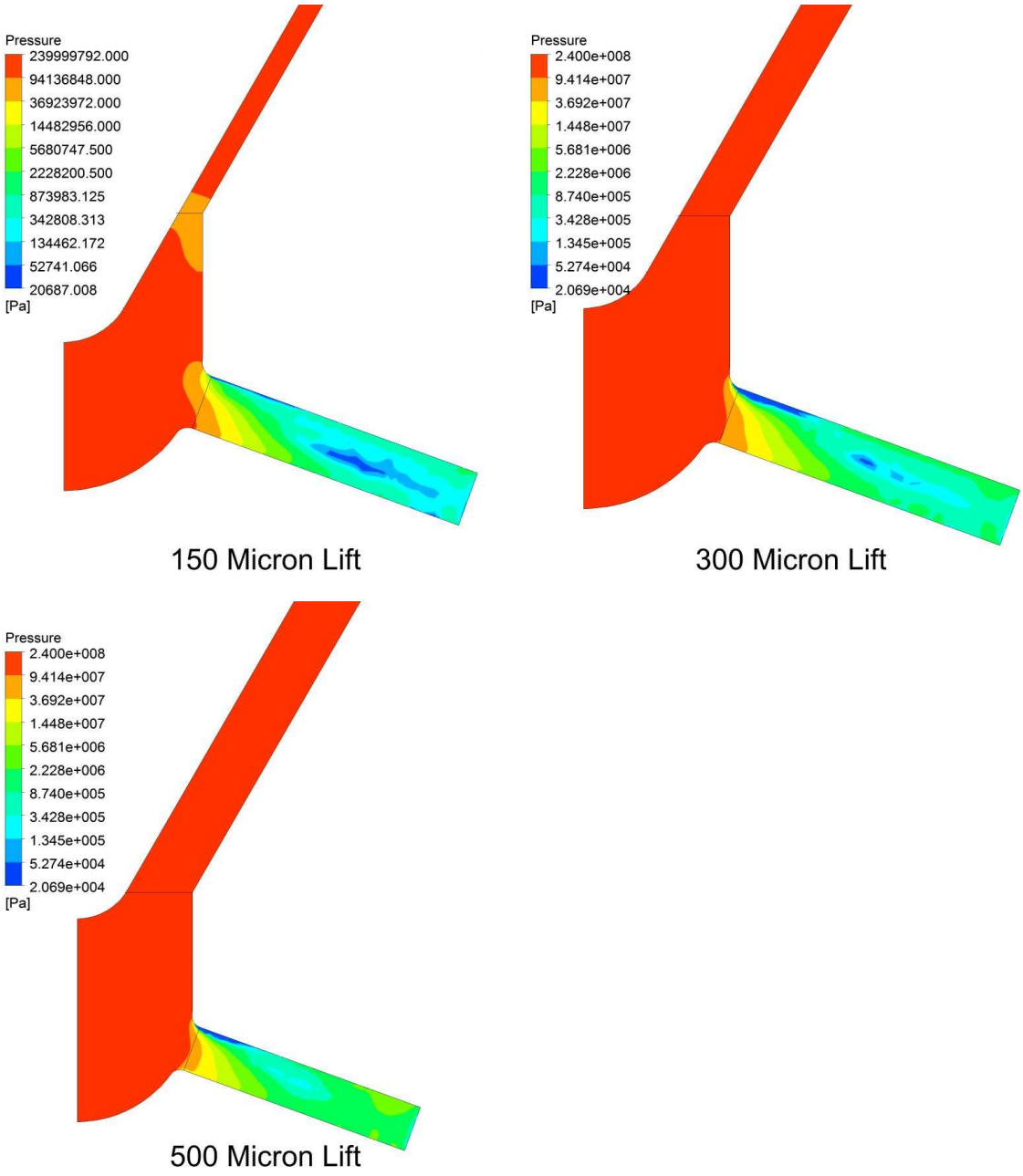

Figure 21. High Lift Pressure

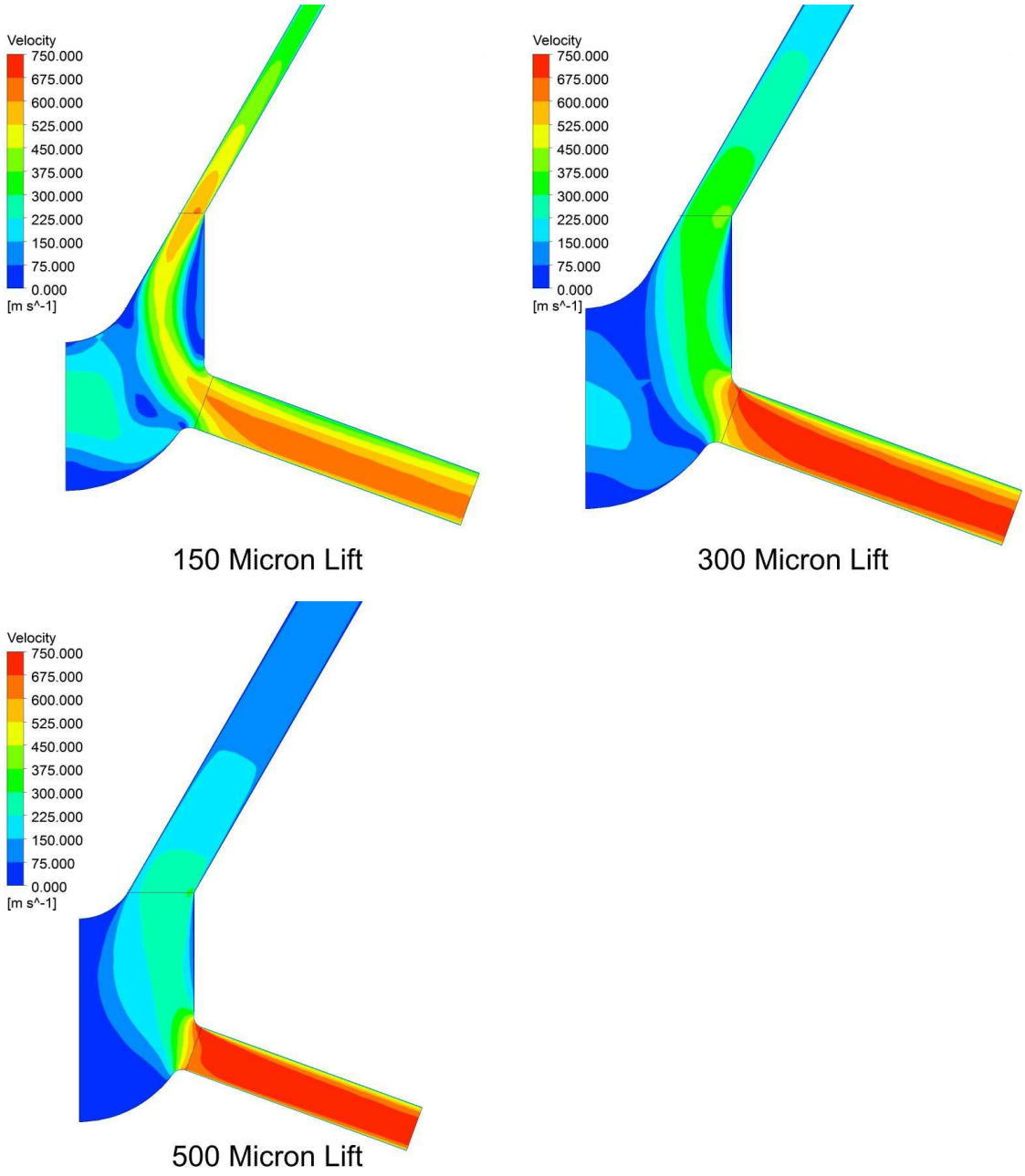

Figure 22. High Lift Velocity Contours

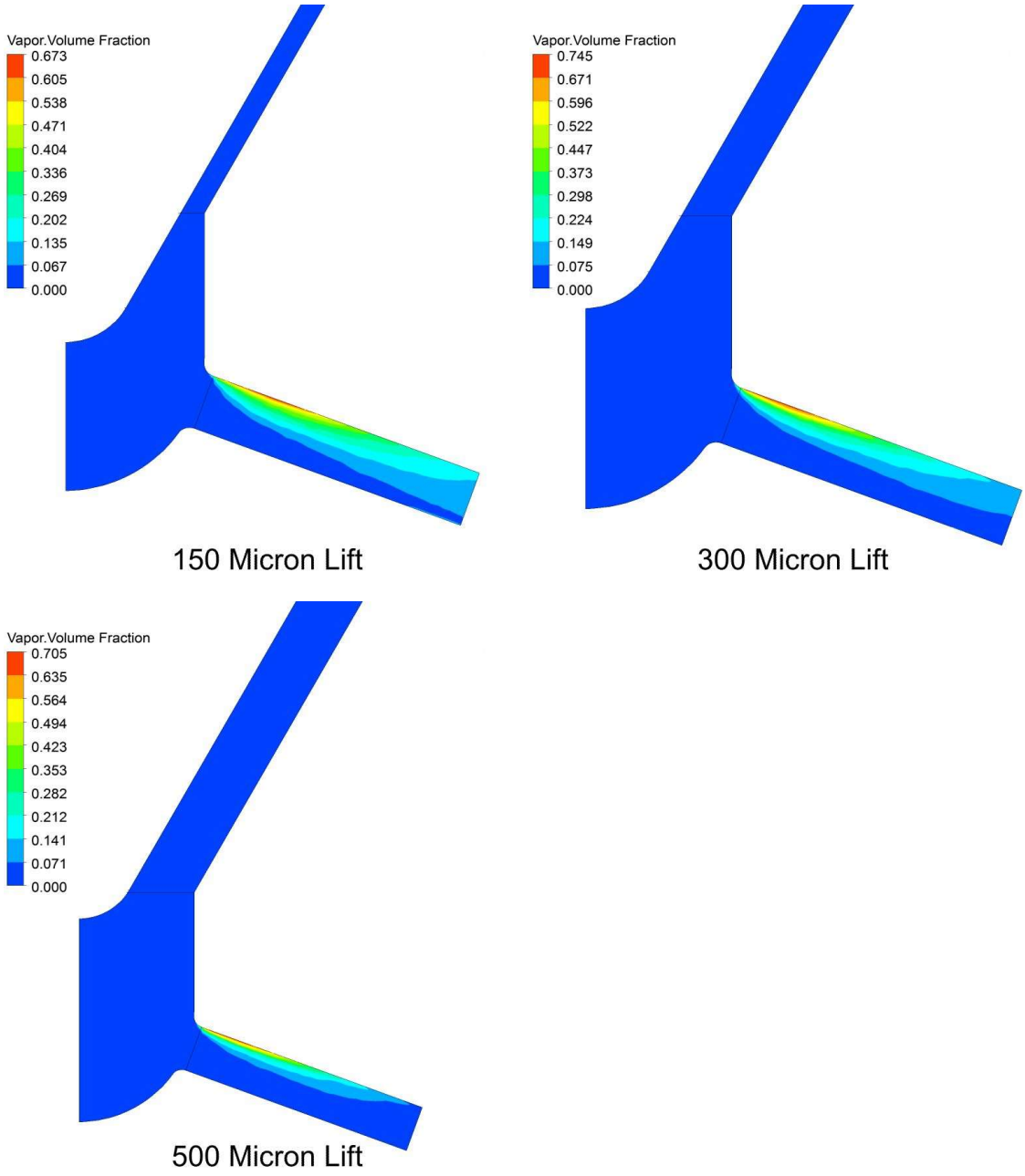

Figure 23. High Lift Vapor Volume Fraction

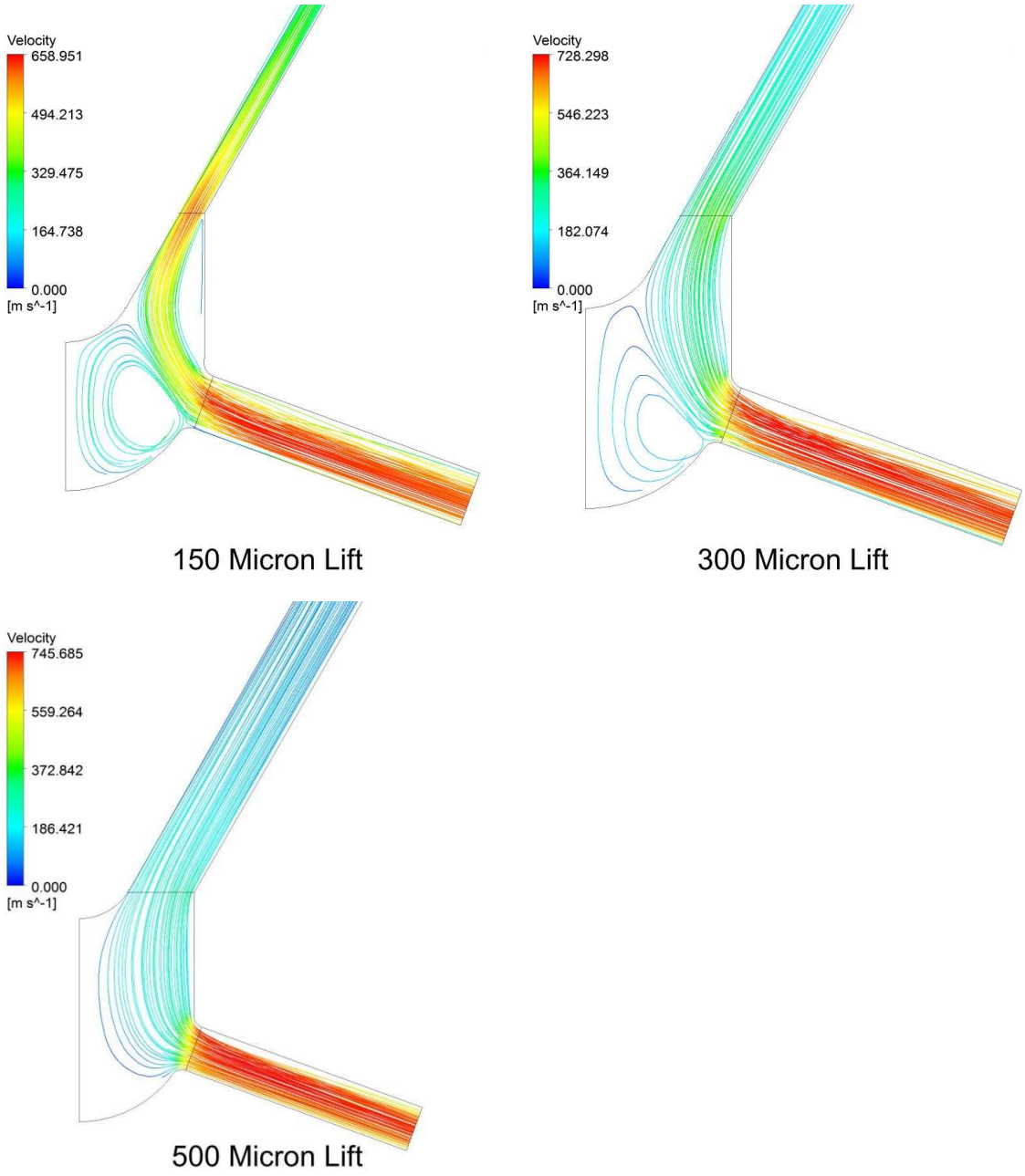

Figure 24. High Lift Stream Lines

D. Low and High Lift Comparison

The previously discussed changes in the sac pressure (Figure 20) as the lift increases leads to a corresponding increase in the average spray hole velocity (Figure 25).

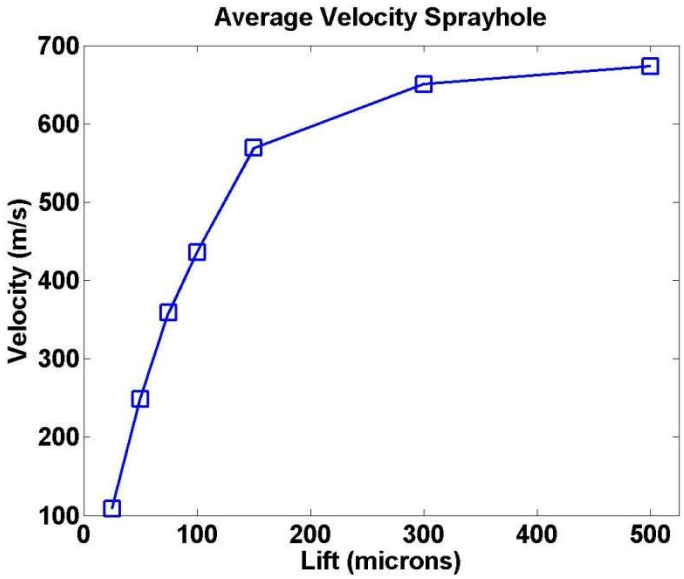

Figure 25. Average Spray Hole Velocity vs. Lift

The velocity correlates well with the mass flow rate (Figure 26) with the relative differences between the lifts resulting from the low lifts having a higher vapor fraction at the exit and a correspondingly lower average density upon exit.

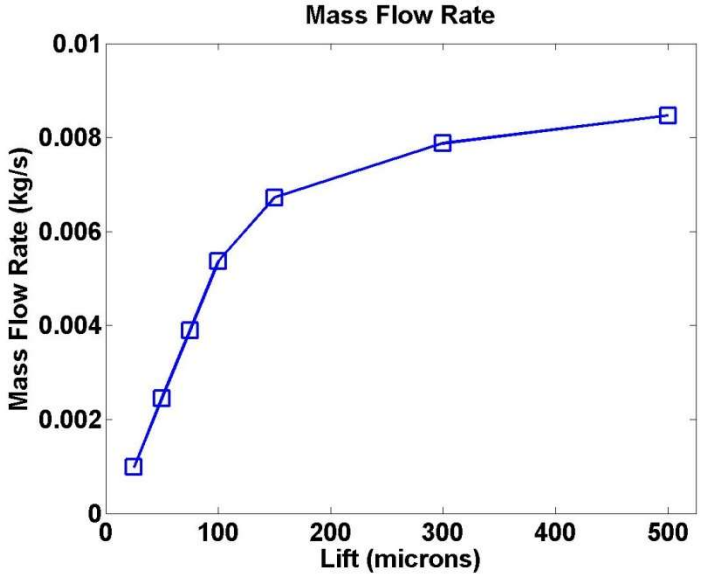

Figure 26. Mass Flow Rate vs. Lift

The lower pressure within the sac also creates a lowered lift force that acts on the needle (Figure 27) that follows the same approximate trend.

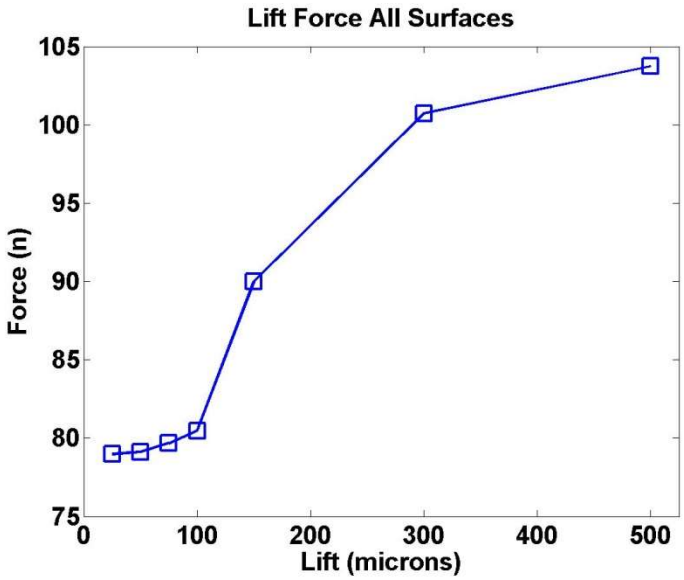

Figure 27. Total Lift Force vs. Lift

The lowered lift force is a direct result of the lowered sac pressure which is further evidenced when the forces are separated into those acting on the surfaces located within the sac and seated area (Figure 28) and those above it (Figure 29). The forces on the lower surfaces increase with an increasing sac pressure while those on the upper surfaces vary by less than .2% over the various lifts.

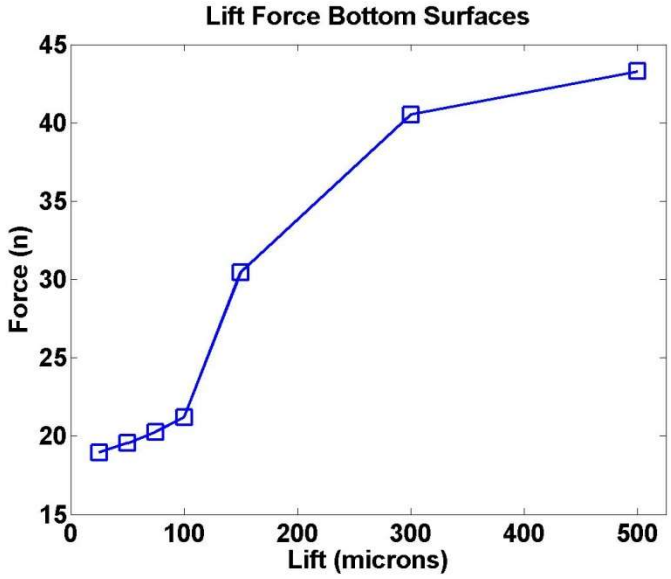

Figure 28. Bottom Surfaces Lift Forces vs. Lift

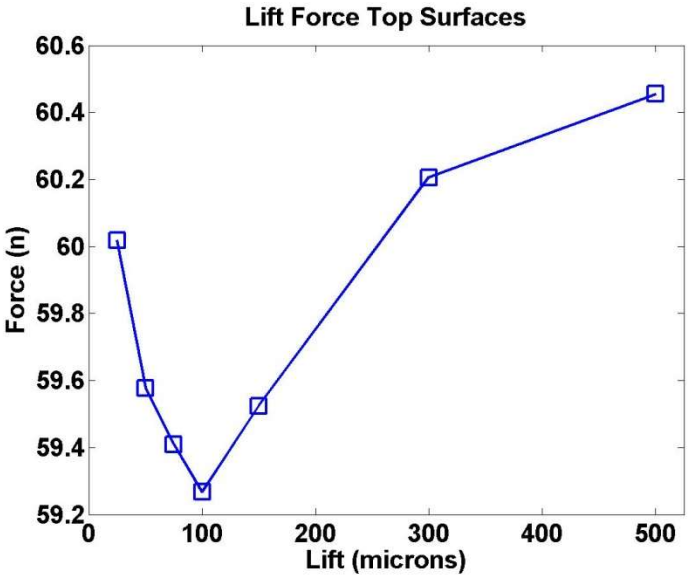

Figure 29. Top Surfaces Lift Forces vs. Lift

The vapor volume within the sac decreases with the increasing lift (Figure 30) with the pressure increase at the higher lifts eliminating the presence of vapor. The singular discrepancy occurs at lifts of 75 and 100 microns. This is a result of the smaller recirculation area at the 100 lift (Figure 18) increasing the stagnated flow at the interface between the seat and the sac which increases the amount of vapor created at this intersection (Figure 19).

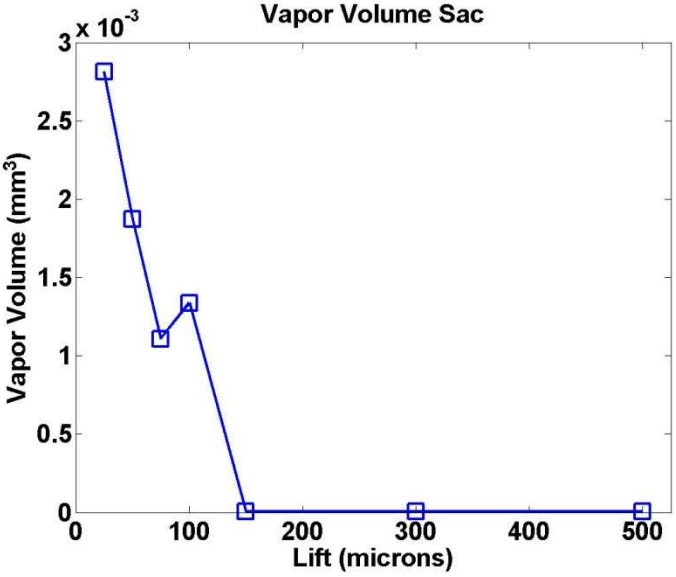

Figure 30. Sac Vapor Volume vs. Lift

The vapor within in the spray hole follows two downward trends (Figure 31). The first trend occurs with vapor forming along the bottom of the spray hole and decreases from the maximum amount of vapor towards a minimum that occurs as the turn in the flow is almost centered on the spray hole. There is an increase in the vapor generation as the flow starts to separate over the upper surface of the spray hole. The amount of vapor decreases as the lift increases as the increased pressure limits the amount of separated flow within the spray hole.

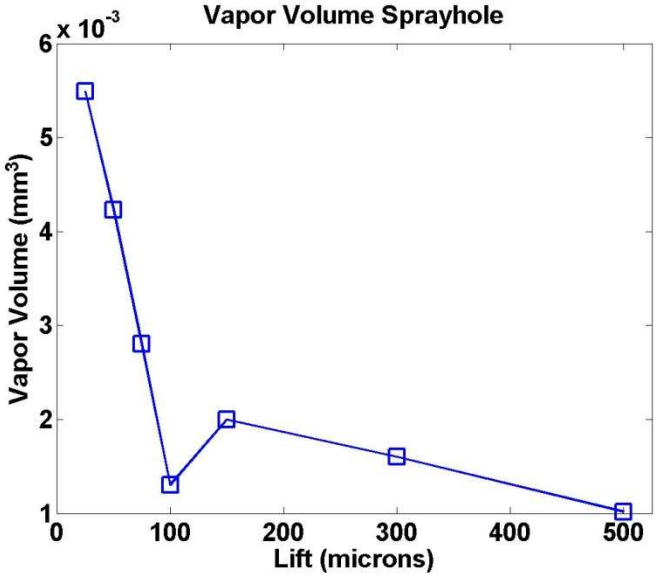

Figure 31. Spray Hole Vapor Volume vs. Lift

VIII. TRANSIENT HOVERING RESULTS

For this study the forces are broadly separated into the lateral and lifting forces where a lifting force is parallel to the direction of the needle vertical displacement, marked as the lift in (Figure 13). The lateral forces are defined as the forces that are perpendicular to the needle's vertical displacement and are presented as a magnitude and a direction.

A. Surface 1 Lateral Forces

Figure 32 shows the lateral force on the needle tip (surface 1 in Figure 13) and the total lateral force on the needle. From this figure two conclusions can be drawn. The simulation that used the DES turbulence model was able to capture the high frequency fluctuations that RANS simulation missed, and the magnitudes of the low-speed fluctuations are larger by ~100% on surface 1 and ~40% overall in the DES simulation.

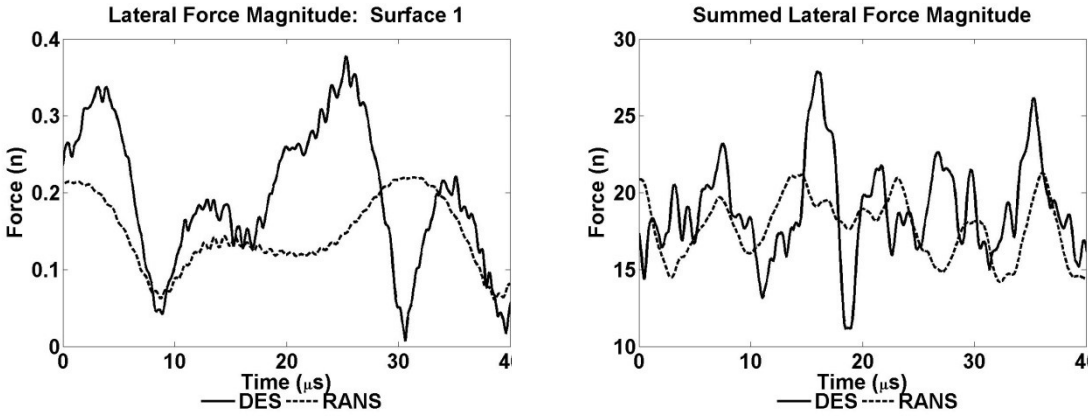

a) Surface 1 b) Total

Figure 32. Comparison of the lateral force for the DES and RANS simulations on a) surface 1 and b) the summation over all the surfaces

These results agree with the conclusions of Constantinescu et al. [37, 38] that DES simulations can capture high frequency fluctuations not seen in the RANS simulation and predict higher peak fluctuations.

Figure 33 displays the lateral force history on the tip of the needle (surface 1 in Figure 13) with points correlating to a low, medium and high lateral force for both simulations that correspond to the pressure contours shown in Figure 34

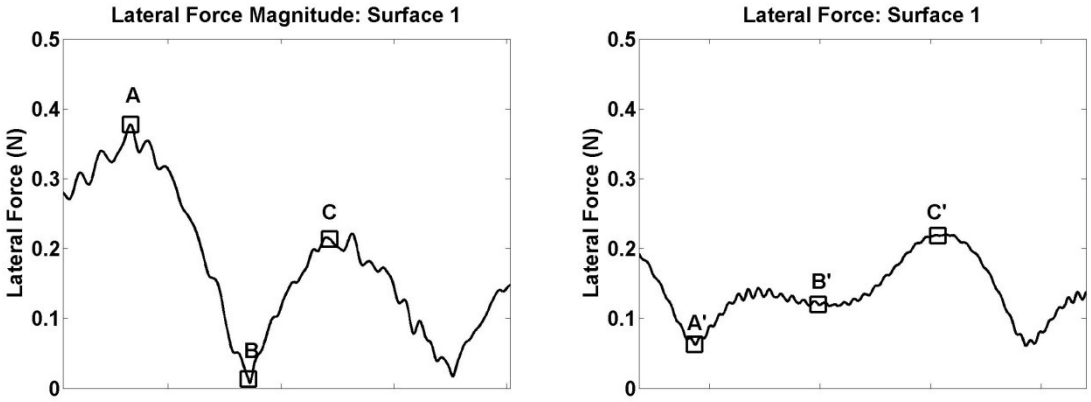

Figure 33. Lateral force history on the needle tip with points marked for figure 12

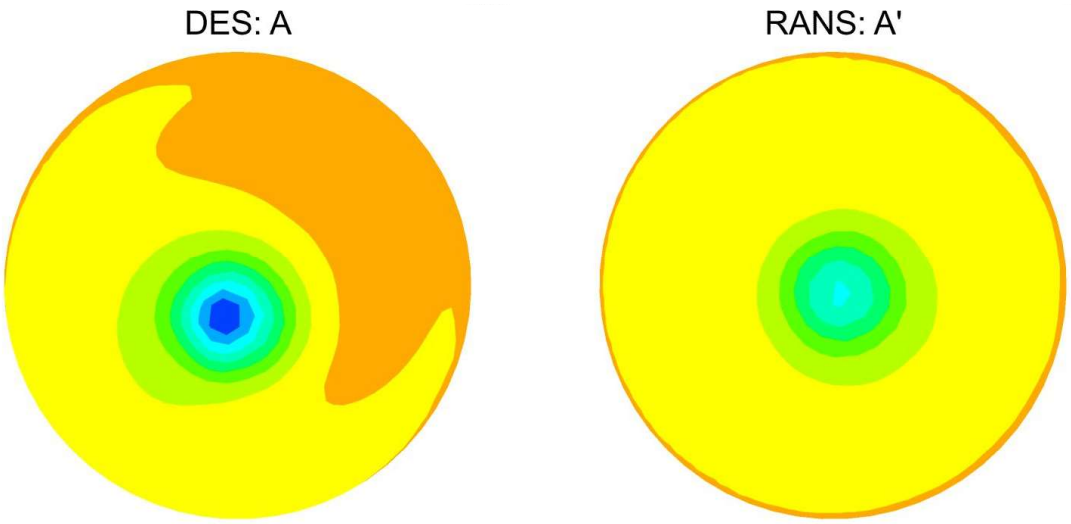

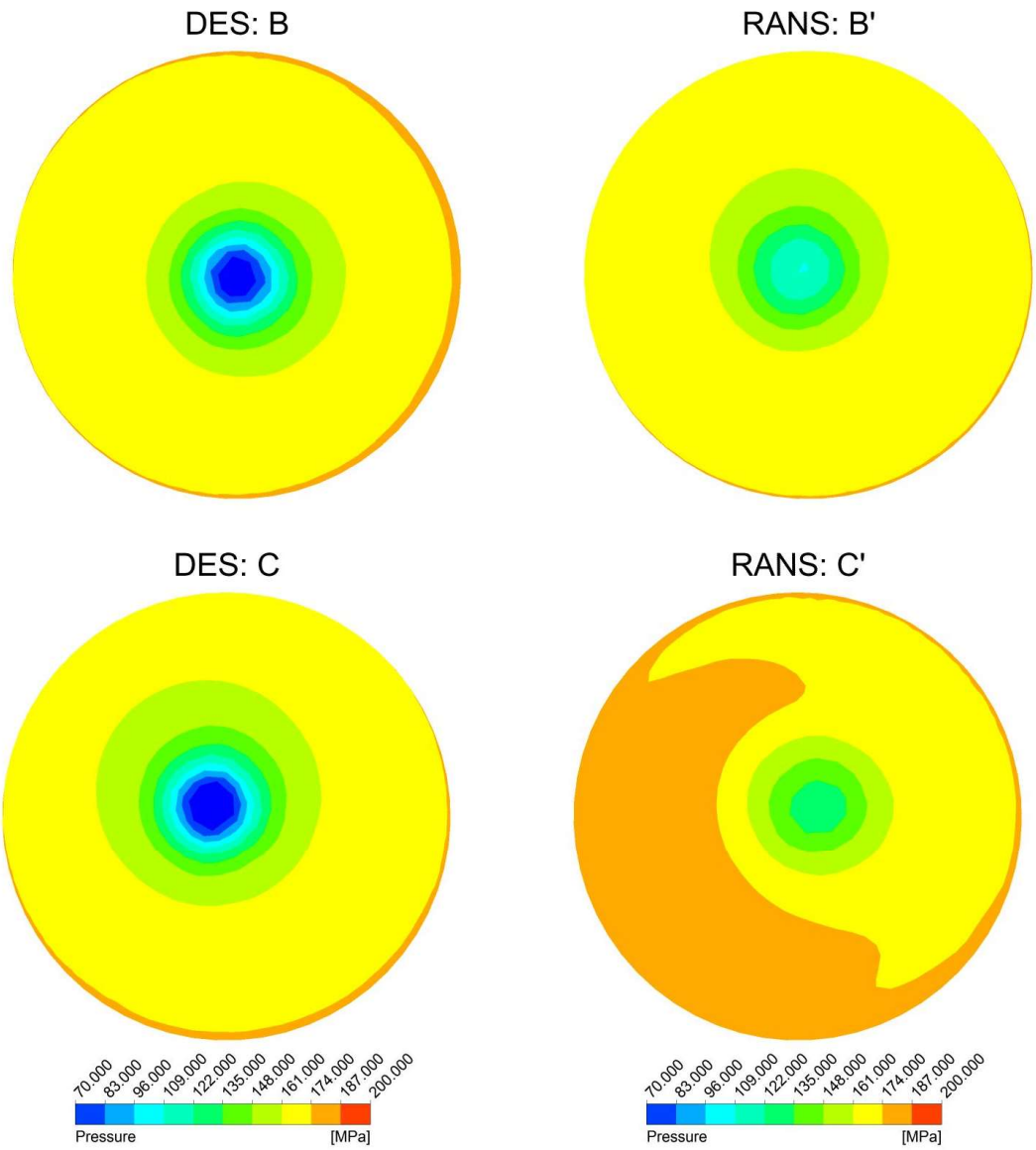

Figure 34. Pressure contours on surface 1 showing the correlation between the offset inception point and the lateral force magnitude in the DES and RANS simulations. For these simulations the inception point predicted using the RANS turbulence model deviates much less from the center than in the DES simulation.

The pressure contours indicate two distinct differences between the turbulence models related to the point of minimum pressure. The DES simulation predicts overall lower pressure acting on the surface as well as predicting that the point where the minimum pressure occurs deviates more from the center of the surface. The lower pressure do not contribute to the lateral force trends seen in Figure 14 only impacting the lifting forces

(Figure 35) by predicting a lower lifting force for the DES simulation when compared to the RANS simulation.

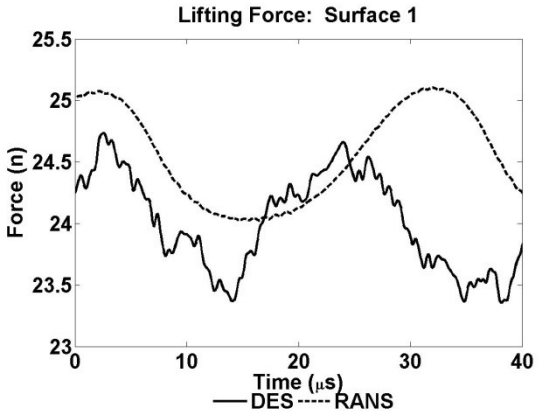

Figure 35. RANS and DES comparison of the lifting force on surface 1 show that the DES simulation predicts a lower lifting force due to the lower minimum pressure

The lateral force instead correlates to the location of the minimum pressure which is created by how the flow rolls up inside the sac. This rollup is visually represented by using the Q-criterion [90] which defines the rolled up portions of the flow as areas where the second invariant of $\nabla \vec{u}$ is positive indicating that the local vorticity magnitude is greater than the strain rate. Figure 36 shows the vortical roll up inside the sac for the two turbulence models. Both models predict that the location of the minimum pressure on surface 1 is at the point of inception for the vortical rollup.

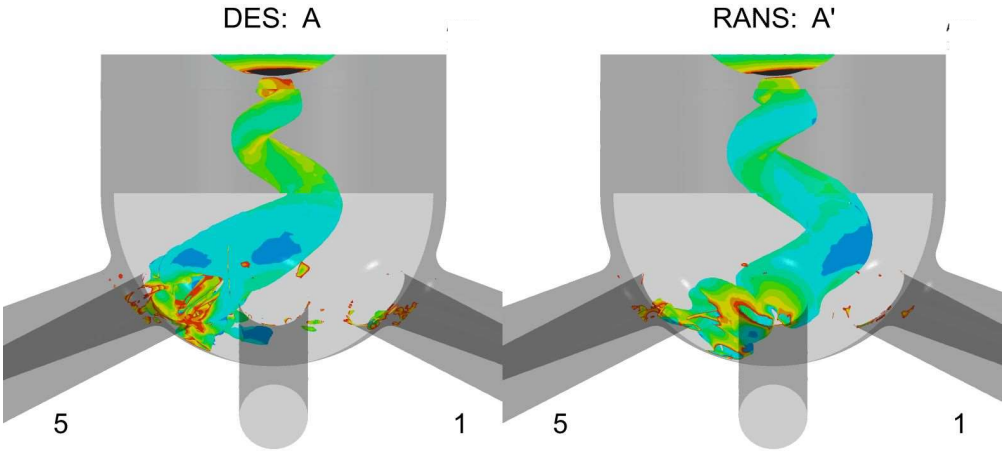

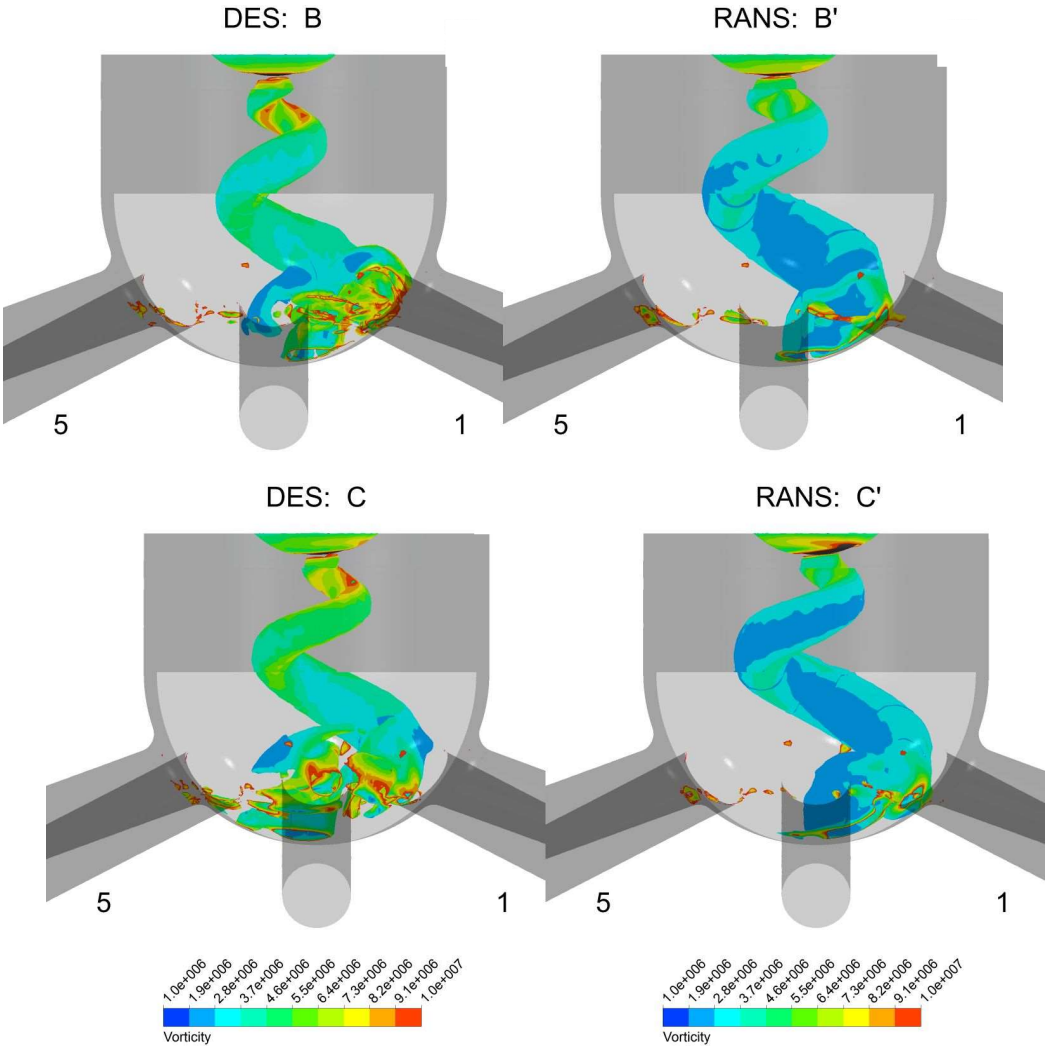

Figure 36. Comparison of iso-surface of the Q criteria (>0.01) between the DES and RANS at time instances of a) high lifting force, b) middling lifting force and c) minimum lifting force with the orientations marked for spray hole 1 and 5. The greyscale is based on the vorticity magnitude.

For this study the inception point of the rollup is defined as the location of the minimum pressure on surface 1. The lateral displacement is the magnitude of the coordinate in in XZ plane which are displayed in Table 3.

	Magnitude of Deviation for the inception point (μm)	
	DES	RANS
Point A	31.28	7.00
Point B	3.11	7.05
Point C	17.90	20.76

Table 3. Summation of the magnitudes of the deviation from the center for the inception points at the points shown in Figure 33.

The maximum deviation of the inception point for the DES simulation is approximately 50 % larger than in the RANS simulation. This corresponds to larger maximum lateral forces predicted by the DES simulation compared to the RANS simulation. In addition, there is a strong correlation between the deviation of the inception point from the center and the magnitude of the lateral force. A higher deviation from the center corresponds to a larger the magnitude for the lateral force. The correlation between the higher deviation and lateral forces in the DES simulations suggests accurately capturing the inception point of the vortical rollup is important to be able to accurately predict the lateral deflections of the injector needle. A difference between the DES and RANS is that the magnitude of the vortical roll up predicted by the RANS decreases much faster than that by the DES (Figure 36). This is consistent with previous studies in the simulation of flow over bluff bodies [37, 38] where the spatial filtering used in RANS can artificially dampen out the trailing vortices. Because of the quicker dampening of the vorticity the RANS simulation has less interaction between the portions of the rolled-up flow that are opposite on another. Figure 37 shows the out of plane vorticity contours plotted on a log scale. It is clear there is an identifiable column in the RANS simulation at the center of the sac that the vortical structure develops and rotates about which isn't present in the DES simulation. As a result, the inception point of vortical structure deviates from the center of the needle, leading to higher fluctuations in the lateral force in the DES simulation.

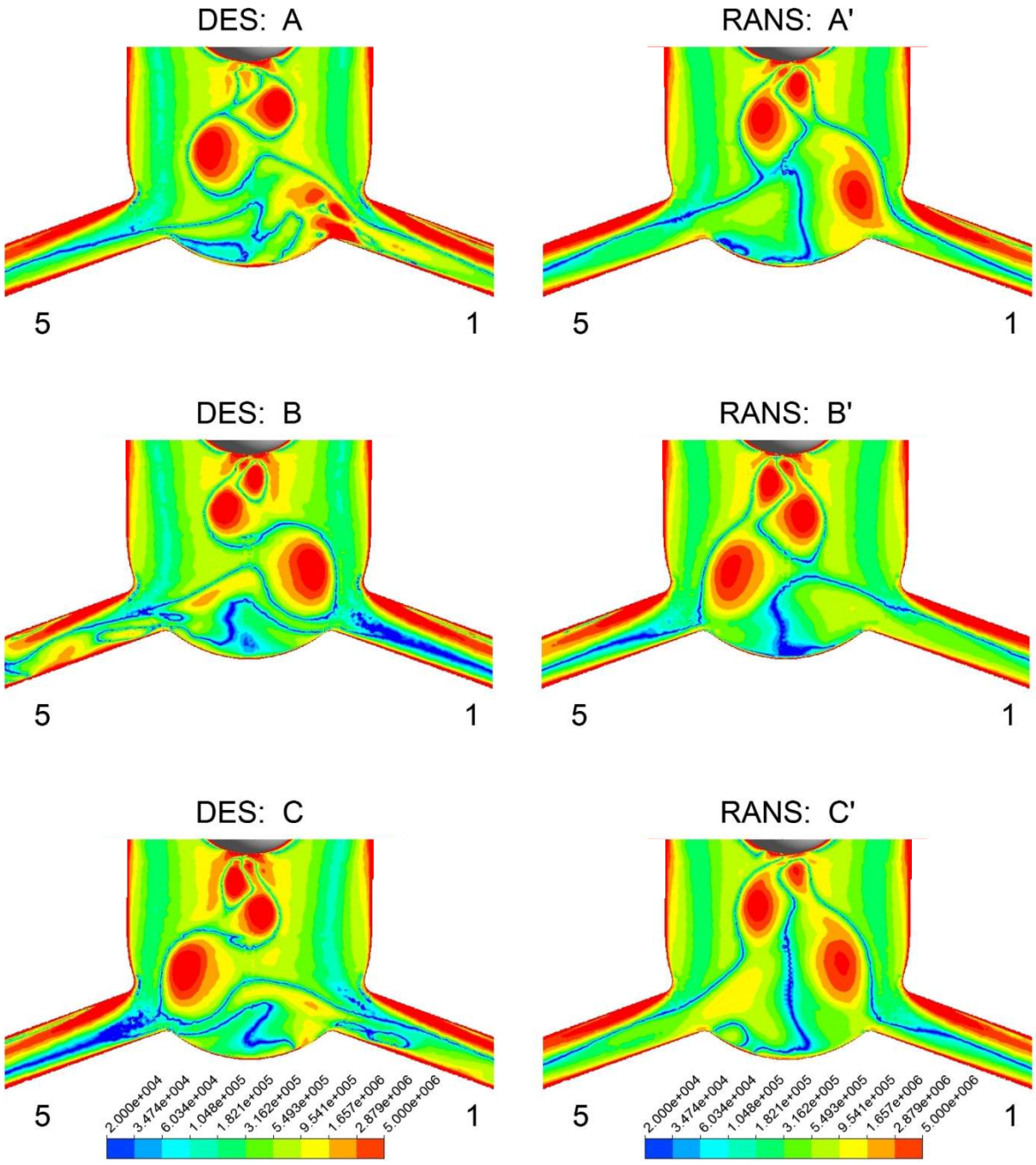

Figure 37. Out of Plane Vorticity Magnitude showing the persistent vertical axis of rotation in the RANS simulation that is not present in the DES simulation

B. Surface 2 and 3 Lateral Forces

The lateral forces (Figure 38) on Surfaces 2 and 3 exhibit similar trends that are driven by the vortical rollup shown in Figure 36. As expected, the fluctuations are much larger in the DES simulation however when a moving average is applied to the forces in the DES simulation (Figure 39) the trends between the two simulations are similar.

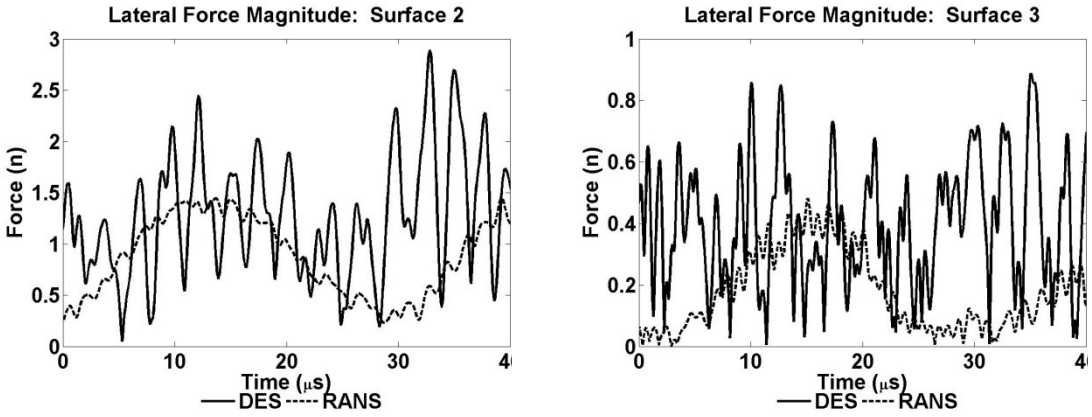

Figure 38. Comparison between the lateral force in the RANS and DES for surfaces 2 and 3

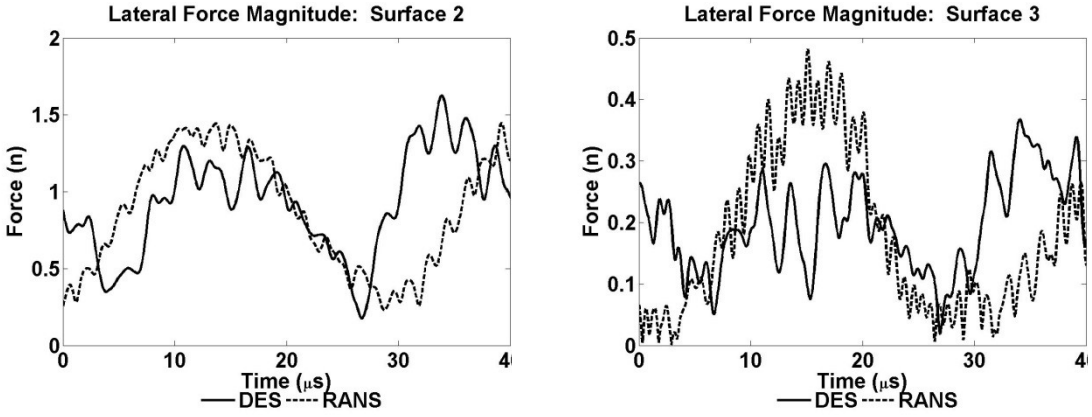

Figure 39. Comparison between the lateral force in the RANS and DES for surfaces 2 and 3 with a moving average window of 2.5 microseconds applied to the DES simulation

When the high frequency fluctuations are averaged out the magnitudes and trends predicted by the two simulations are similar. For these surfaces the lateral forces are directly impacted by the speed that the vortical rollup shown in Figure 36 rotates at. For this analysis a swirling speed is defined in this paper as the volume average lateral speed of the flow inside the sac and calculated as:

$$\text{Swirl Speed} = \frac{\sum_{Sac} V \cdot \left(\sqrt{u_x^2 + u_z^2}\right)}{\sum_{sac} V} \tag{87}$$

Figure 40 compares the swirling speed and the lateral forces on these two surfaces and shows that there is a positive correlation between the two variables. Periods of high swirling speed correlate to larger magnitudes in the lateral forces and the periods of lower swirling speeds correlate to lowered lateral forces.

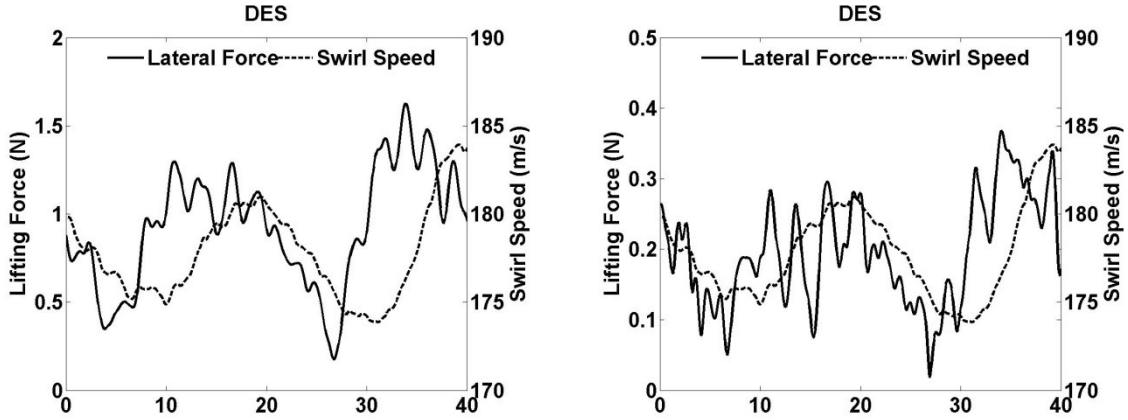

Figure 40. Comparison between the lateral forces on surfaces 2 and 3 and the swirling speed inside the sac showing that the swirling speed is proportional to the magnitude of the force

C. Spray Hole Vapor

This next section explores the vapor volume within the spray holes. For these simulations there were only slight differences between the vapor predictions for the RANS and DES simulation (Figure 41) so the remainder of the section only shows the results from the DES simulations.

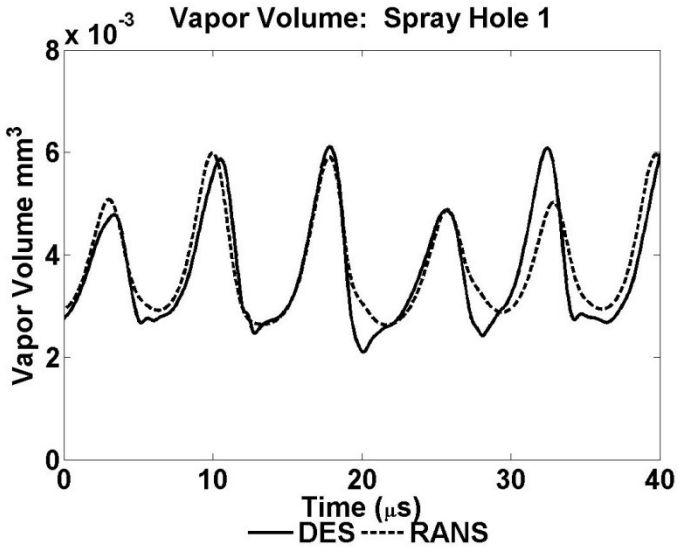

Figure 41. Comparison between the vapor generated in a single spray hole in the DES and RANS simulations. From this graph it was determined that there is no significant difference between the predicted vapor generation.

Figure 42 shows the vapor volume for three of the spray holes all of which show the same trend with a phase difference between them.

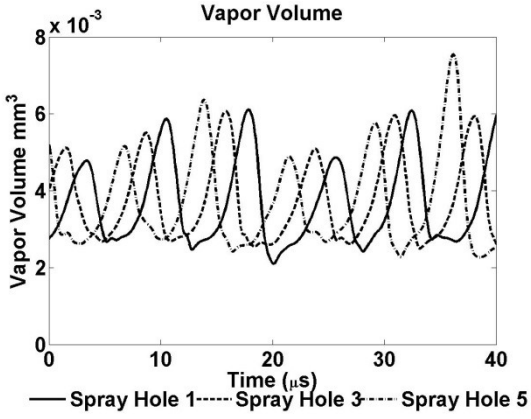

Figure 42. Vapor Volume in spray holes 1 and 3 and 5 for the DES simulation.

The peaks and the phase difference are caused by the rollup shown in Figure 36. Figure 43 shows the vapor formation within spray holes 1 and 5 which are on opposite sides of the sac. These spray holes have opposite trends. When spray hole 1 has a maximum vapor volume spray hole 5 is near a minimum. This is caused by the vortical rollup which, when it covers one of the holes, leave the hole on the opposite side completely uncovered.

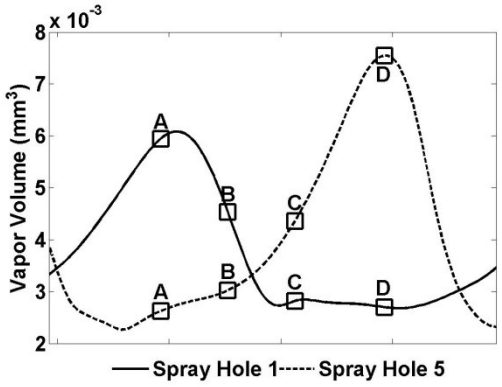

Figure 43. Vapor volume within spray holes on opposite sides of the sac over a singular peak with markers indicating the time instances used for figure 18

The cause of the peak vapor generation is how the flow enters the spray hole due to the flow blockage created by the vortical structure. Figure 44 shows the velocity contours and vapor fraction at the points indicated by Figure 43. When the spray hole 1 is covered by the rolled-up flow at point A the flow enters the spray hole at a sharper angler with a higher velocity. This creates a large flow separation at the top of spray hole 1 which leads to a large formation of vapor. Point C shows when the rolled-up formation is over spray hole 5. At that point in time the flow enters spray hole 5 does so at a steeper angle and with a larger velocity leading to a higher formation of vapor. Spray hole 1 has more even velocity profile at the spray hole entrance which leads to less separation in the flow and a lower amount of vapor generation.

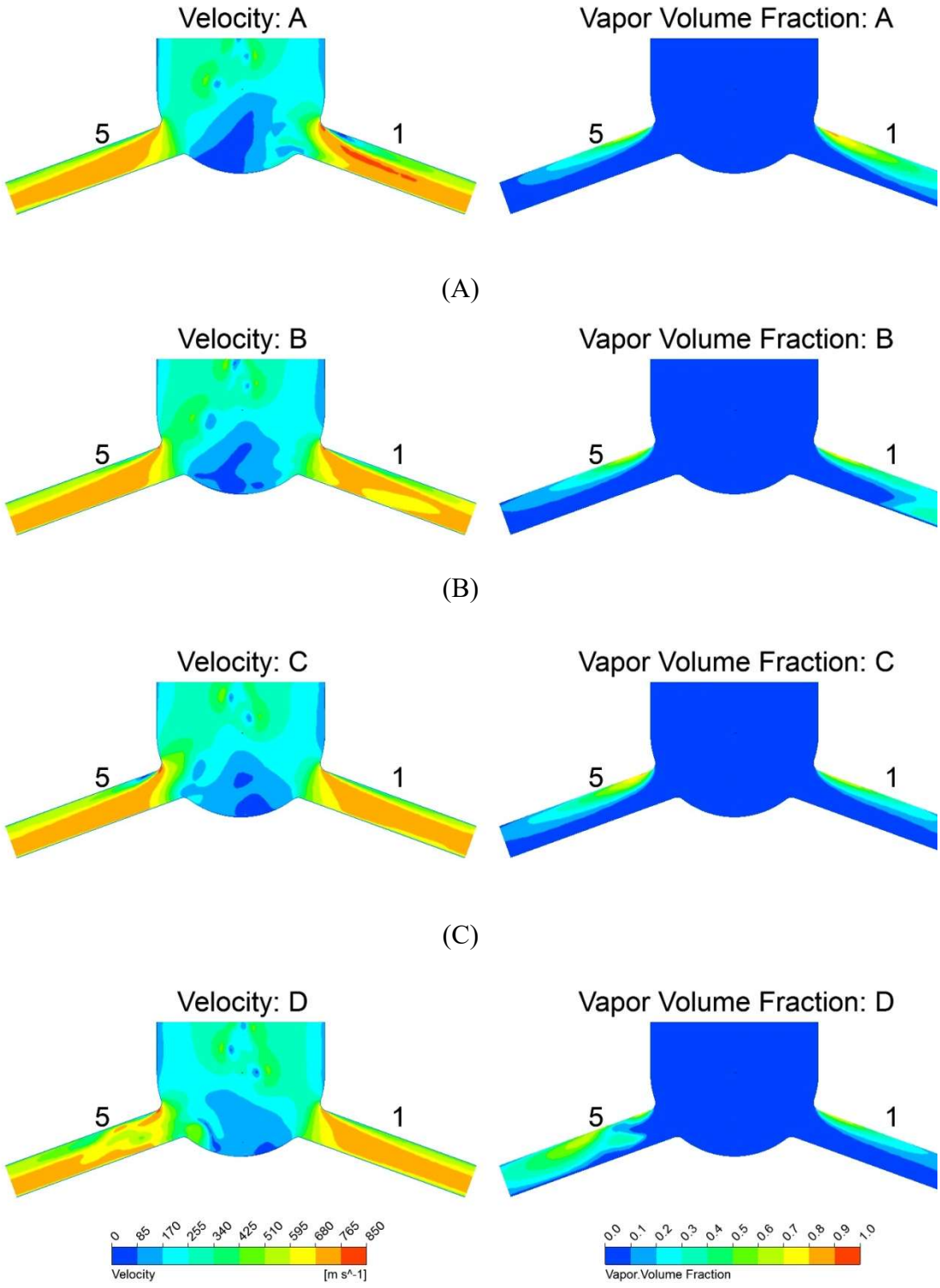

Figure 44. Side-by-side plots of the velocity and vapor volume fraction at time instances indicated in figure 18 showing fluctuations in the vapor volume as the vortical rollup passes over the spray hole.

D. Outlet Mass Flow Rates

The mass flow rate ends up being largely dependent on the vapor volume within the individual spray holes. Figure 45 shows the comparison between the vapor volume and the mass flow rate for the spray hole 1 in the DES simulation which shows that not only do the peaks for the vapor volume match up with the local minimums for the mass flow rates but the magnitude of the vapor volume peaks aligns with the magnitude peaks for the mass flow rate minimums.

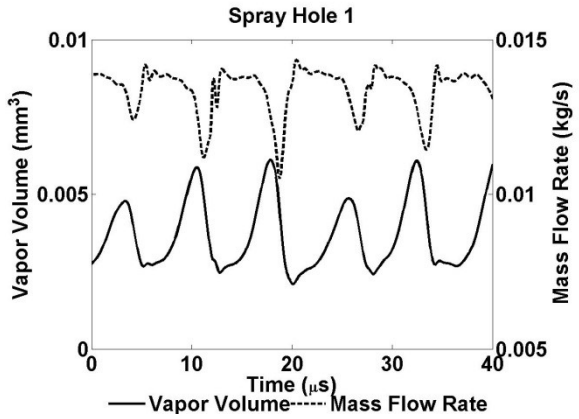

Figure 45. Vapor Volume and Mass Flow Rate for spray hole 1 in the DES simulation showing an inverse relationship between the two flow variables

The vortical structure therefore represents a key contributor to hole to hole variation during injection cycles.

IX. FSI SIMULATION AT HOVER

This section details the FSI simulation that was performed and simulates the hovering phase of the injection. This simulation was performed for an unbalanced injector (Figure 46) because the needle motion for these simulations are simpler than that of the flow balanced injector, which rotates, and allowed simplified boundary conditions to be applied that reduced the computational time required.

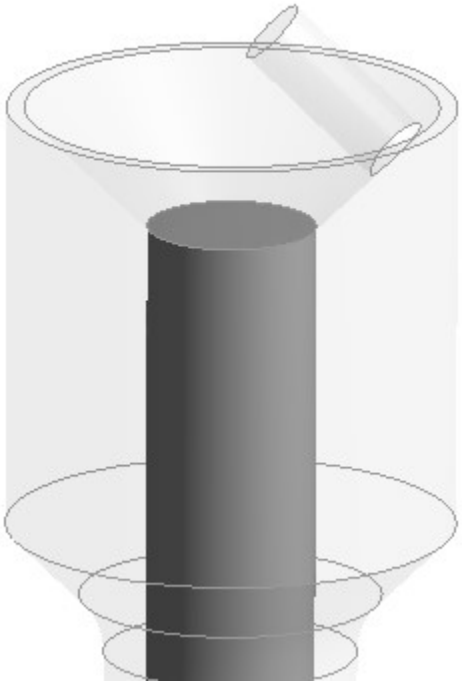

Figure 46. Unbalanced injector gain orifice.

High speed x-ray imaging [91, 92] of the needle motion during operation has shown that the needle motion occurs in a singular plane. Analysis of the lateral forces from the transient simulations at hover (Figure 47) indicated that the motion is predominantly in the plane that is aligned with the gain orifice.

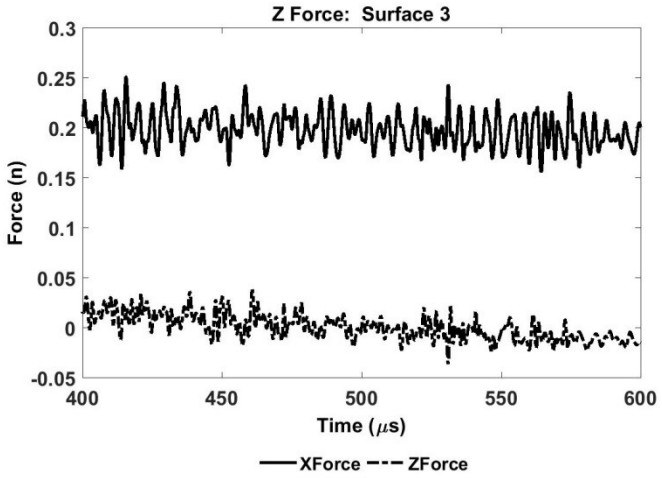

a) Surface 3 force comparison

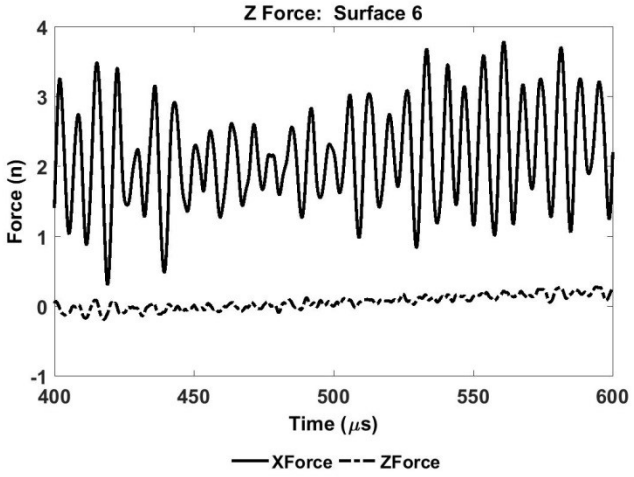

b) Surface 6 force comparison

Figure 47. Comparison of the forces in line with the gain orifice (X-direction) and perpendicular to the gain orifice (Z-direction) on surfaces a) 3 and b) 6. On both surfaces the magnitude of the forces are much larger in the x direction.

These simulations were simplified by imposing boundary conditions that limited the bending motion to this plane. Figure 48 shows the constraints imposed to the points on the XY plane.

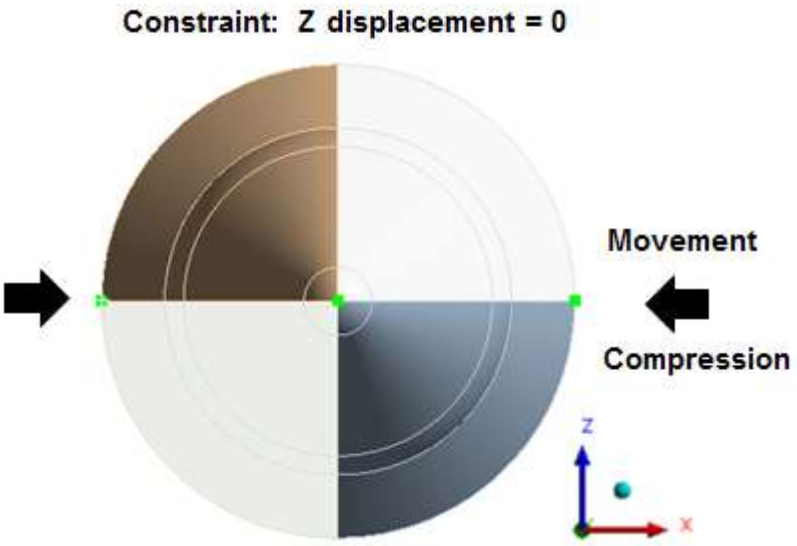

Figure 48. Boundary conitions imposed on the points in the XY plane.

A. Vertical Compression

The injector needle experiences two modes of deformation; initially the needle is compressed by the surrounding pressure. It is then bent due to imbalances in the pressure on the surfaces due to the surrounding flow. The surrounding pressure compresses the injector shortening it by approximately 14 microns (~2.5% of the lift at hover). This compression occurs over a short time relative to the total time of the lift cycle (Figure 49) after which the oscillations in the displacement are the result of the bending motion.

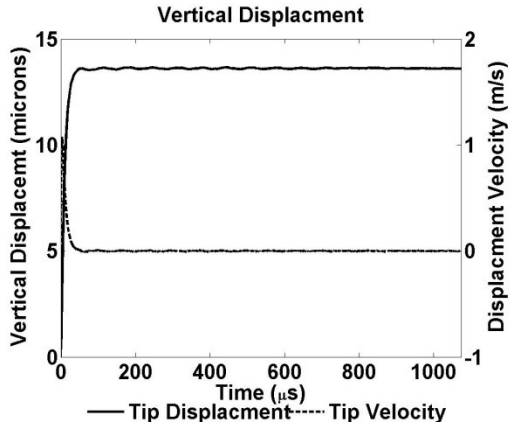

Figure 49. Vertical displacment measured at the injector tip over the full cycle.

The compression of the needle occurs within the first 40 microseconds of the simulation (Figure 50), however this is for a simulation where time t=0 corresponds to a fully opened injector. In real world applications the compression would occur over a longer time due to the lower sac pressure when the seat clearance is less than fully opened (Figure 16 and Figure 21). Studies[1] have found that during the closing the needle is compressed beyond what occurs during the opening and hover phase.

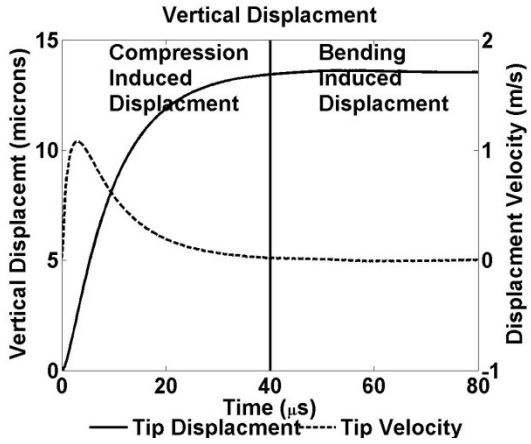

Figure 50. Vertical displacement measured at the injector tip over the full cycle

B. Lateral Displacement

The simulation shows that needle undergoes a bending induced displacement (Figure 51) and conforms with the measurements made by [91, 92] in that the maximum displacement is matched, the motion is to a singular side and does not return to the center. The amplitude declines over the cycle indicating that if the needle was allowed to hover indefinitely it would reach an equilibrium point. The time required to do so would be much greater than the operational time.

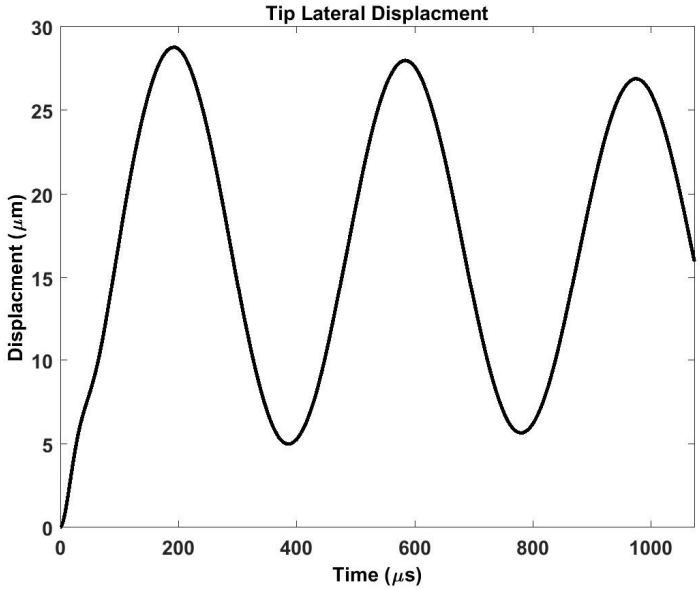

Figure 51. Lateral displacement measured at the tip over the full cycle.

This deformation is shown in Figure 52 at a true scale and in Figure 53 at a 5x scale

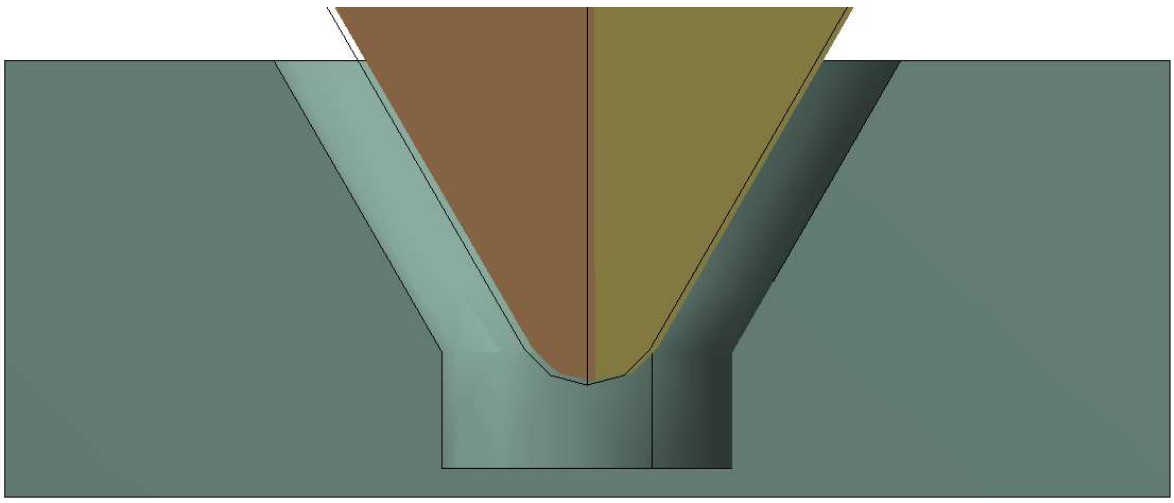

Figure 52. Displacement of the needle compared to the undeformed wire frame at a 1x scale.

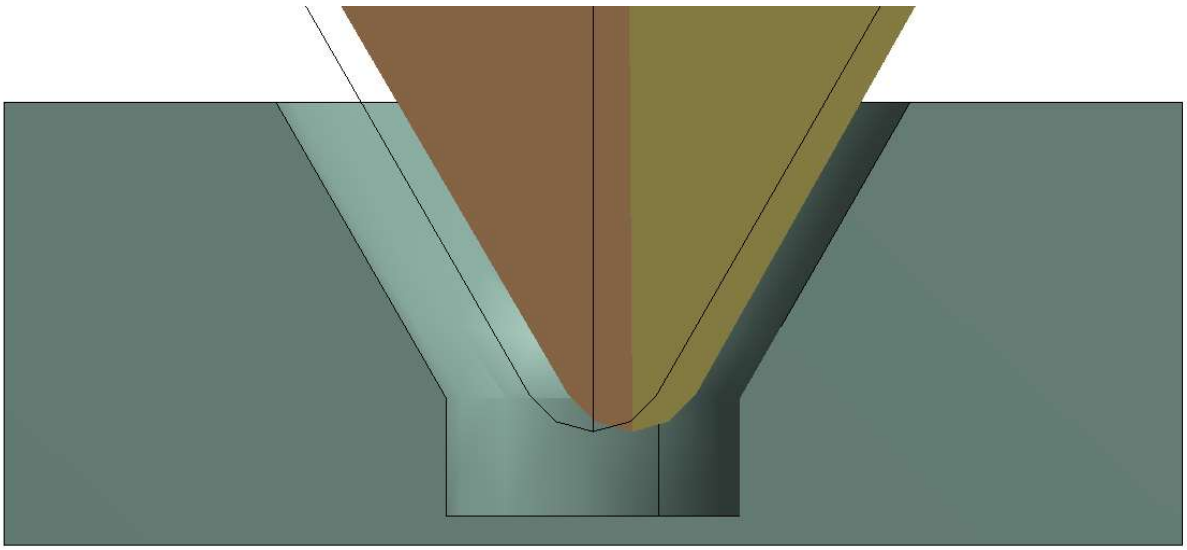

Figure 53. Displacement of the needle compared to the undeformed wire frame at a 5x scale.

This displacement is caused by an imbalanced force along the shaft of the needle. For simplicity the forces are reported as sums on each of the 6 faces of the needle (surfaces 1-3 are shown in Figure 13 and surfaces 4-6 are shown in Figure 54). Figures 48-52 show the forces on the different surfaces as well as the sign of the resultant force associated with the displacement.

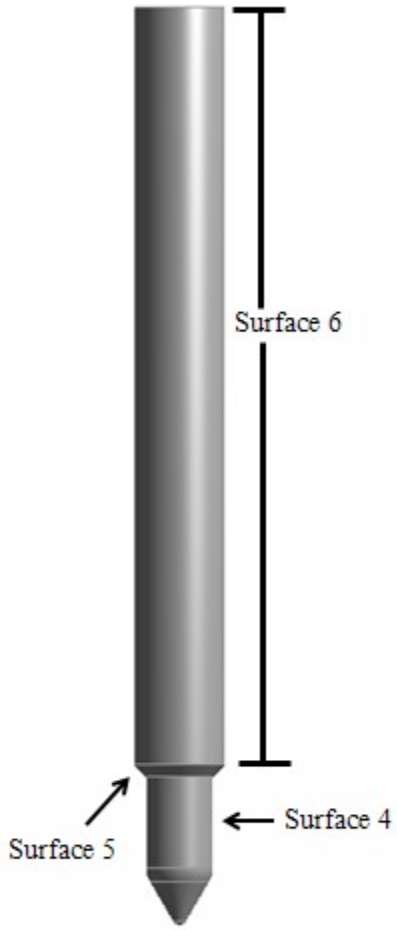

Figure 54. Diagram showing the locations of surfaces 4-6.

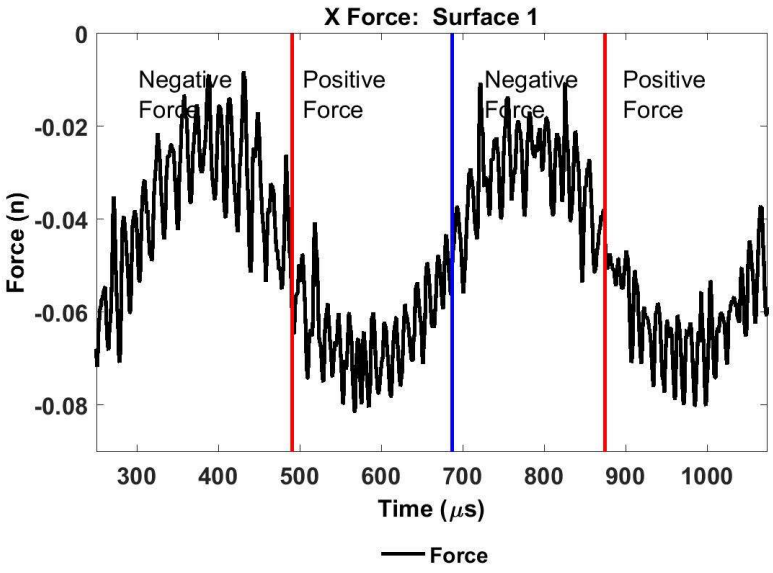

Figure 55. Force in the X direction on surface 1.

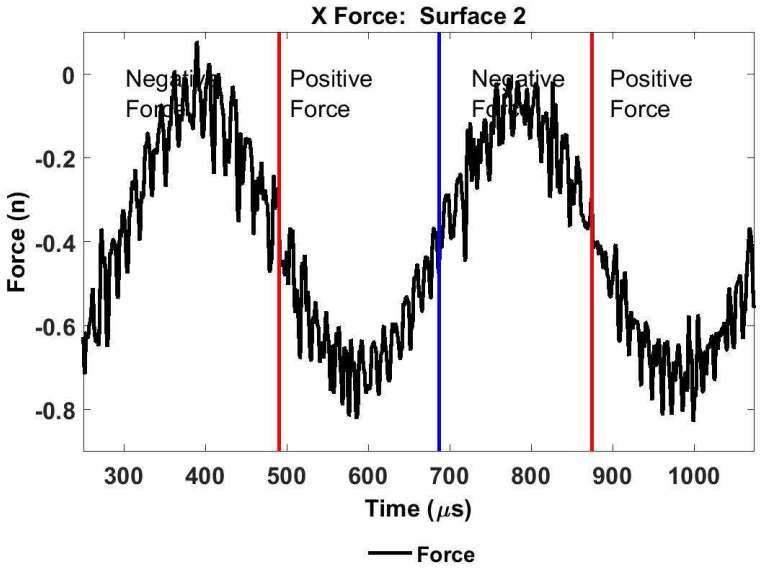

Figure 56. Force in the X direction on surface 2.

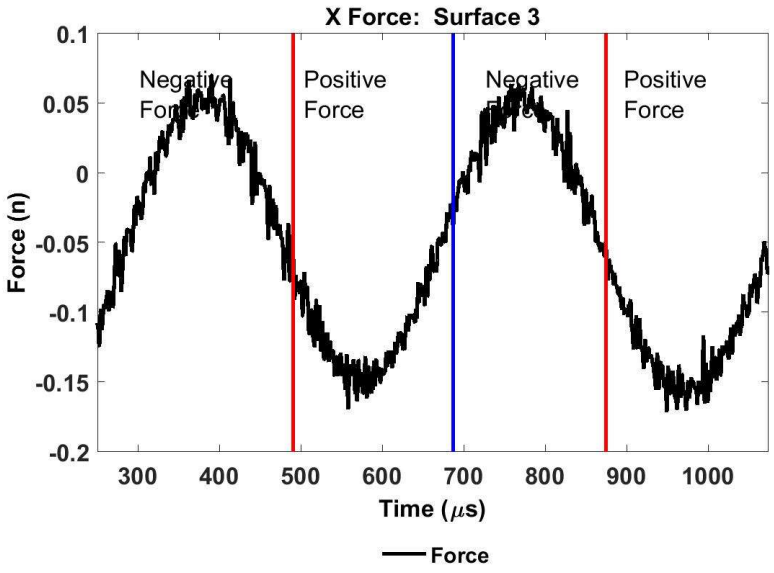

Figure 57. Force in the X direction on surface 3.

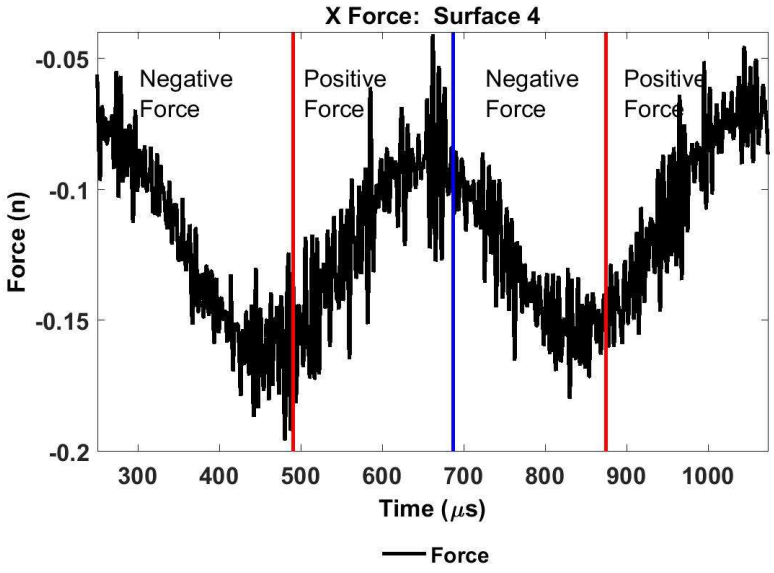

Figure 58. Force in the X direction on surface 4.

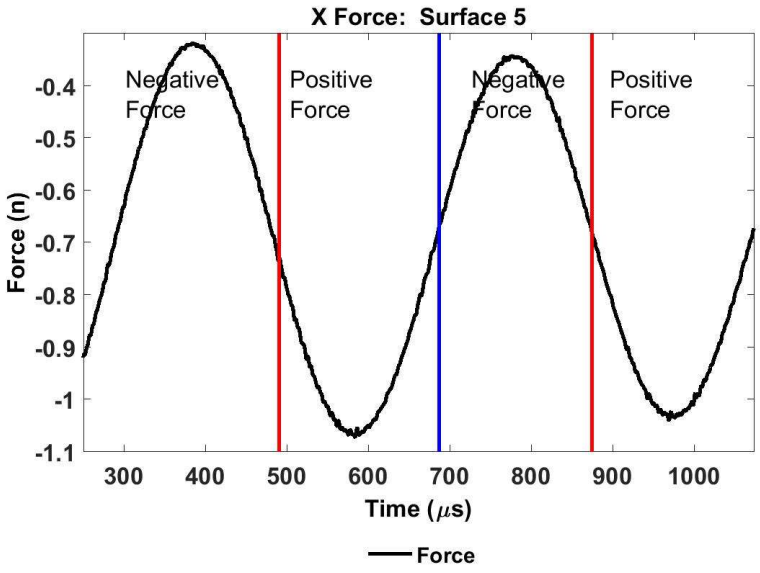

Figure 59. Force in the X direction on surface 5.

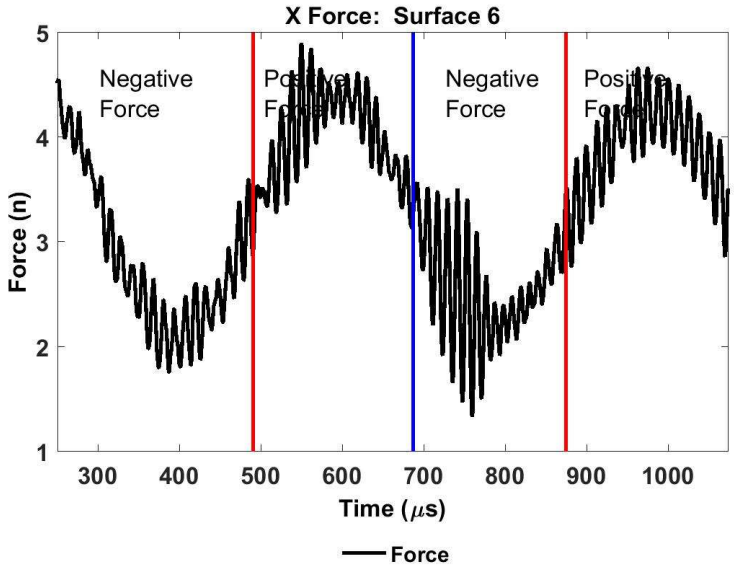

Figure 60. Force in the X direction on surface 6.

From these figures it becomes apparent that the displacement is directly affecting the forces on surfaces 1-5. On these surfaces the forces are at their local minimums when the resultant force suggests that the force driving the motion should be at a local maximum. It's only on surface 6 that this is true which suggests that the pressure differential on this

surface drives the motion at hover and the pressure differentials on the other surfaces are driven by the deflection.

C. Mass Flow Rates

This section details the mass flow rates through the individual spray holes during the simulation. All mass flow rates and volume fractions have been filtered using a moving window of 10 microseconds. Figure 61 shows the unfiltered mass flow rate for spray hole 1 and Figure 62 shows the same figure only with the filter. Also plotted on these graphs is the change in the distance between the needle tip and the center of the entrance to the spray hole. Negative displacements on these figures indicate that the needle is moving away from the spray hole. Figure 63 shows the mass flow rate and distance for spray hole 5 which is opposite spray hole 1.

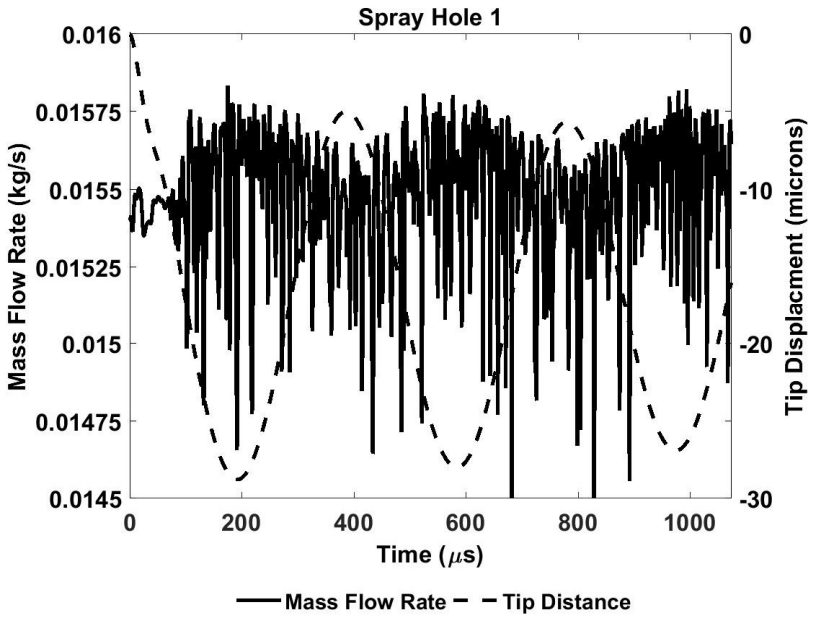

Figure 61. Unfiltered mass flow rate for spray hole 1.

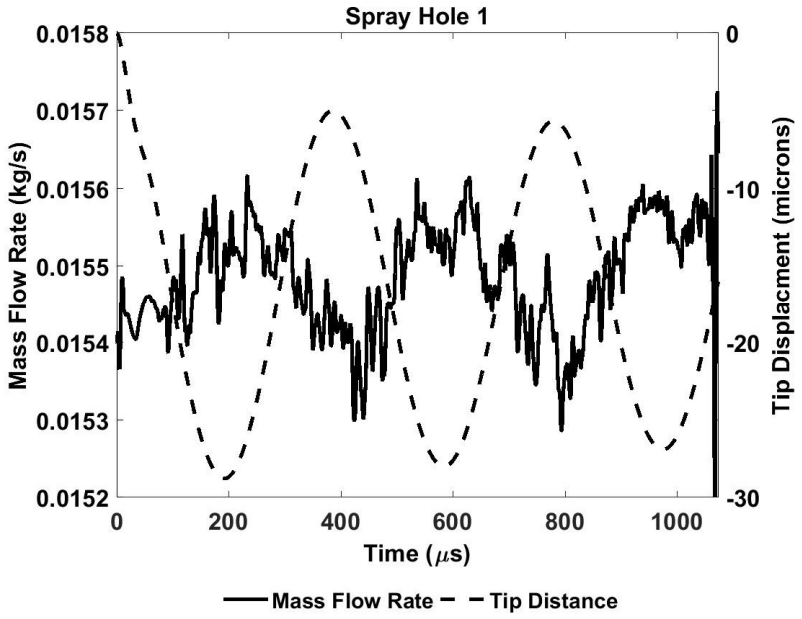

Figure 62. Filtered mass flow rate for spray hole 1 compared with the distance between the tip and the center of the spray hole entrance

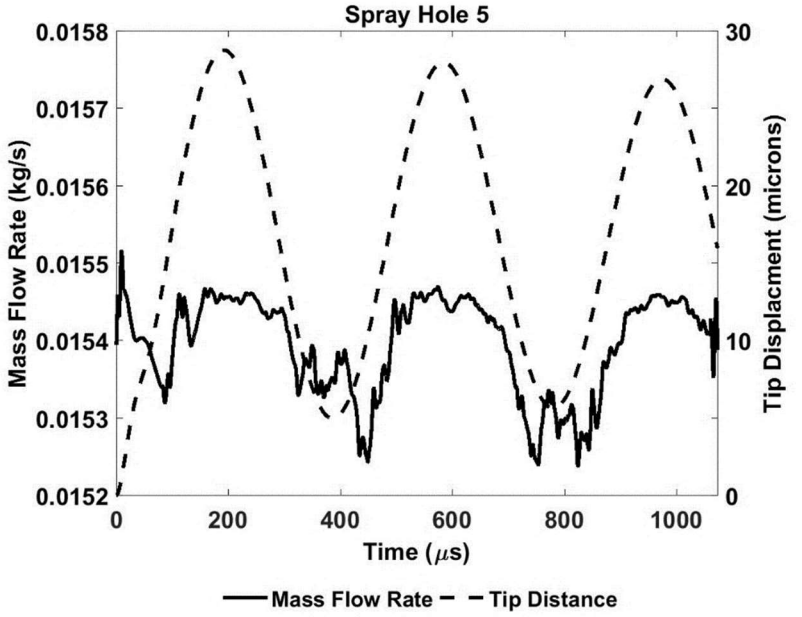

Figure 63. Filtered mass flow rate for spray hole 5 compared with the distance between the tip and the center of the spray hole entrance

Comparisons of Figure 62 and Figure 63 indicate that there is no correlation between the displacement of the tip and the mass flow rates. Both mass flow rates increase and decrease regardless of if the needle is moving towards or away from the spray hole. When these simulations are compared to a non-FSI simulation there does appear to be some

slight increases in the mass flow rates for both spray holes (Figure 64 and Figure 65) which suggests that the compression of the needle has reduced the friction losses as the flow enters the sac and has increased the average pressure in the sac which would lead to increased exit velocities through the spray holes. These increases are approximately 1% over the period which is negligible.

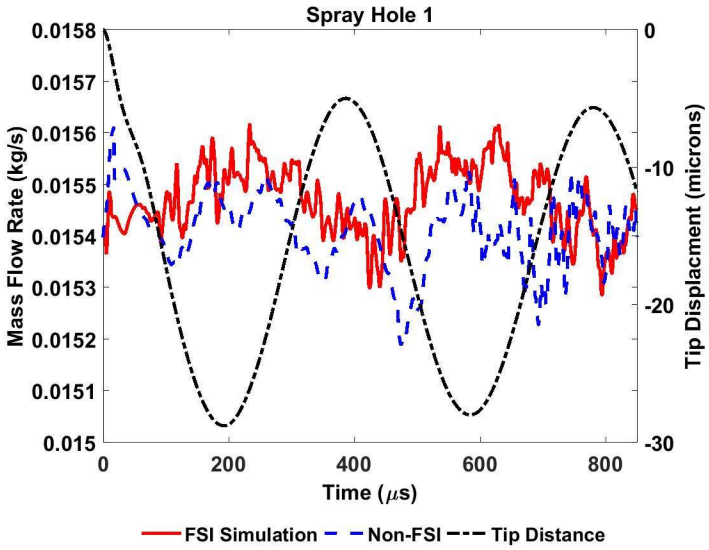

Figure 64. Comparison between the mass flow rate out of spray hole 1 with and without the structural displacement.

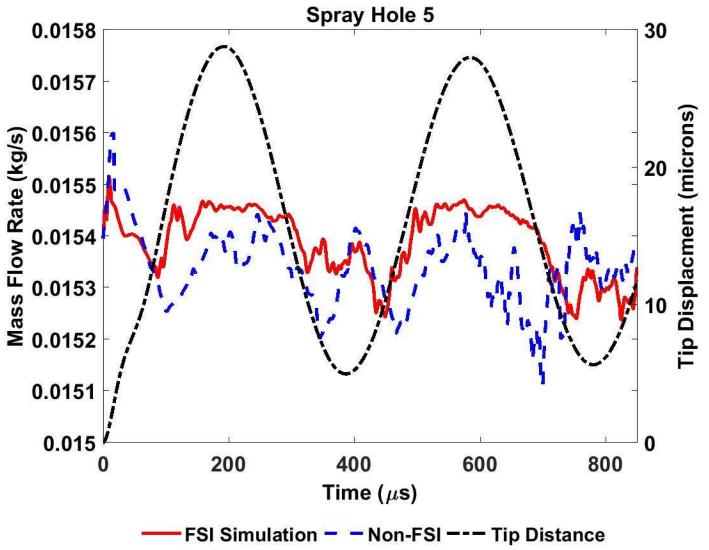

Figure 65. Comparison between the mass flow rate out of spray hole 5 with and without the structural displacement.

D. Vapor Volume Fraction

This section details the change in the vapor volume in the spray holes. In the spray holes that are perpendicular to the needle plane of movement there are negligible differences between the predicted vapor generation with and without the structural deformation (Figure 66 and Figure 67).

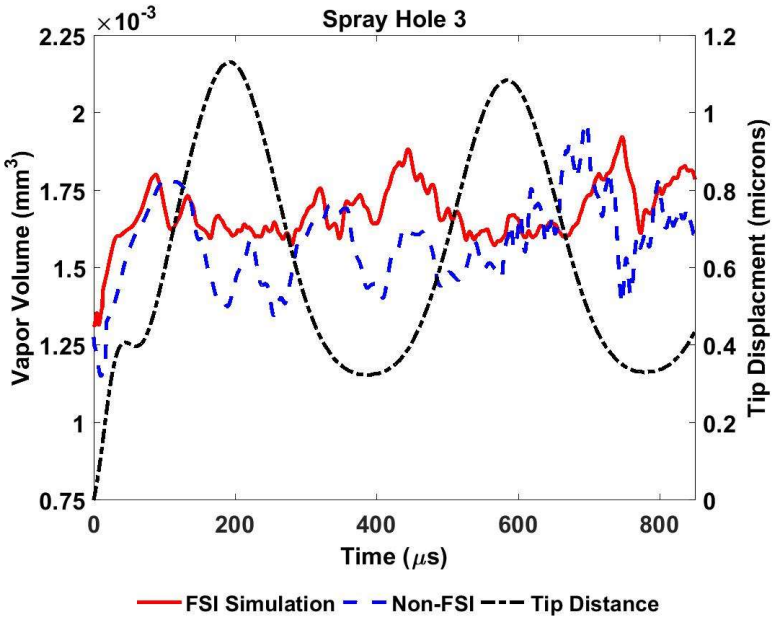

Figure 66. Vapor volume fraction for spray hole 3, which is perpendicular to the needle motion, with and without the needle motion.

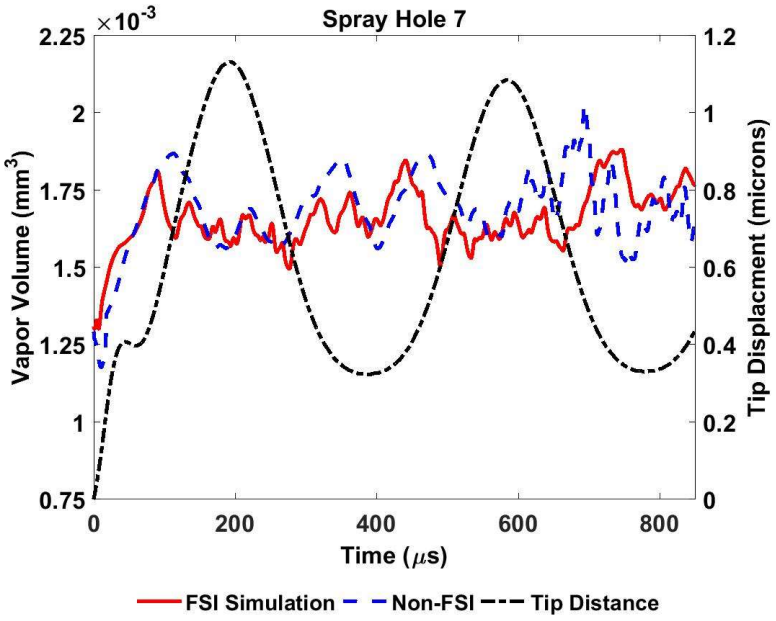

Figure 67. Vapor volume fraction for spray hole 7, which is perpendicular to the needle motion, with and without the needle motion.

The spray hole that is in the plane of the needle motion but which the needle moves away from also sees negligible changes in the vapor generation (Figure 68).

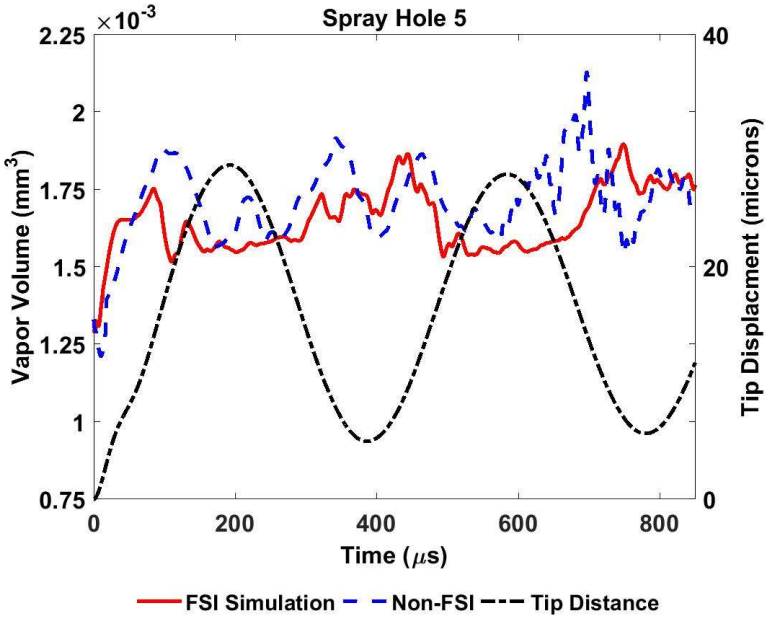

Figure 68. Vapor volume fraction for spray hole 5, which is in the plane of the needle motion, with and without the needle motion.

The only spray holes which are impacted by the needle motion are the ones that the needle deflects towards (Figure 69) which exhibits a decrease in the vapor generation.

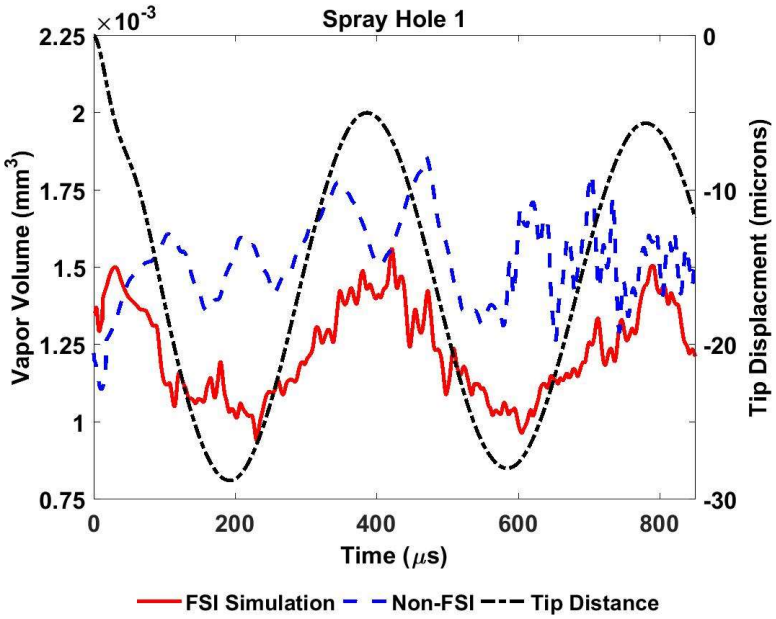

Figure 69. Vapor volume fraction for spray hole 1, which is in the plane of the needle motion, with and without the needle motion.

In the non-FSI simulation the vapor is generated when the flow separates as it turns into the spray hole (Figure 23). There is a similar amount of liquid flowing into the sac from both sides of the needle which then turns into the spray holes and in the center of the sac you generate a low-speed zone (Figure 70).

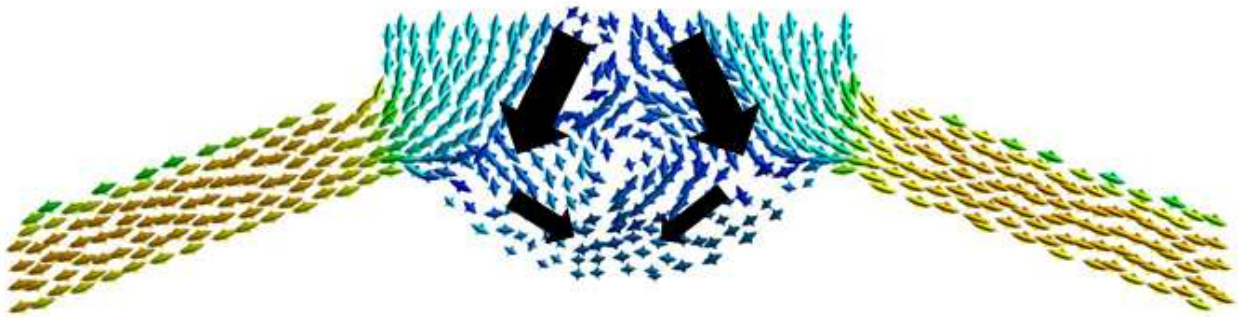

Figure 70. Sac flow without the structural displacement.

When the needle deflects to a single side there is an imbalance in the flow. There is a larger mass flow rate on the side that the needle is deflecting away from which creates a rotating core inside the sac (Figure 71).

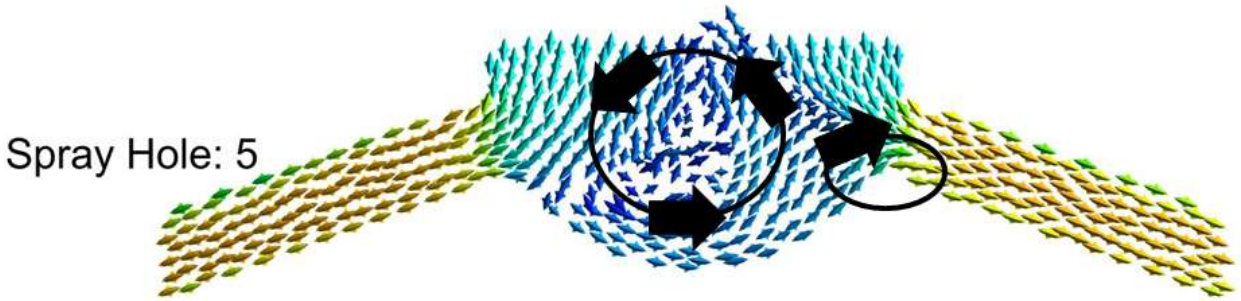

Figure 71. Sac flow with the needle bent away from spray hole 5.

When this occurs, the fluid will rotate along the bottom of the sac and enter the spray hole that the needle is bent towards with an upward trajectory. This suppresses the amount of separation along the top of the spray hole and reduces the amount of vapor formed (Figure 72). The flow along the bottom of the sac creates a separation along the bottom radius that will create additional vapor formation periodically.

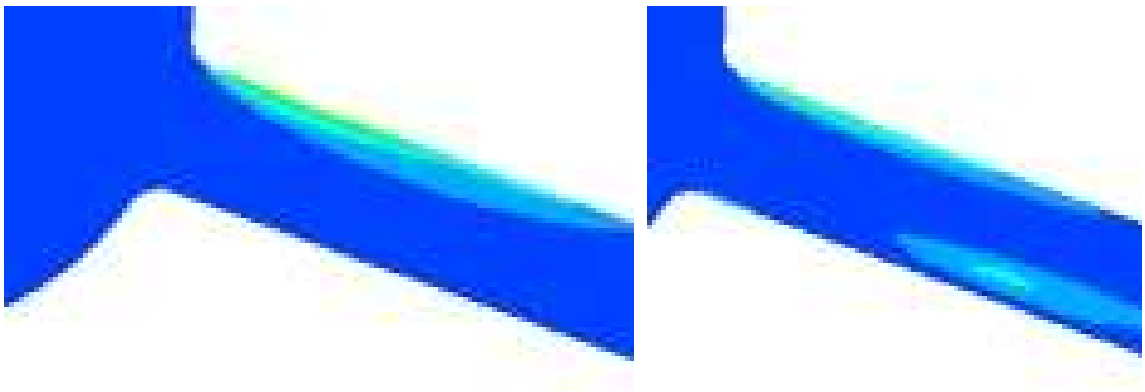

a) without structural displacement b) with structural displacement

Figure 72. Vapor volume fraction a) without structural displacements and b) with structural displacement. With the displacement the separation height is reduced decreasing the amount of vapor formed. The flow from the bottom of the sac into the spray hole creates additional vapor on the bottom of the spray hole.

X. FSI SIMULATION INCLUDING OPENING AND CLOSING NEEDLE MOTION

A. MOTION PROFILE

This section discusses the results of simulations of the injector where the entirety of the injection cycle is included. The rigid body vertical motion is a direct input from measured experimental data. The lift profile for this injector is shown in Figure 9. Figure 73 shows the needle position at low and high lift and illustrates how the gap between the seating surface and the needle changes over the lift profile

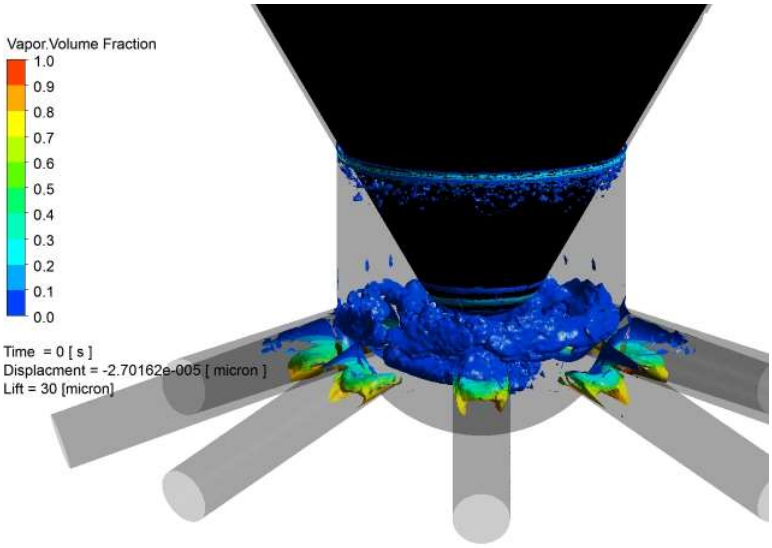

a) Low Lift

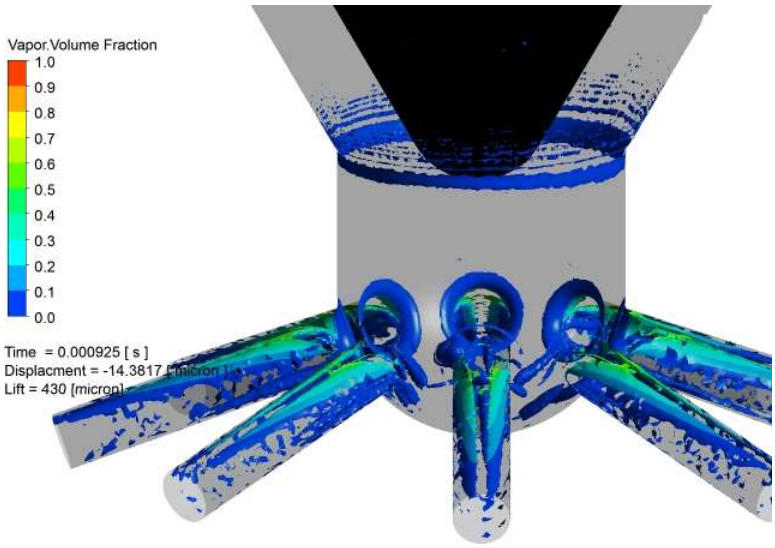

b) High Lift

Figure 73. Needle position at a) low lift and b) high lift

Figure 74 shows the extreme of the of the needle bending during the injection cycle and provides a reference for how the area can vary from side to side due to needle bending.

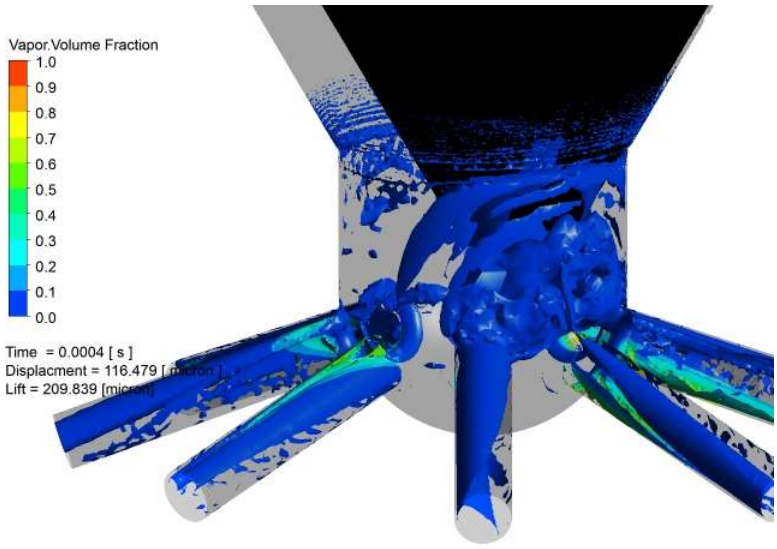

Figure 74. Extreme of lateral displacement from needle bending

For this study two simulations were run. For this study two cases were simulated. The case which this study is primarily interested in simulates how the needle bends due to

differences in the pressure around the needle. The second case simulated only allowed displacement in the vertical direction. The previous results in this thesis showed that the orientation of the gain orifice drove asymmetrical flow, having the two simulations allowed the asymmetrical flow that results from needle bending to be separated from the asymmetrical flow that results purely from the gain orifice orientation.

B. LATERAL MOTION

This section discusses the lateral motion of the needle and the forces that drive this motion. Figure 75 shows the vertical and lateral displacement measured at the needle tip over the injection cycle.

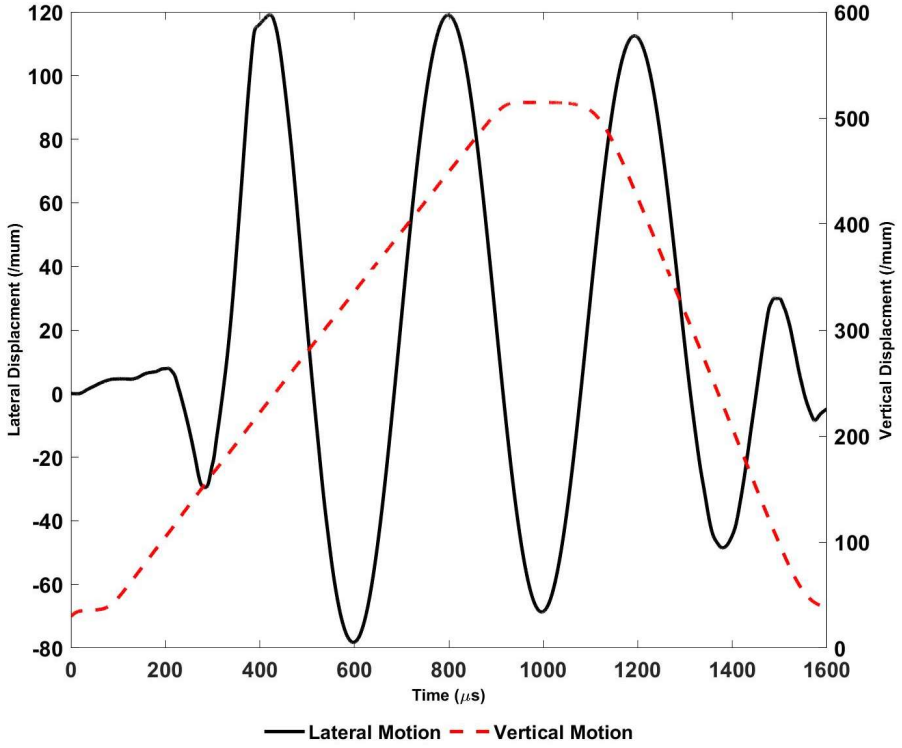

Figure 75. Vertical and lateral displacement of the needle tip during the injection cycle

At the start of the cycle the lateral motion is from the needle bending towards the seat (Figure 7) and then being pressed against this face from the fluid forces. For the initial approximate 200 microseconds the needle moves towards and along this seating face before reversing direction. After the reversal of the motion the needle hits the wall constraint at the 1st local minimum (t=~250 microseconds) and the following maximum (t=400 microseconds). Beyond this point time the needle freely oscillates until closing during which the needle's lateral motion is constrained by contact with the seating face at time =~1400 microseconds and ~1500microseconds.

The needle undergoes distinct two stages of motion. Initially the needle is displaced to one side and rides up along that side. This occurs in the initial 200 microseconds when the lift of the needle is less than approximately 150 microns. After that portion of the motion the needle reverses direction and then oscillates at the natural frequency of the needle

between the maximum deflection in the positive and negative direction. It's not a free oscillation because there is a magnitude difference in the deflection between the positive and negative direction, and as discussed in section 9 the difference in magnitude is due to the higher lateral force in the positive x direction. Figure 76 shows the force in the x direction on surfaces 1-6 as were defined in figures 14 and 55. These graphs isolate the force that drives the initial displacement as well as the force that creates the reversal and following oscillation of the needle. From the graphs the initial source is identified as the lateral force on the tip of the needle (surface 1). This is the only surface that has a force in the same direction as the initial displacement over the period during which the needle is pushed against the wall and not oscillating back and forth. The initial reversal occurs when the flow has been blocked off and a large force in the negative direction on surface three accelerates the needle in the opposite direction after which it oscillates between the extremes as shown in Figure 75.

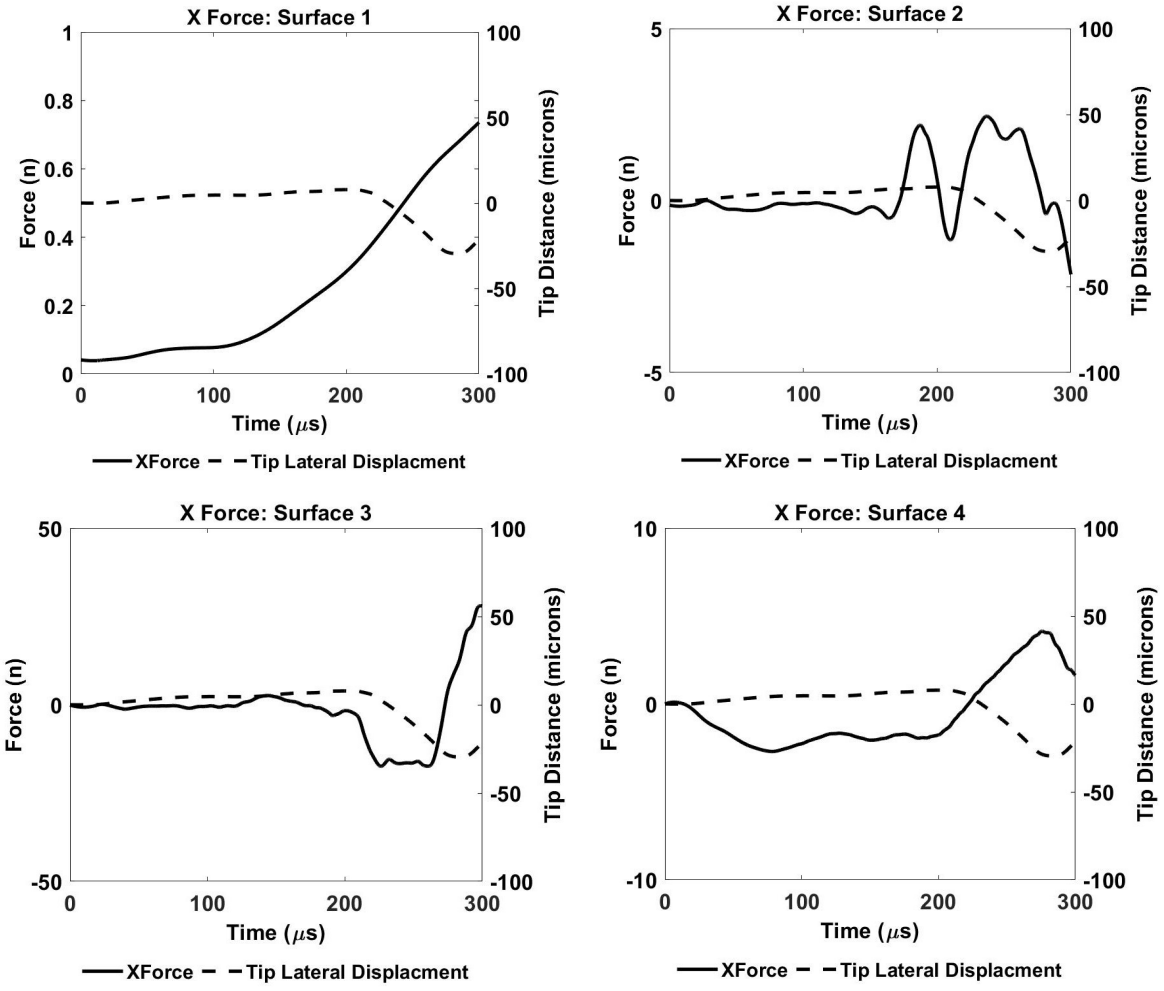

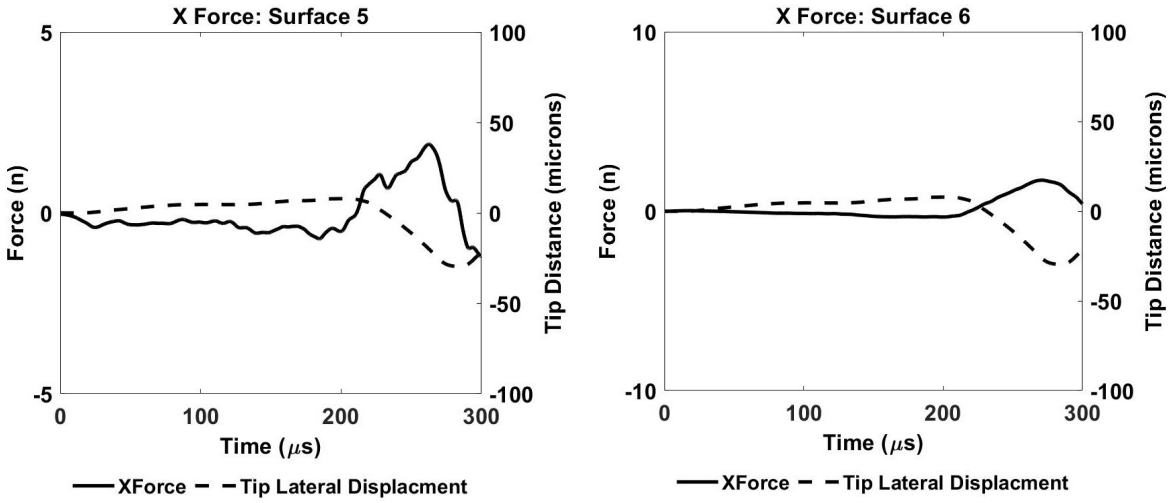

Figure 76. Force in the x direction and the tip Displacement during the initial portion of the injection cycle

As shown in Figure 76 the net force that drives this initial motion is only a few newtons, the coinciding pressure contour (Figure 77) does show a small asymmetrical pressure along the tip of the needle. The length of the needle allows this small force to generate a moment large enough to bend the needle. The only asymmetrical feature of the model is the gain orifice which points to that as being the feature that initially generates the motion of the needle.

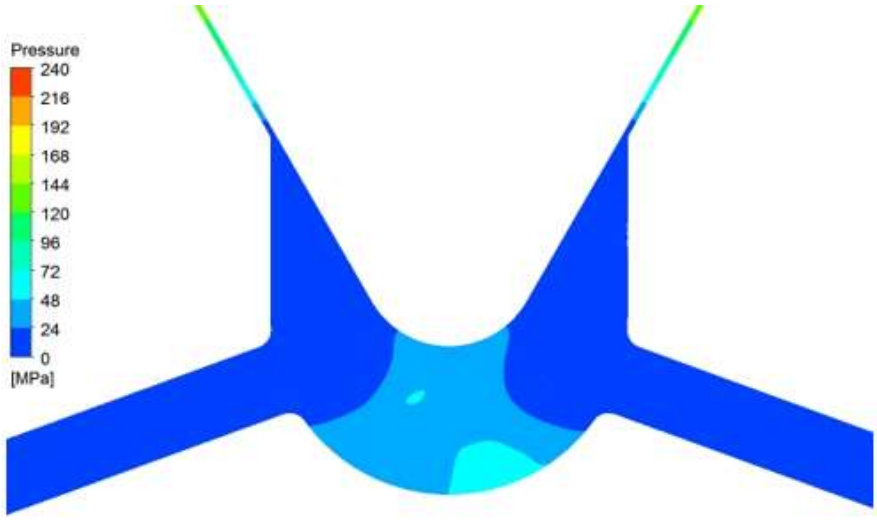

Figure 77. Pressure contour at the initial opening of the needle

The velocity contours at the initial do show an asymmetrical flow penetration into the sac (Figure 78) with higher velocity, and higher penetration on the side that the needle will move towards.

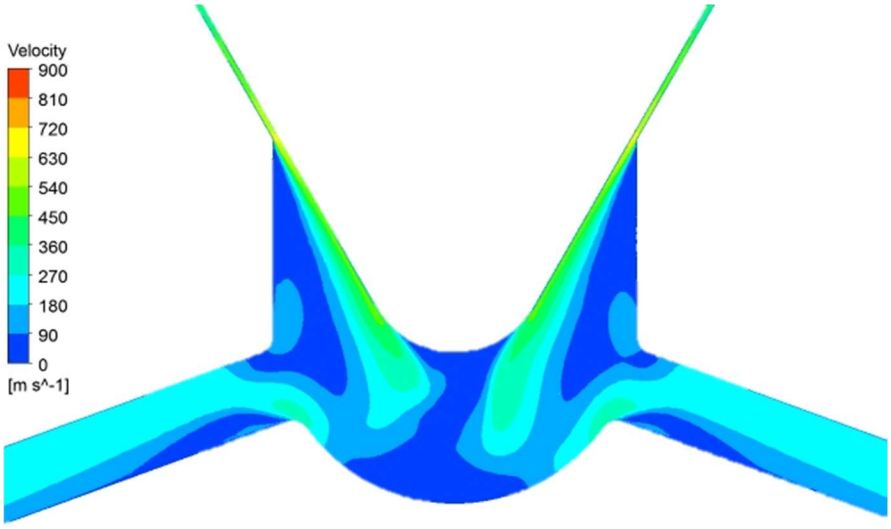

Figure 78. Velocity contour at the initial opening of the needle

There are two reversals of the motion that are driven by an outside force. These occur when the simulation time is approximately equal to 225 and 250 microseconds. At these points in time a high fluid pressure builds on the surface 3 and forces the needle to reverse direction. Figure 79 shows the pressure contour at this low lift high displacement condition. There is a higher pressure on the side that the needle is bent towards which creates the large force that will reverse the direction of the bending. Figure 80 shows the velocity contour at the midpoint of surface 3 at this same point in time and shows the root cause of this pressure difference. At low lifts when the needle is off center the flow is restricted on one side. The side-to-side area difference leads to high flow velocities on the side that the needle has moved away from and low velocities on the side with the smaller flow area. The difference in the flow velocities difference leads to the pressure differential that reverses the direction of the needle bending.

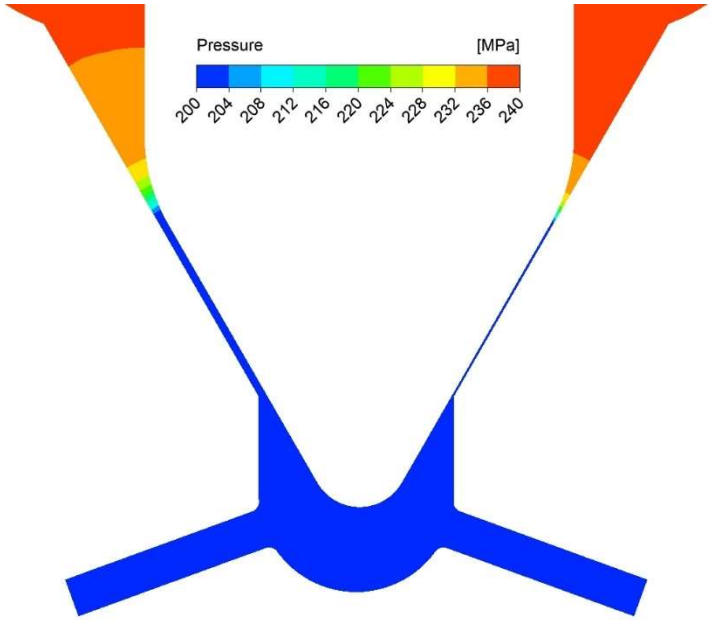

Figure 79. Pressure contour at a low lift when the needle is deflected to one side.

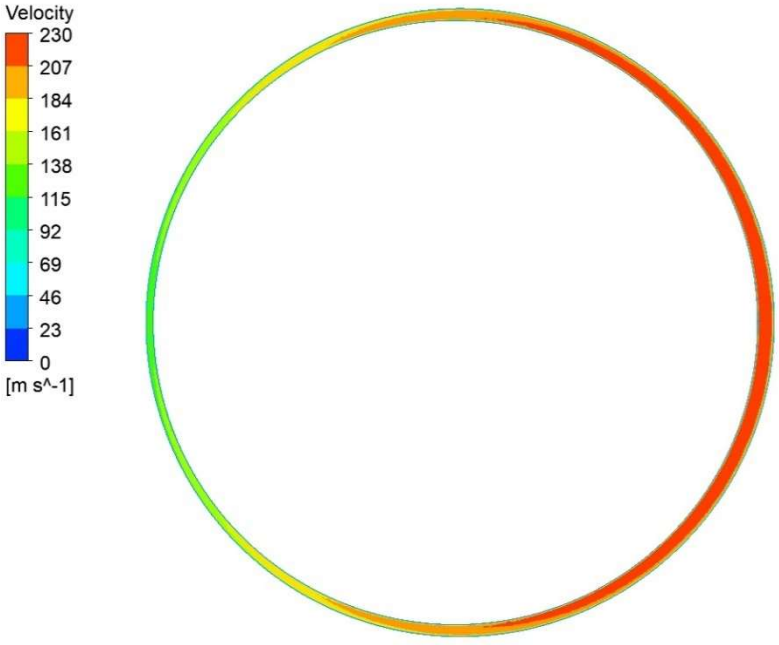

Figure 80. Velocity contour at the midpoint of surface 3 at a low lift when the needle is deflected to one side.

After ~450 microseconds the motion of the needle is no longer driven by external fluid forces because the velocity upstream of the sac is reduced as the flow restriction shifts from the cross-sectional area between the seat and the needle surface to the total cross-sectional area at the spray hole exits. The shift in the flow restriction can be seen in Figure 81 which plots the total mass flow rate versus the needle lift. The mass flow rate flattens after the needle lift exceeds ~220 microns. After this point even though cross-sectional area between the needle and the seat increases the mass flow rate does not change because the restriction is the cross-sectional area of the exits of the spray holes.

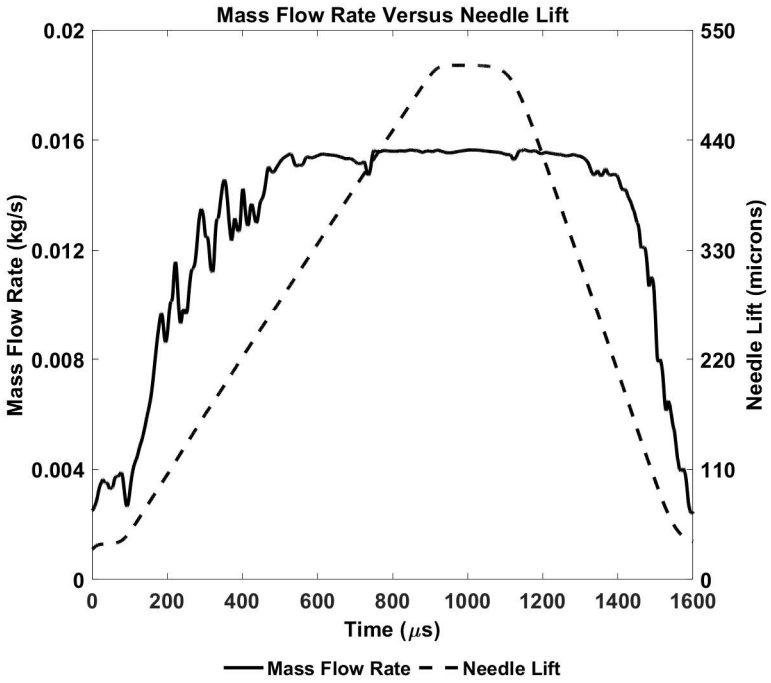

Figure 81. Mass flow rate versus needle lift.

Figure 82 shows the pressure contour at a high lift and high displacement condition. Even with the bias to one side there isn't a large pressure differential between the two sides of the needle. Because the flow restriction is at the spray hole rather than the cross-sectional area between the nozzle seat and needle surface the deflection of the needle doesn't generate a flow restriction.

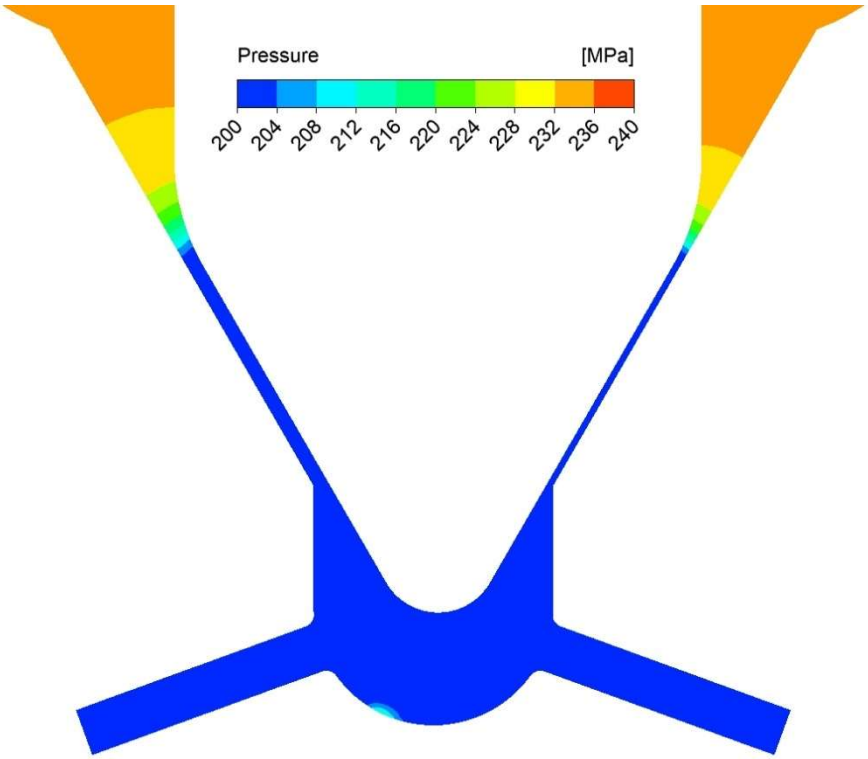

Figure 82. Pressure contour at a high lift when the needle is biased to one side.

Figure 83 shows the velocity through a plane at the midpoint of surface 3. Even though there is a bias towards one side, the velocities on each side are a similar magnitude. This leads to a similar pressure on both sides of the needle.

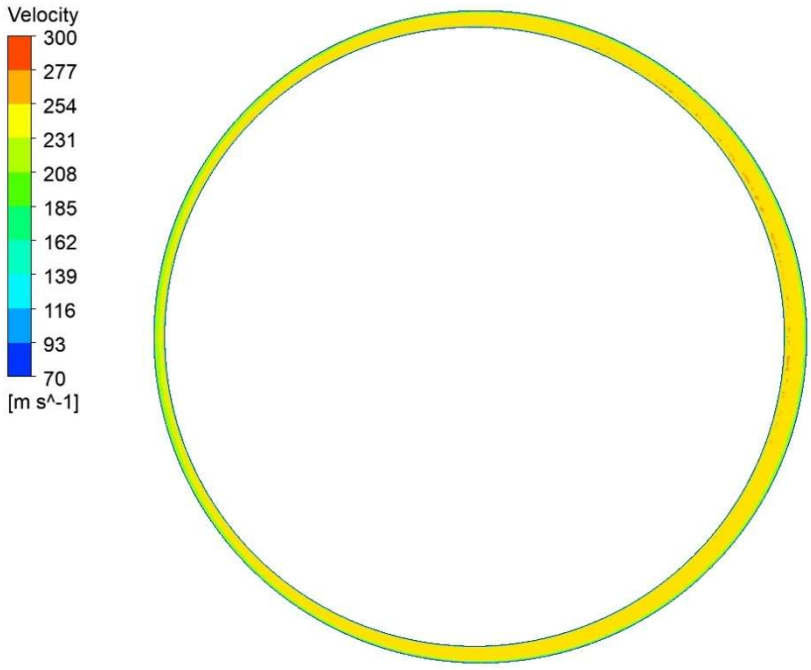

Figure 83. Velocity contour at the midpoint of surface 3 at a high lift when the needle is biased to one side.

After the transition of the location of the flow restriction the needle oscillates at it's natural frequency. The point that the needle oscillates about is offset from the origin because the hydraulic forces applied to the needle favor bending in the positive x direction, but these forces are not enough to further excite the motion and the magnitude of the oscillation (Figure 84) will decrease over the injection cycle until the closing portion where the seat constraints limit the magnitude of the motion.

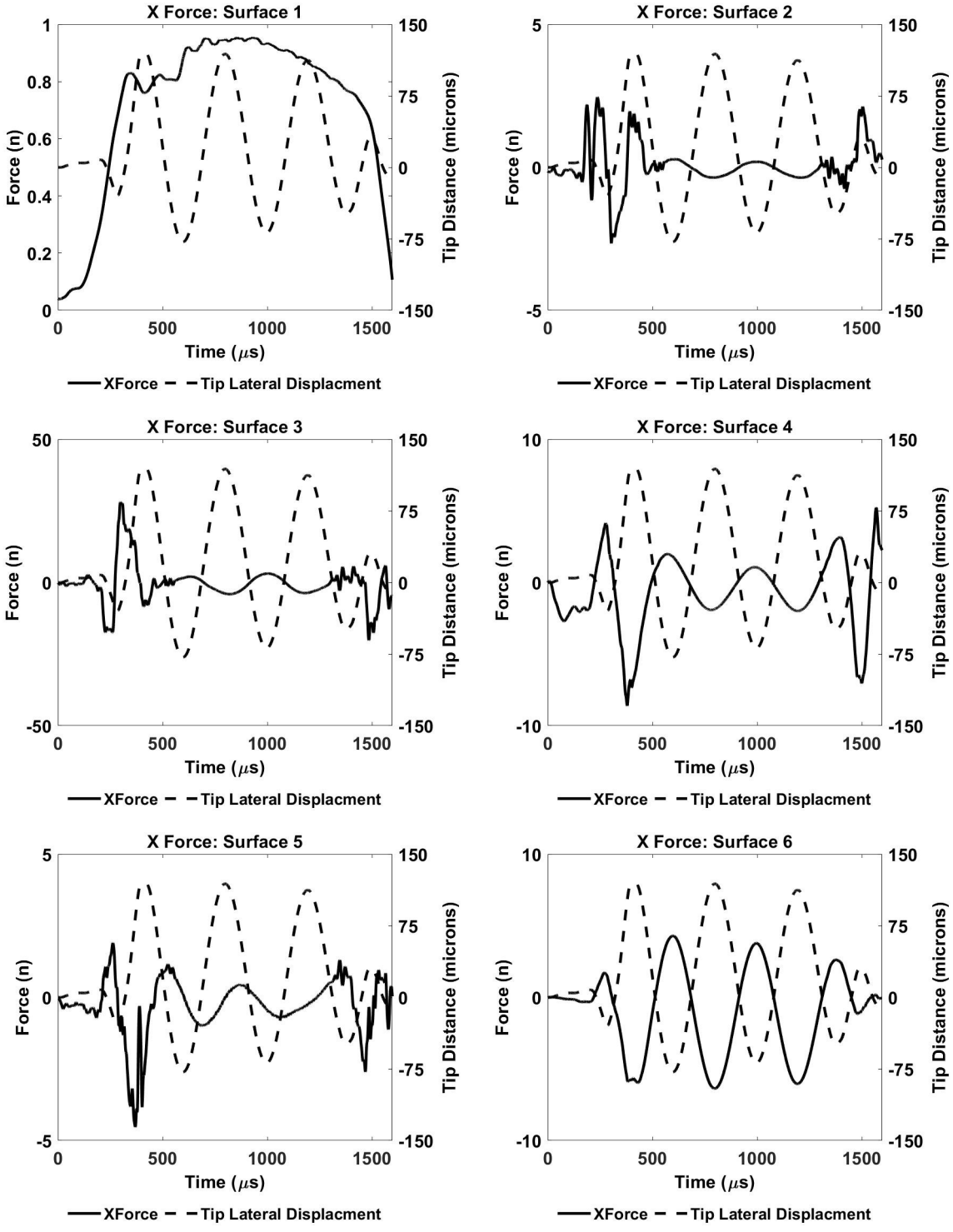

Figure 84. Forces on surfaces 1-6 over the entire injection cycle.

Figure 85 shows the forces on the bottom 3 surfaces with and without the lateral motion of the needle. At the start of the injection cycle the forces on these surfaces are nearly identical which indicates that the forces which initiate and drive the lateral motion

throughout the injection cycle are present because of the geometry and do not occur in response to an initial lateral displacement. The lateral motion instead limits the magnitude of the force in the x direction by decreasing pressure when the lateral bending increases the cross-sectional flow area. In the cases without lateral needle motion the only source of asymmetry in the model is the gain orifice which indicates that this is generating the motion.

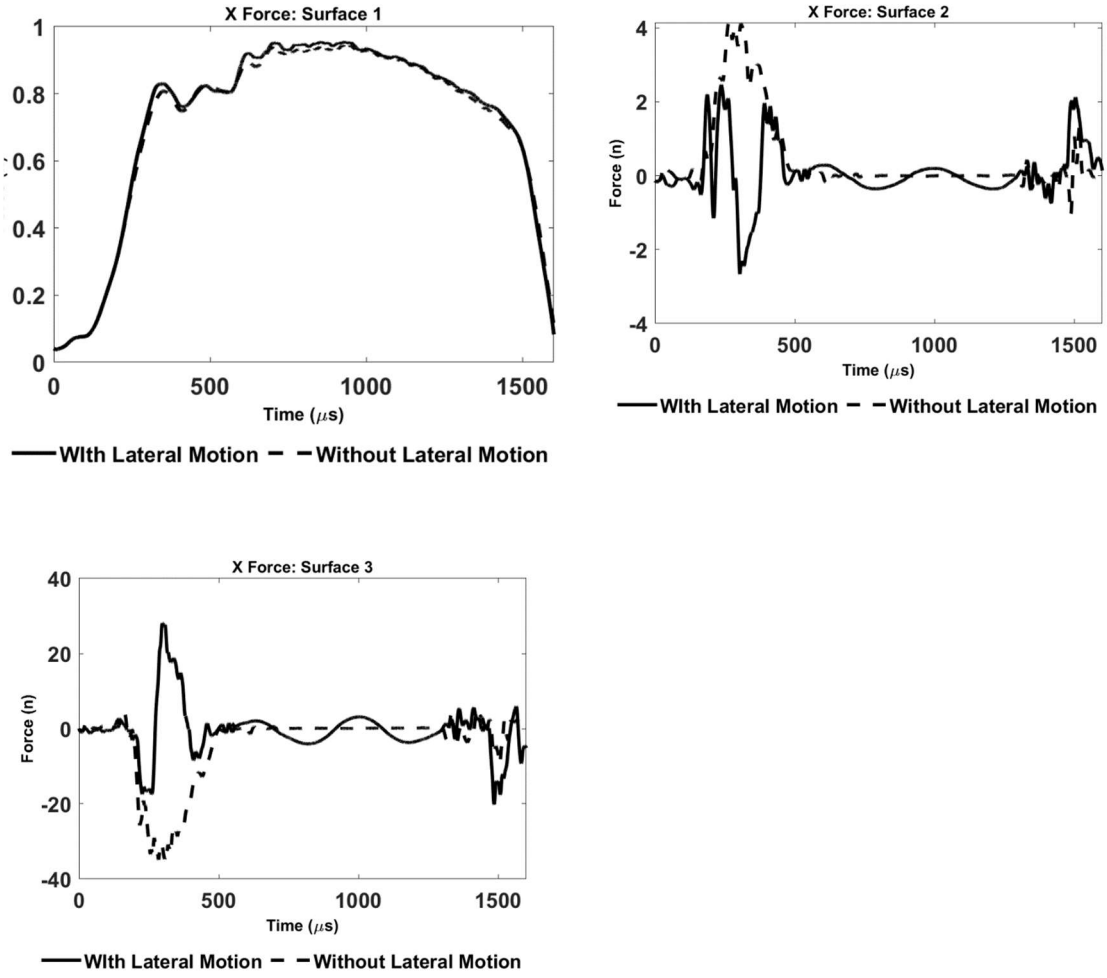

Figure 85. Forces on needle surfaces 1-3 with and without the lateral motion simulated.

C. MASS FLOW RATE

These previous section shows that asymmetries from gain orifice causes the needle to bend during the operation of the injector. This section looks at the impact of the motion on the quantity fuel injected during operation. Specifically, it looks at how the bending affects the both the overall nozzle mass flow rates and the mass flow rates through the individual spray holes. Figure 86 shows the total mass flow rate for the nozzle over the entire injection cycle and Figure 87 shows the percentage change to the mass flow rate when the lateral motion is included. The percentage change is calculated by taking the difference between the mass flow rate with and without the lateral motion simulated and normalizing by the mass flow rate from the simulation without the lateral motion as shown in equation 85.

$$100 \times \frac{\left(MassFlow_{LateralMotion} - MassFlow_{NoLateralMotion}\right)}{MassFlow_{NoLateralMotion}} \tag{85}$$

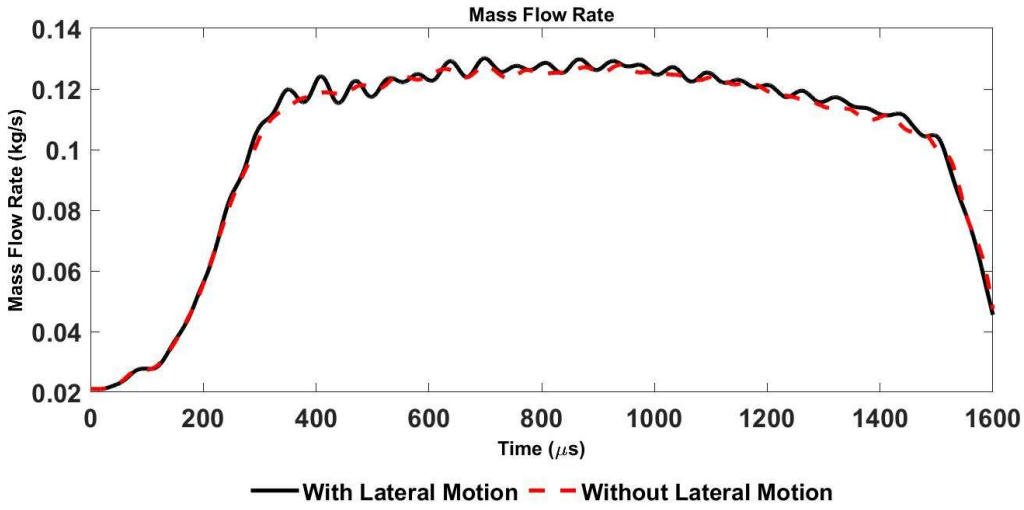

Figure 86. Total Mass flow rate with and with the lateral motion

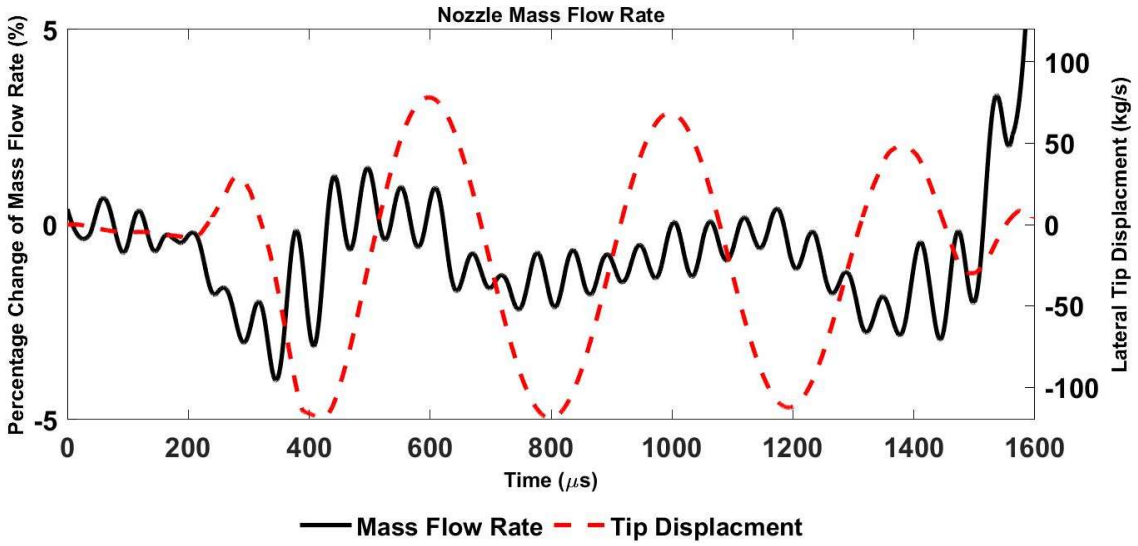

Figure 87. Percentage change of the mass flow rate when the lateral motion is simulated

Figure 86 and Figure 87 show that the change in the total mass flow rate is minimal and that the largest changes occur when the needle is opening or closing. Other than at the end of the simulation the largest change that occurs is less than 5%. There is an overall increase in the mass of fuel injected when the when the needle is allowed to bend from 166.5 mg to 167.9 mg however this is less than a 1% increase.

Figure 88 shows the mass flow rates through the individual spray holes for the simulations with and without the lateral motion. There can be a large difference between the mass flow rates of individual spray holes even without lateral motion. The addition of the lateral motion does add more variation over small time scales to mass flow rate and when comparing the instantaneous mass flow rate between the simulations with and without lateral motion there can be significant differences.

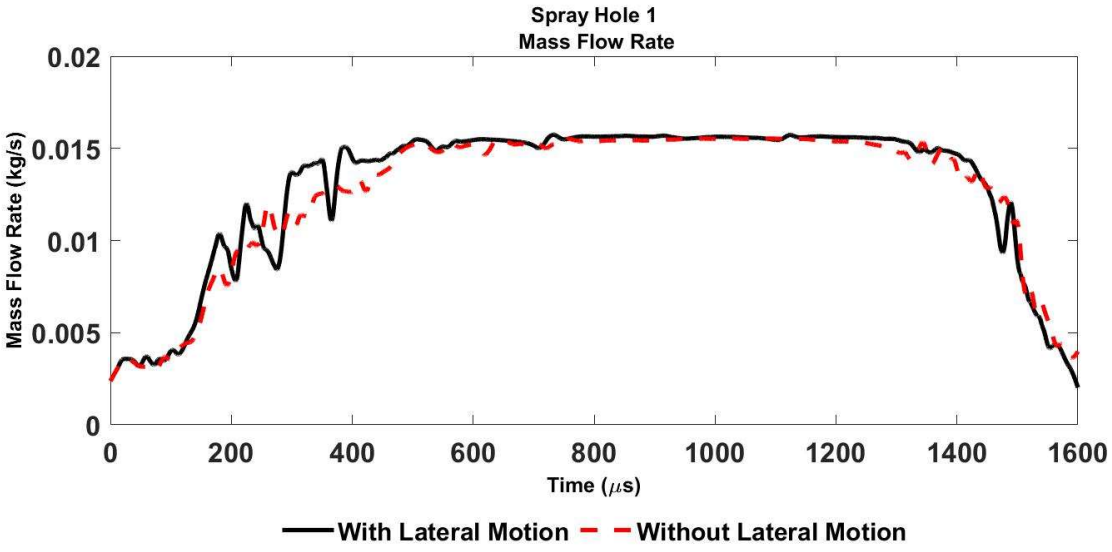
Spray Hole 1
Mass Flow Rate
Mass Flow Rate (kg/s)
0.02
0.015
0.01
0.005
0
0
200
400
600
800
1000
1200
1400
1600
Time (μs)
With Lateral Motion
Without Lateral Motion

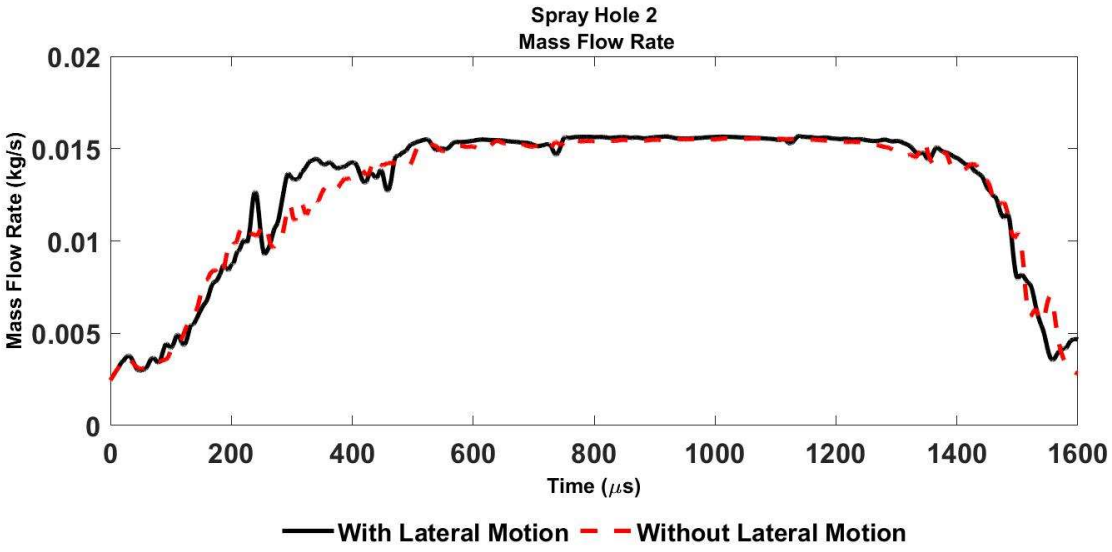
Spray Hole 2
Mass Flow Rate
Mass Flow Rate (kg/s)
0.02
0.015
0.01
0.005
0
0
200
400
600
800
1000
1200
1400
1600
Time (μs)
With Lateral Motion
Without Lateral Motion

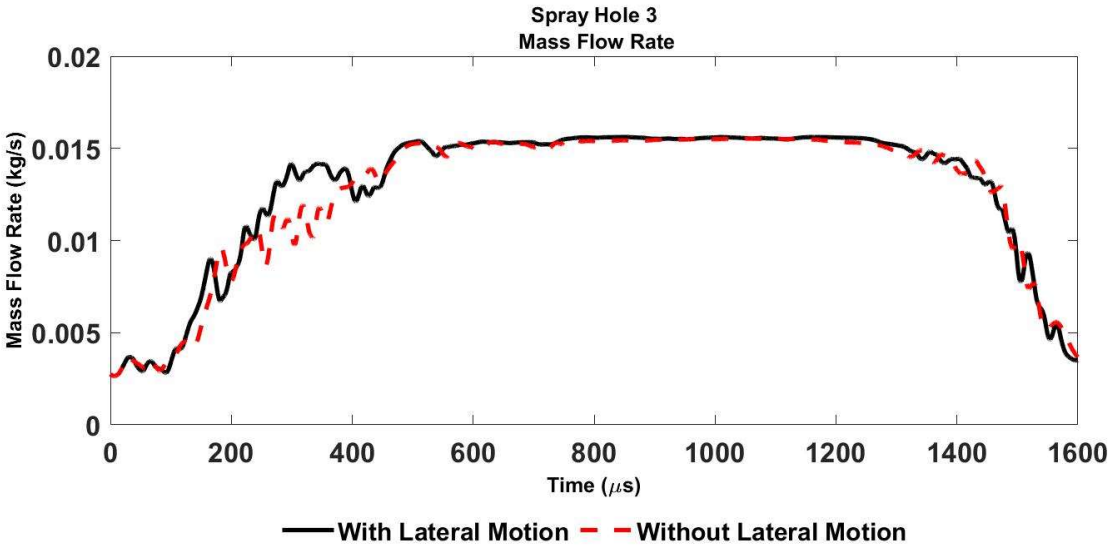
Spray Hole 3
Mass Flow Rate
Mass Flow Rate (kg/s)
0.02
0.015
0.01
0.005
0
0
200
400
600
800
1000
1200
1400
1600
Time (μs)
With Lateral Motion
Without Lateral Motion

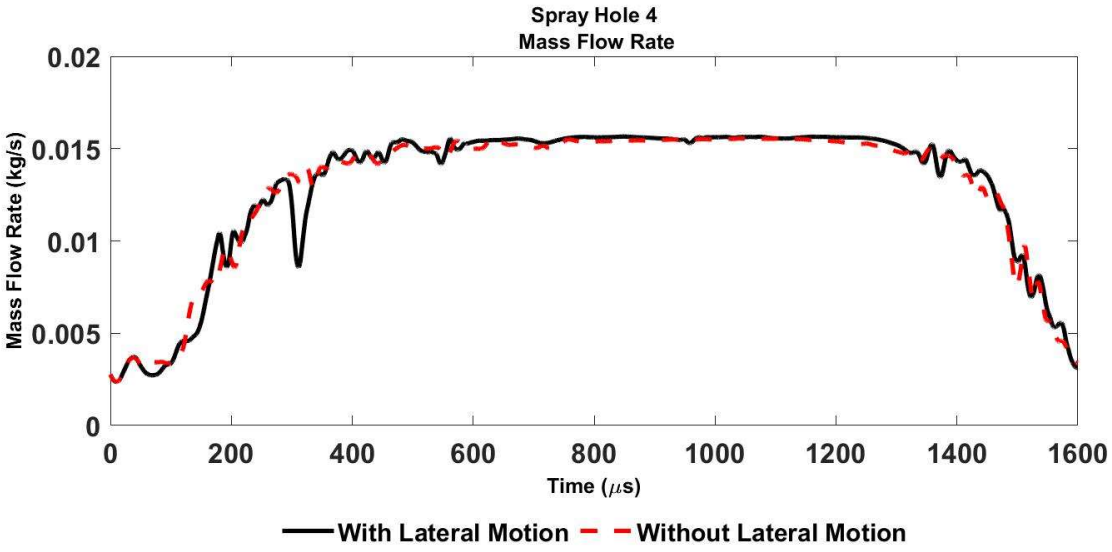
Spray Hole 4
Mass Flow Rate
Mass Flow Rate (kg/s)
0.02
0.015
0.01
0.005
0
0
200
400
600
800
1000
1200
1400
1600
Time (μs)
With Lateral Motion
Without Lateral Motion

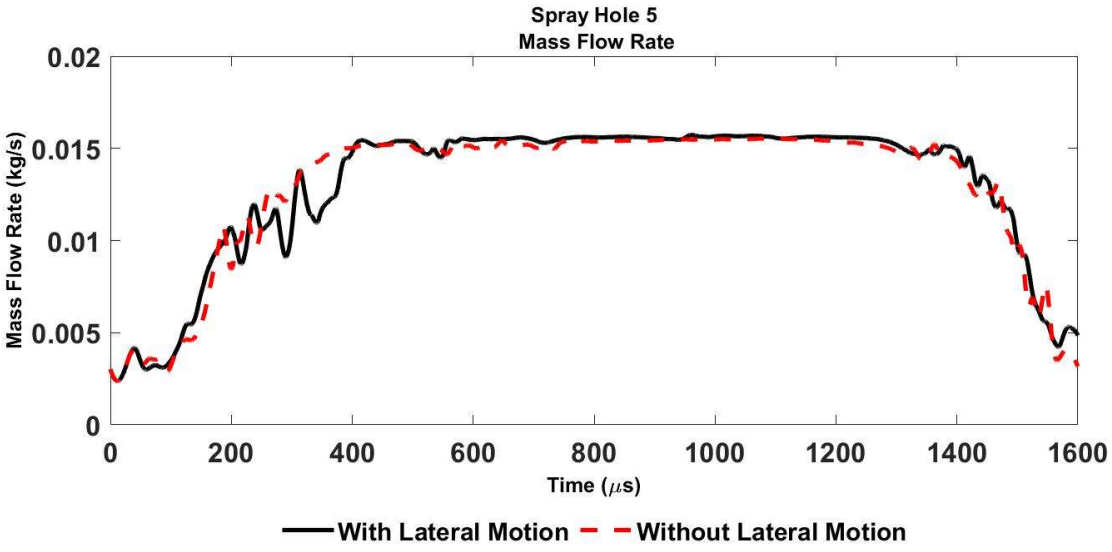
Spray Hole 5
Mass Flow Rate
Mass Flow Rate (kg/s)
0.02
0.015
0.01
0.005
0
0
200
400
600
800
1000
1200
1400
1600
Time (μs)
With Lateral Motion
Without Lateral Motion

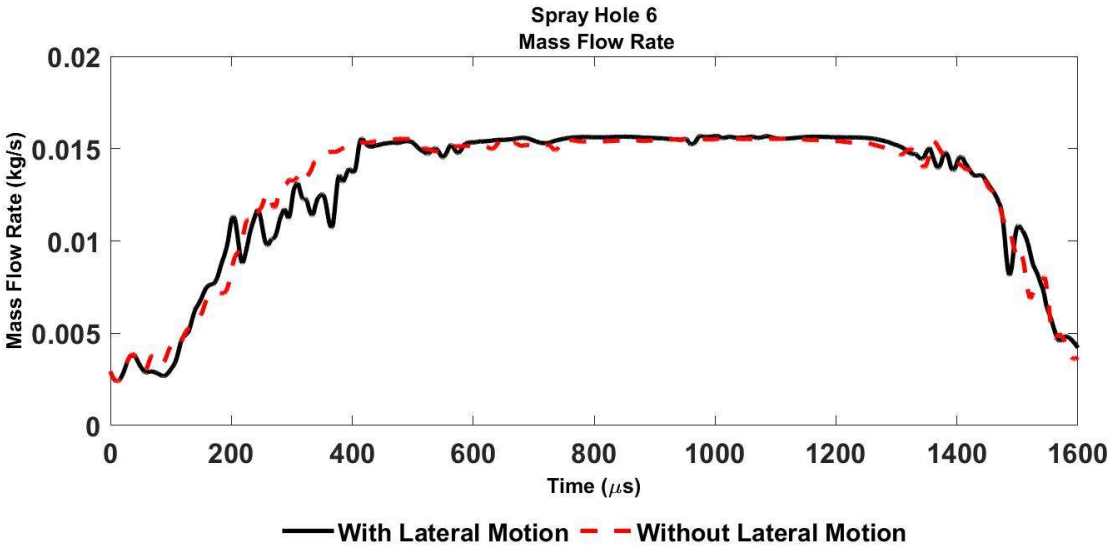
Spray Hole 6
Mass Flow Rate
Mass Flow Rate (kg/s)
0.02
0.015
0.01
0.005
0
0
200
400
600
800
1000
1200
1400
1600
Time (μs)
With Lateral Motion
Without Lateral Motion

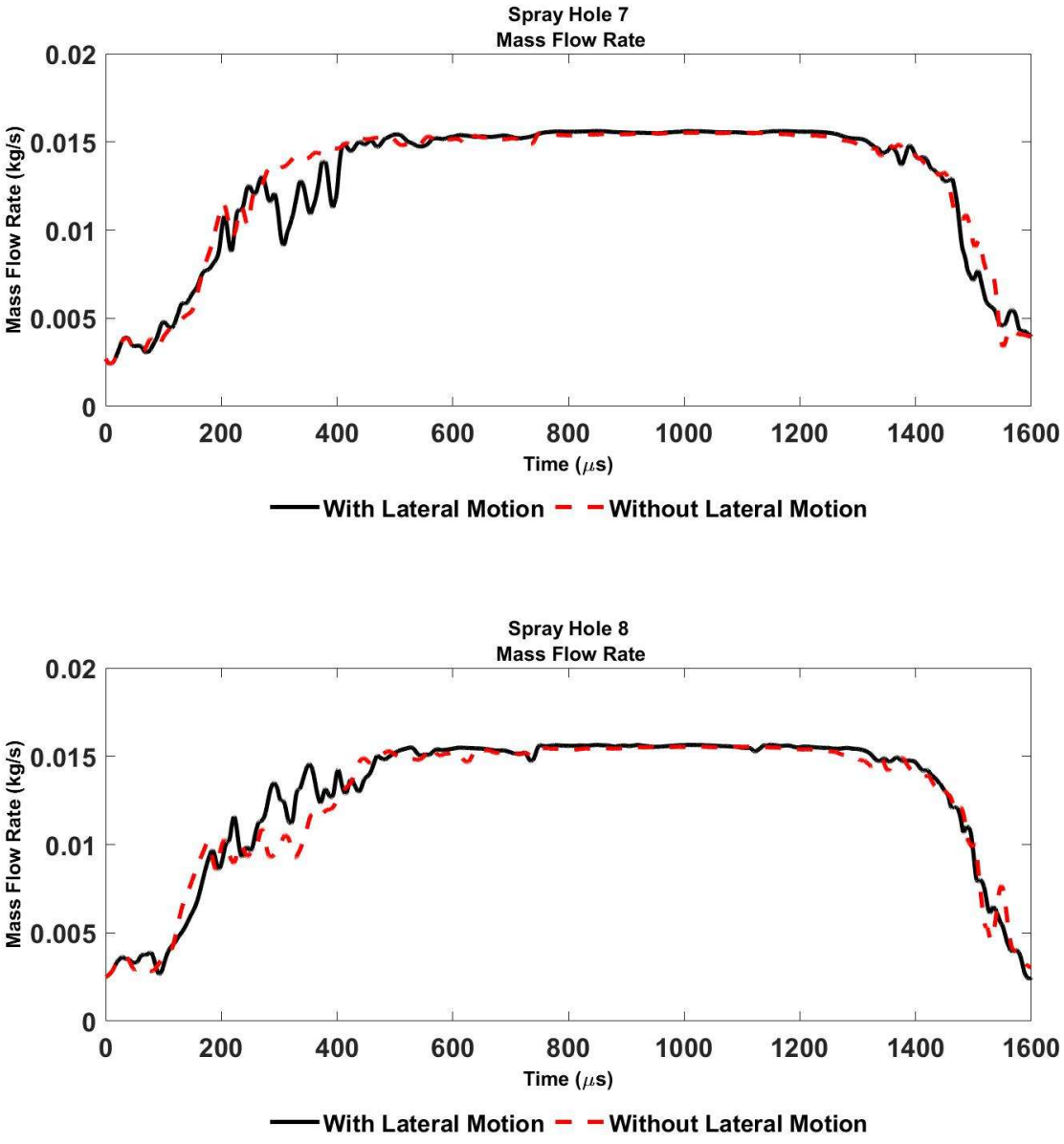

Figure 88. Individual spray hole mass flow rates with and without lateral motion

These simulations show that the lateral motion impacts the mass flow rates and this portion of the research tries to quantify if that impact is beneficial or detrimental. To quantify this the following equation is introduced where mass flow rate for the individual spray hole is divided by the mass flow rate for the nozzle. This gives the percentage of the total flow going through an individual spray hole. In an ideal 8-hole injector the flow through each hole should be 12.5% of the total flow. Equation 86 gives the deviation of the flow from the ideal.

$$100 \times \frac{MassFlowRate_{sprayhole}}{MassFlowRate_{Nozzle}} - 12.5 \quad (86)$$

Figure 89 plots the deviation of the flow from the ideal for the simulations with and without lateral motion. These plots show that in general most of the asymmetrical flow for individual spray holes occur at the lower lifts. These portions align with the portions of the injection curve (Figure 86) where the mass flow rate is increasing or decreasing and that physically represent portions where the flow is restricted by the cross-sectional area of the gap between the seat and the needle rather than the cross-sectional exit area of the spray holes.

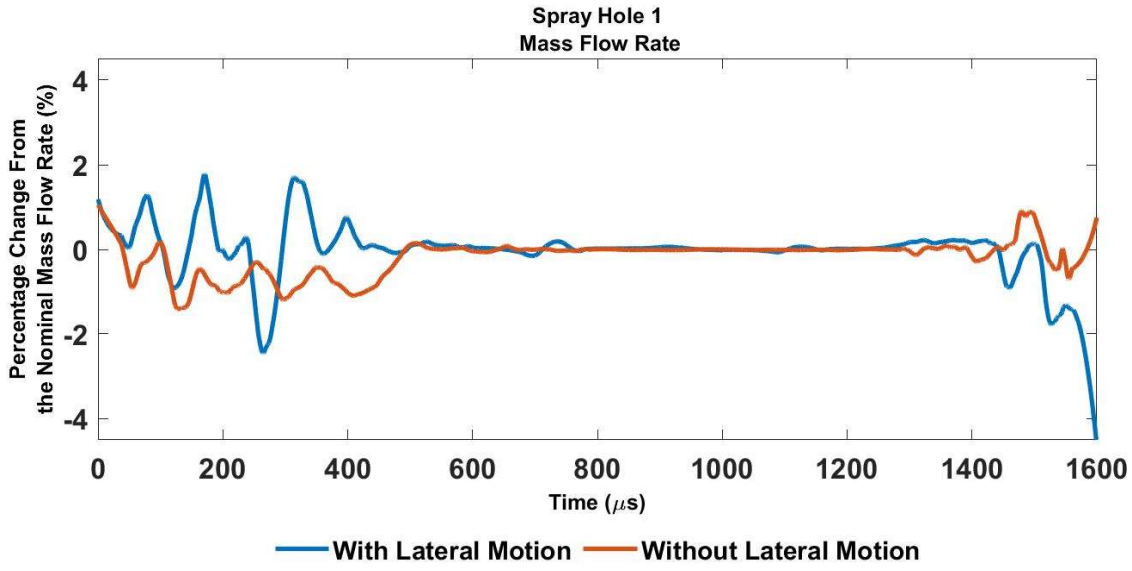

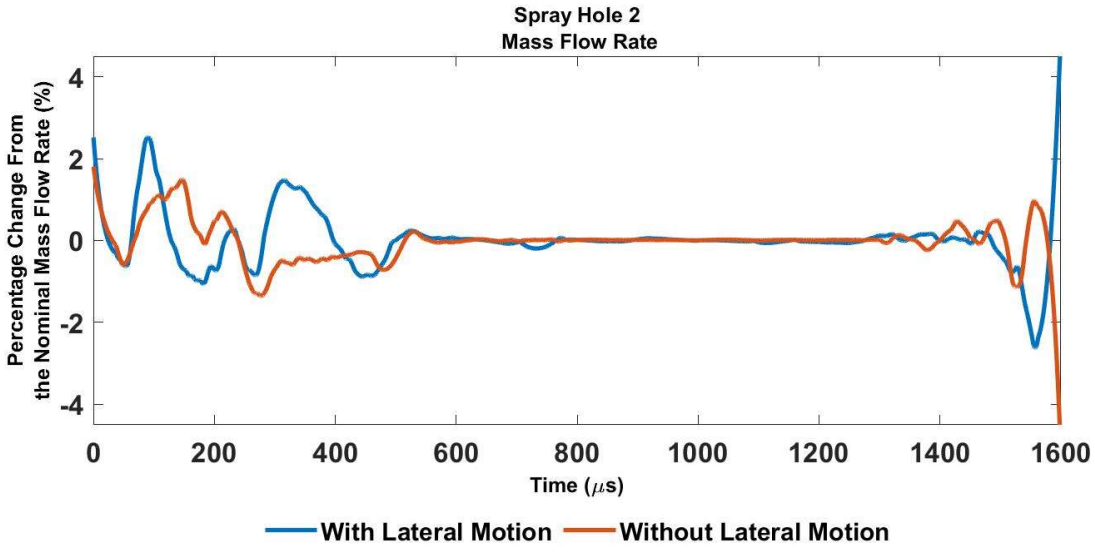
Spray Hole 2
Mass Flow Rate
Percentage Change From
the Nominal Mass Flow Rate (%)
4
2
0
-2
-4
0
200
400
600
800
1000
1200
1400
1600
Time (μs)
With Lateral Motion
Without Lateral Motion

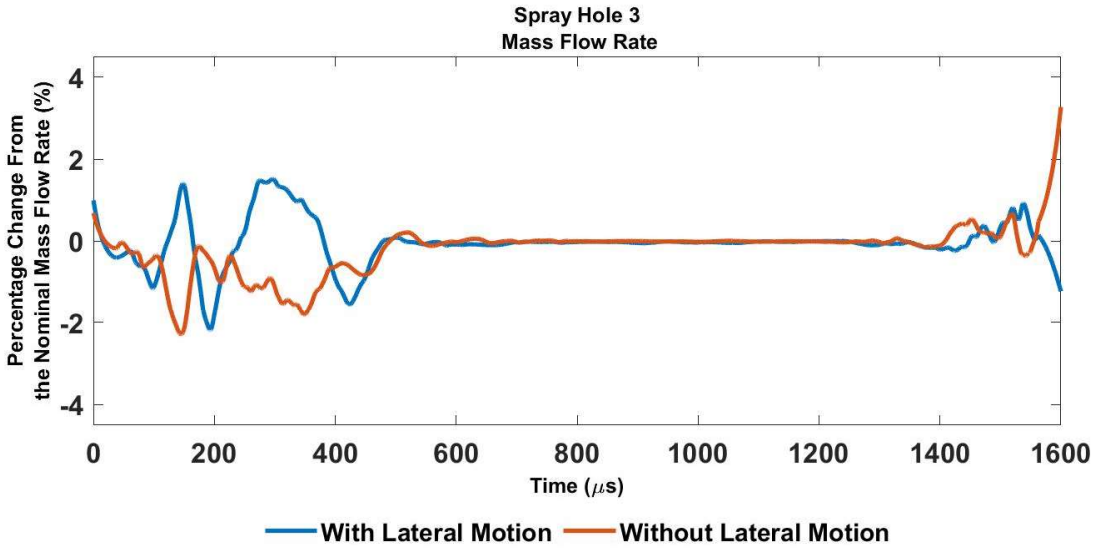
Spray Hole 3
Mass Flow Rate
Percentage Change From
the Nominal Mass Flow Rate (%)
4
2
0
-2
-4
0
200
400
600
800
1000
1200
1400
1600
Time (μs)
With Lateral Motion
Without Lateral Motion

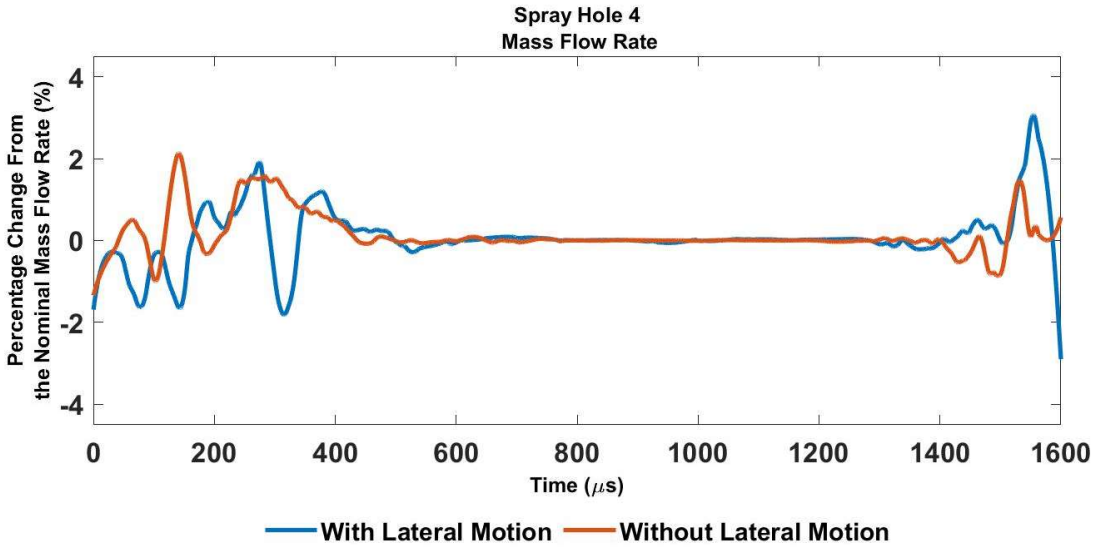
Spray Hole 4
Mass Flow Rate
Percentage Change From
the Nominal Mass Flow Rate (%)
4
2
0
-2
-4
0
200
400
600
800
1000
1200
1400
1600
Time (μs)
With Lateral Motion
Without Lateral Motion

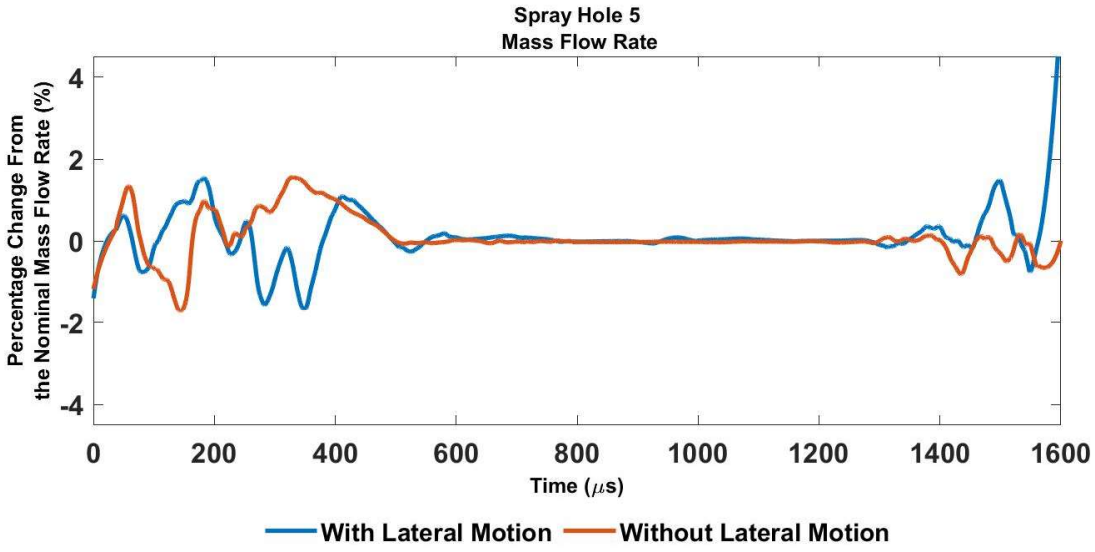
Spray Hole 5
Mass Flow Rate
Percentage Change From
the Nominal Mass Flow Rate (%)
4
2
0
-2
-4
0
200
400
600
800
1000
1200
1400
1600
Time (μs)
With Lateral Motion
Without Lateral Motion

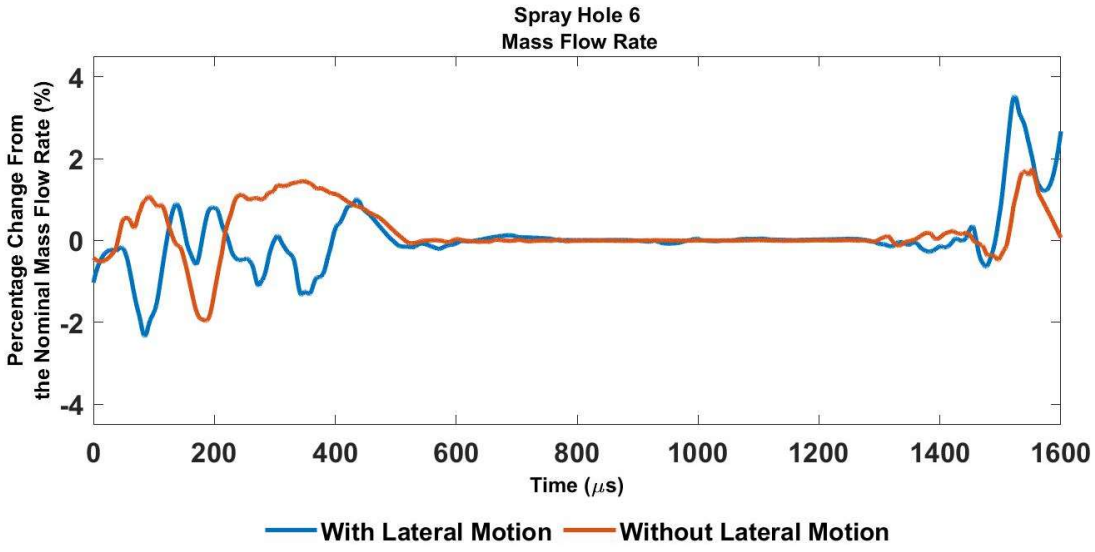
Spray Hole 6
Mass Flow Rate
Percentage Change From the Nominal Mass Flow Rate (%)
4
2
0
-2
-4
0
200
400
600
800
1000
1200
1400
1600
Time (μs)
With Lateral Motion
Without Lateral Motion

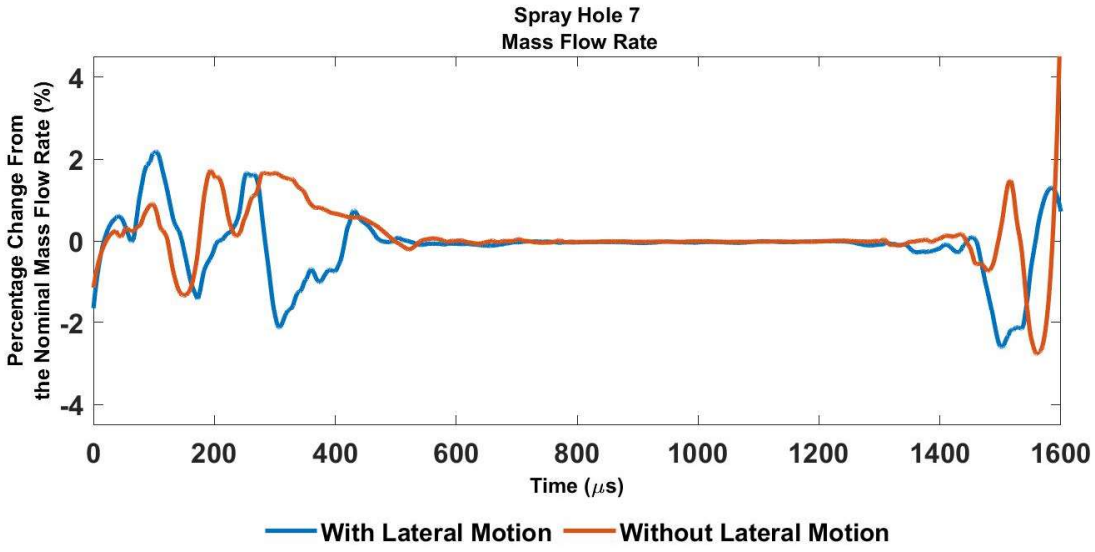
Spray Hole 7
Mass Flow Rate
Percentage Change From the Nominal Mass Flow Rate (%)
4
2
0
-2
-4
0
200
400
600
800
1000
1200
1400
1600
Time (μs)
With Lateral Motion
Without Lateral Motion

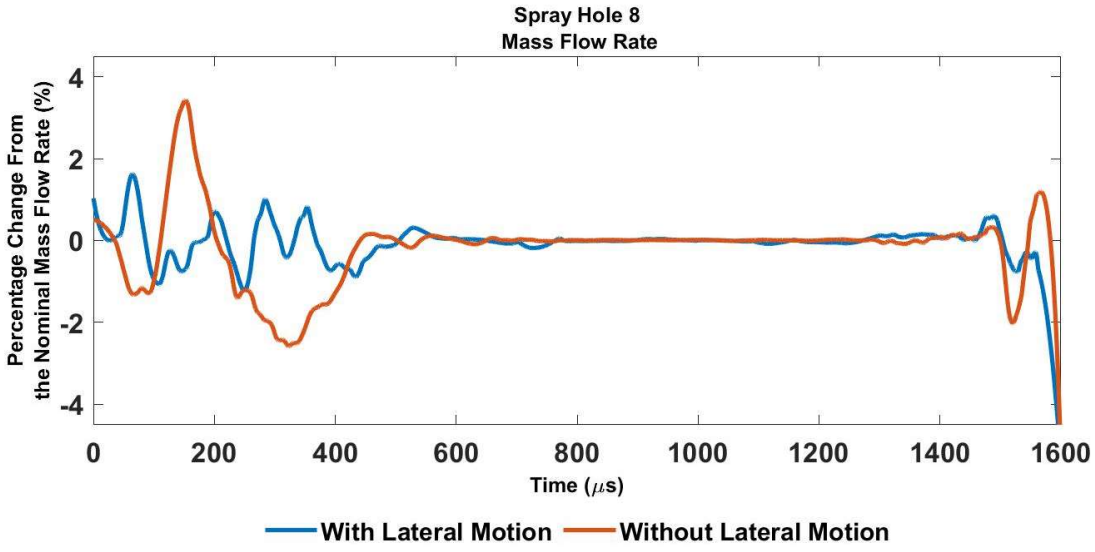

Figure 89. Percentage of excess mass flow rate for individual spray holes.

During the opening portion (before 600 microseconds) the lateral motion of the needle is beneficial. For most of the spray holes the magnitude of the deviation is similar with and without the lateral motion and less than ~2% (which is a ~16% increase from the ideal 12.5%). The exception is spray hole 8 where the deviation peaks at ~3.7 % (this represents a ~30% increase from the ideal 12.5%). Additionally, the lateral motion forces the injected mass flow rate to oscillate about the ideal of 0%. In simulations without the lateral motion the mass flow rate will tend to remain above or below the ideal level. This indicates that although some spray hole to spray hole mass flow rate discrepancies will always remain during opening the motion can help limit that. This will lead a more symmetrical combustion and cylinder temperature and should promote better fuel efficiency.

During the portion where the mass flow rate remains constant (from ~600 microseconds to ~1450 microseconds) there is slightly more variation in the simulation with the lateral motion than without but it is of a negligible scale.

During the closing portion (after ~1450 microseconds) the lateral motion doesn't provide a quantifiable benefit or detriment. To determine if it is harmful or helpful a combustion simulation would need to be run and that is beyond the scope of this study.

D. VAPOR VOLUME

This section looks at the impact of the lateral motion of the needle on the vapor formation in the individual spray holes. For this portion of the study a new measurement is introduced to quantify the change in the distance of the needle tip from the individual spray holes. This measurement is how much the distance between the center of the spray hole entrance and the needle tip is changing in the XZ plane. This measurement is shown in Figure 90. At time t=0s the tip is centered and the base tip distance is assumed to be zero, negative values indicate that the tip is getting close to a spray hole and positive values indicate that the distance is increasing.

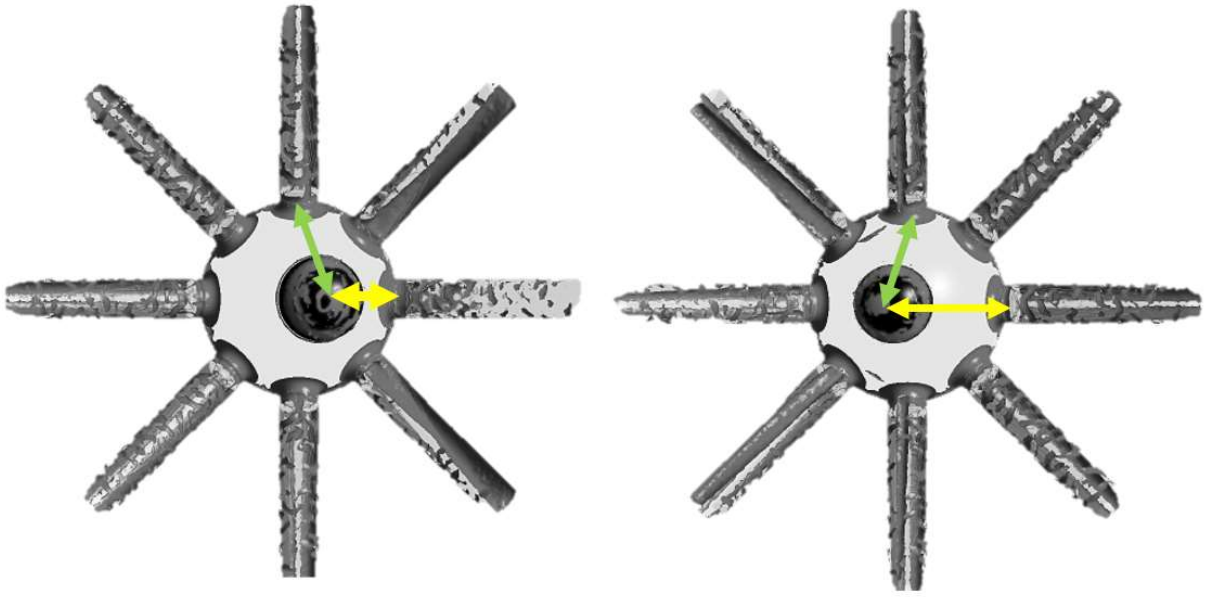

Figure 90. Tip distance measurement at two different time steps

Figure 91 shows the vapor volume in cubic millimeters with and without the lateral motion. The trend for both cases follows what was discussed in section 7 where there is more vapor at the low lifts and the amount of vapor will decrease at the higher lifts.

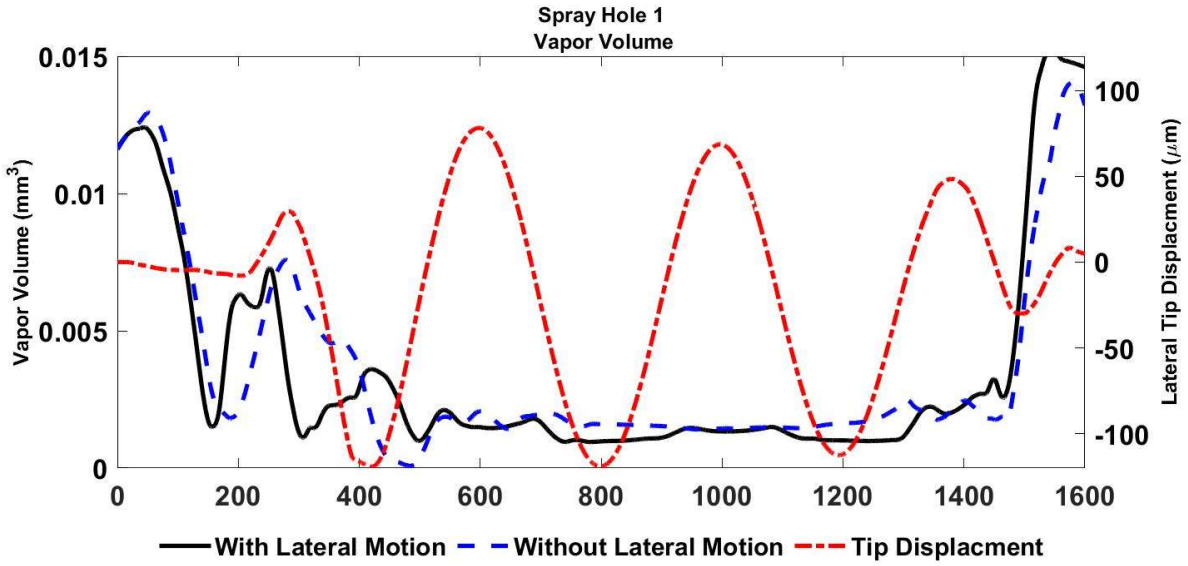
Spray Hole 1
Vapor Volume
Vapor Volume (mm3)
Lateral Tip Displacment (μm)
0.015
0.01
0.005
0
100
50
0
-50
-100
0
200
400
600
800
1000
1200
1400
1600
With Lateral Motion
Without Lateral Motion
Tip Displacment

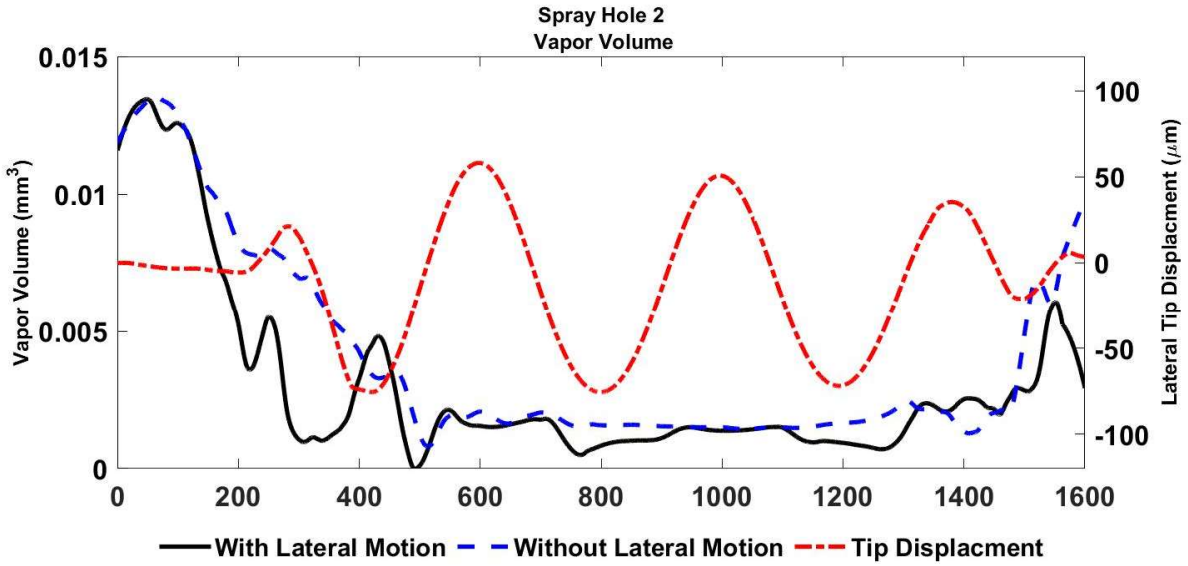
Spray Hole 2
Vapor Volume
Vapor Volume (mm3)
Lateral Tip Displacment (μm)
0.015
0.01
0.005
0
100
50
0
-50
-100
0
200
400
600
800
1000
1200
1400
1600
With Lateral Motion
Without Lateral Motion
Tip Displacment

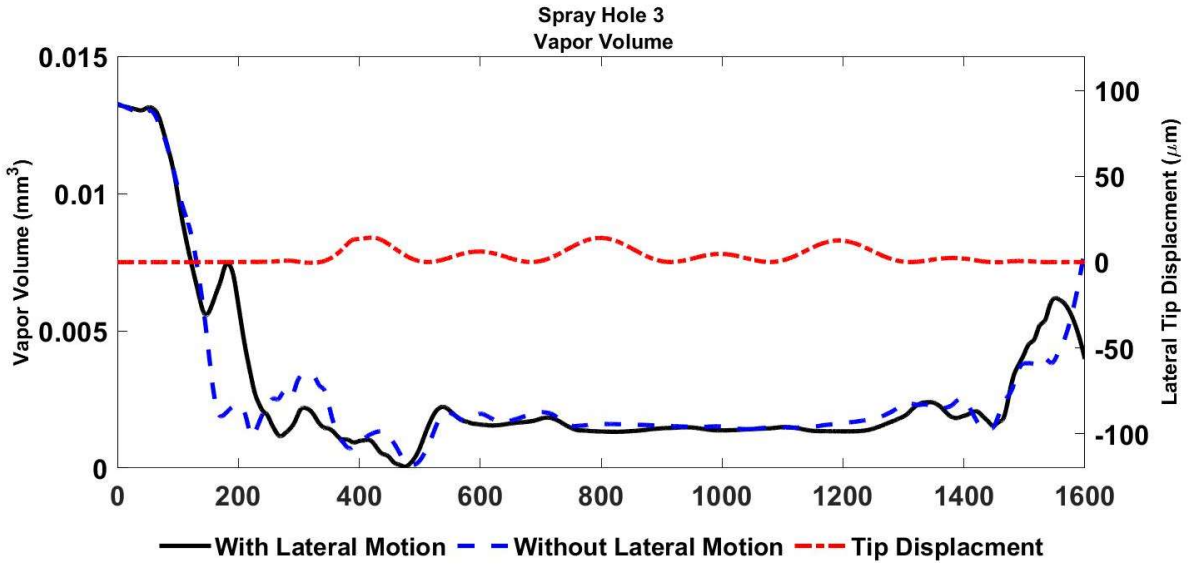
Spray Hole 3
Vapor Volume
Vapor Volume (mm3)
Lateral Tip Displacment (μm)
0.015
0.01
0.005
0
100
50
0
-50
-100
0
200
400
600
800
1000
1200
1400
1600
With Lateral Motion
Without Lateral Motion
Tip Displacment

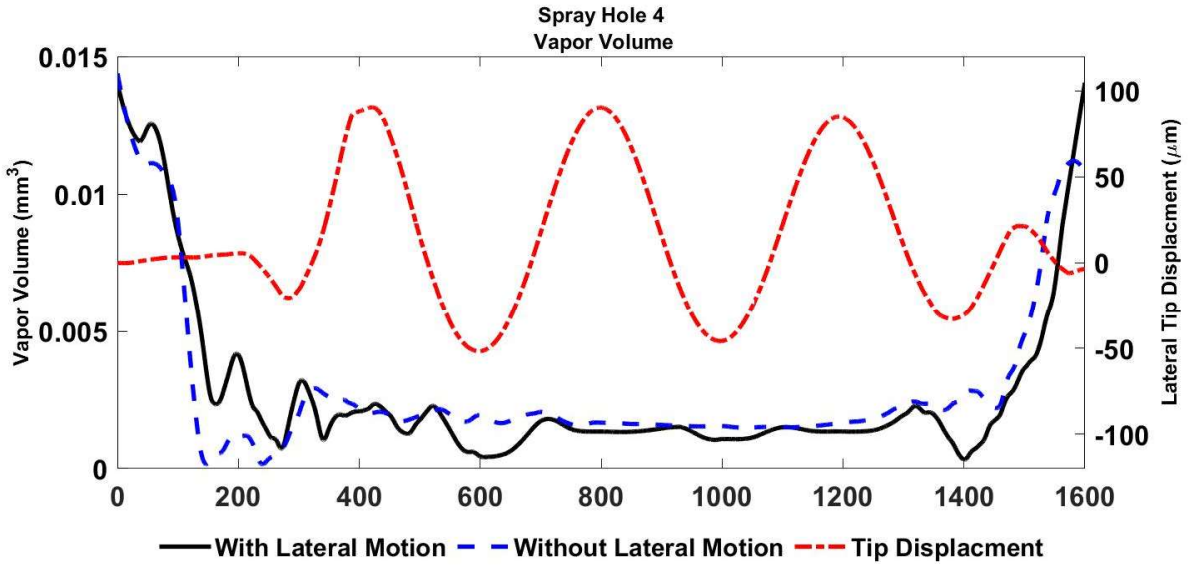
Spray Hole 4
Vapor Volume
Vapor Volume (mm3)
Lateral Tip Displacment (μm)
0.015
0.01
0.005
0
100
50
0
-50
-100
0
200
400
600
800
1000
1200
1400
1600
With Lateral Motion
Without Lateral Motion
Tip Displacment

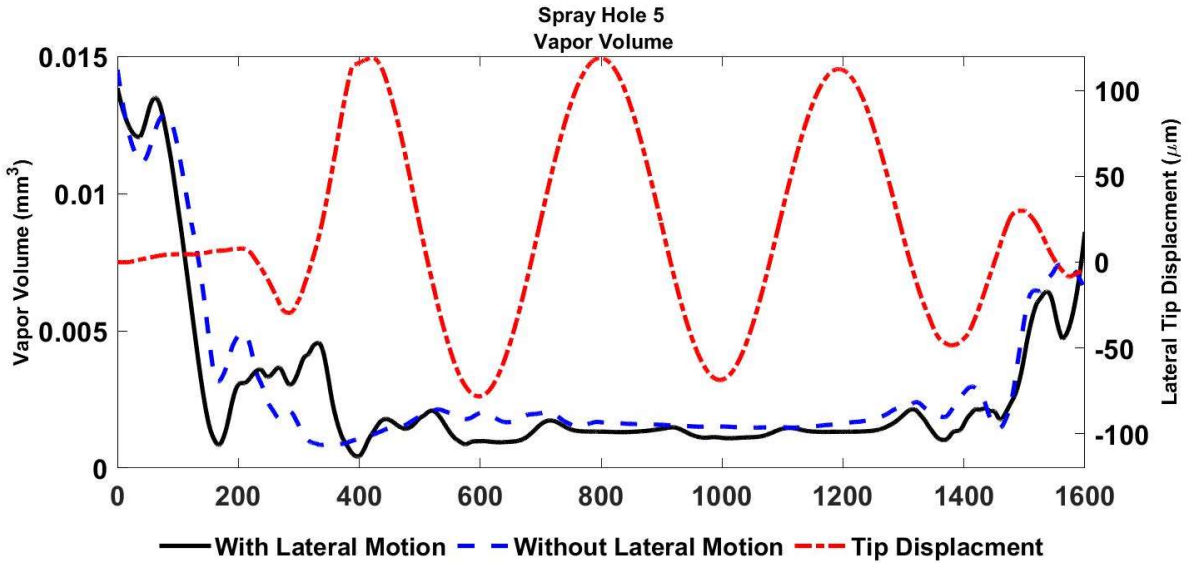
Spray Hole 5
Vapor Volume
Vapor Volume (mm3)
Lateral Tip Displacment (μm)
0.015
0.01
0.005
0
100
50
0
-50
-100
0
200
400
600
800
1000
1200
1400
1600
With Lateral Motion
Without Lateral Motion
Tip Displacment

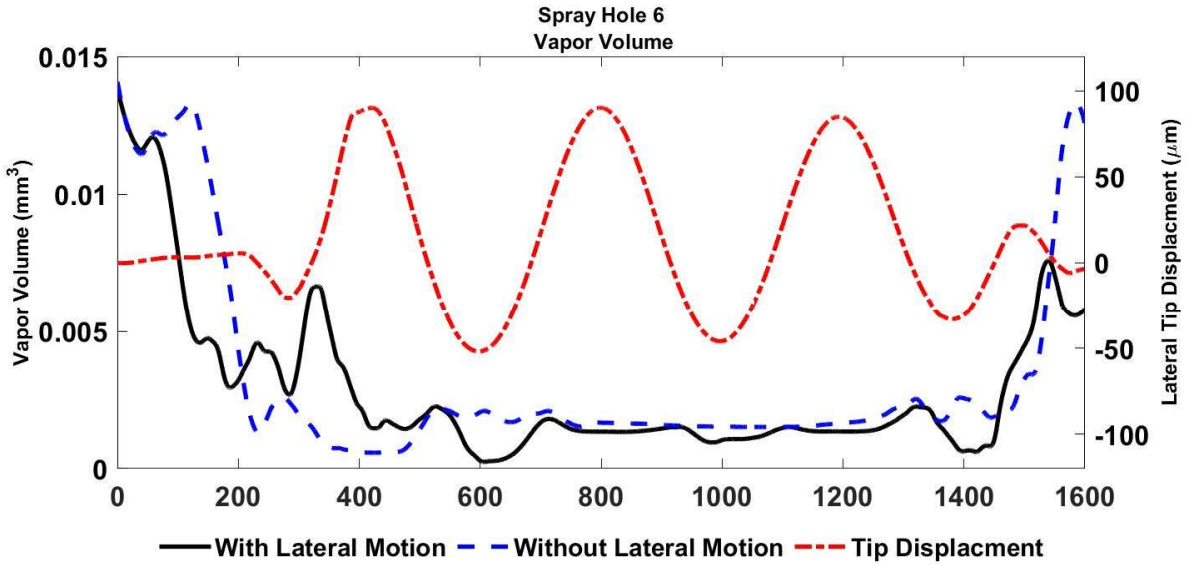
Spray Hole 6
Vapor Volume
Vapor Volume (mm3)
Lateral Tip Displacment (μm)
0.015
0.01
0.005
0
100
50
0
-50
-100
0
200
400
600
800
1000
1200
1400
1600
With Lateral Motion
Without Lateral Motion
Tip Displacment

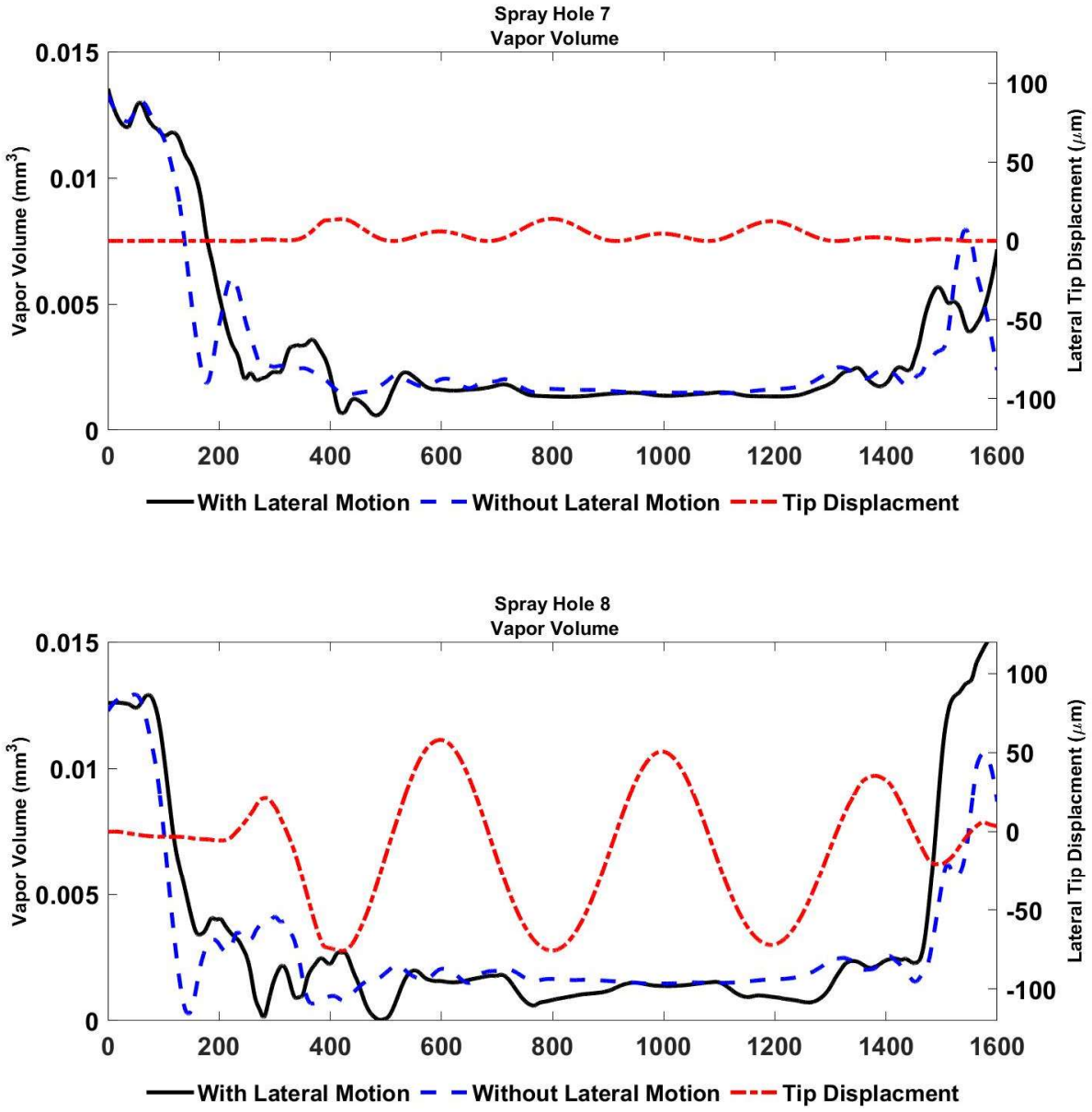

Figure 91. Spray hole vapor with and without lateral motion and the tip distance for spray holes 1-8.

The amount of vapor follows the same trend for both the simulation with and without the lateral motion. During the opening portion of the injection cycle the lateral motion plays a role in how much vapor is generated. In spray holes 1,2,5,6 the amount of vapor is decreased when the lateral motion is included. This portion of the cycle does not have a correlation between the needle motion and the vapor generated.

After the opening portion the two cases with the smallest change in the tip distance (spray holes 3 and 7) show the smallest discrepancy between the two cases which indicates that the tip distance plays role in the amount of vapor created at the highest lifts. From the other cases, at hover, the needle distance does correlate to the vapor formation. In these cases when the needle moves towards the spray hole the amount of vapor decreases. Figure 92 shows the vapor formation when the needle is centered and offset. These pictures show that the hole that the needle bends towards sees less vapor formation, although the hole that the needle bends towards sees vapor on both the top and bottom surfaces.

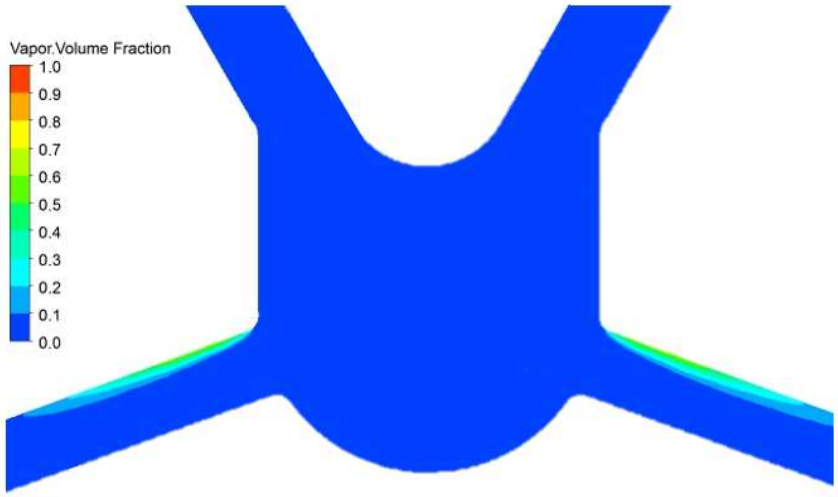

a) needle approximately centered at hover

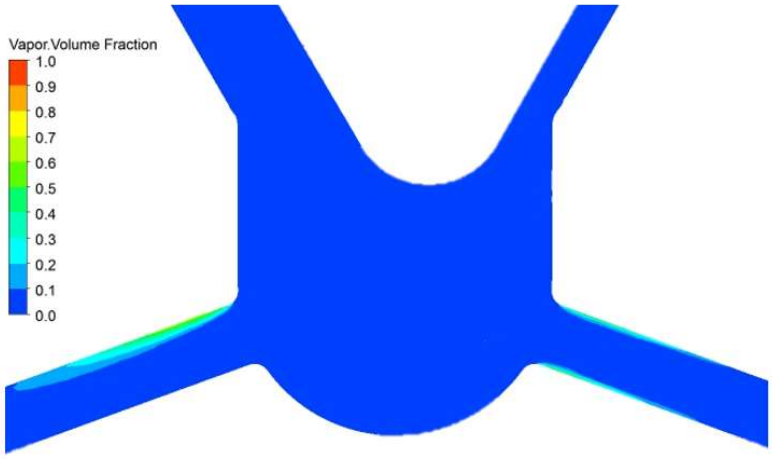

b) needle bent at hover

Figure 92. Vapor formation at hover with a) the needle centered b) offset

These results suggest that the lateral motion could be beneficial in reducing vapor formation at high lifts by reducing the amount of vapor present in the spray holes. Hovering is generally the portion of the injection cycle that has the most potential to generate cavitation damage because the pressure near the spray holes is at a maximum. During opening and closing there are changes to the vapor formation but determining if it is beneficial would require a combustion or spray simulation which is beyond the scope of this study.

XI. CONCLUISONS

This dissertation investigated the changes in the internal flow of a diesel injector across the entire lift profile and how the internal flow affects performance parameters such as the amount of vapor generated, the lifting force created and the mass flow through the outlet. Additionally, the lateral forces developed on the needle of a diesel injector with two different types of gain orifices. This dissertation showed that RANS based turbulence models prove insufficient for predicting the lateral forces as stabilities that develop in the boundary layer are dampened out and not allowed to propagate throughout the simulation domain. This paper then used a DES turbulence model to simulate the flow in dual gain orifice injector. The vortical swirling motion was shown to play a role in spray hole to spray hole mass flow delivery during the simulation. Also investigated was the influence that the transient needle motion has on the flow characteristics at hover. The FSI simulations at hover in this paper matched the amplitude and frequency of experimental studies and discovered that the forces that drive this motion are the forces on the needle shaft above the sac that arise from flow imbalances caused by the orientation of the gain orifice. The motion causes statistically insignificant changes to most of the mass flow rates and vapor volumes for the individual spray holes. The exception is the spray hole that the needle bends towards which exhibits a decrease in the amount of vapor formed. The decrease is caused by a change in the flow pattern into the spray hole, the needle bend causes fluid along the bottom of the sac to flow upward into the spray hole which decreases the height of the separated flow and limits the amount of vapor that is formed. When the opening/hover and closing motion of the injector is modeled this paper showed that the initial motion of the needle is caused by flow asymmetries that are caused by the orientation of the gain orifice. From this initial displacement larger bending forces are generated as flow is blocked by the bending of the needle at low lifts. When the flow restriction shifts from the cross-sectional area between the seating surfaces of the nozzle and needle to the spray hole outlet areas the needle bending no longer creates a flow restriction that generates enough of a pressure differential to add to the magnitude of the needle bending. At this

point the needle oscillates at the natural frequency of the needle at an offset that is related to the flow asymmetries from the gain orifice. This research has shown that the needle oscillations do not significantly contribute to the total mass of fuel injected during operation. The needle oscillations have the largest impact at low lifts and can cause large fluctuations over time for the flow through individual spray holes. However, this research has shown that although the needle motion will create fluctuations over time these fluctuations will even out the flow between individual spray holes. The flow per spray hole is more consistent in simulations where the needle was allowed to bend than simulations without bending because the needle motion reduced the asymmetries caused by the orientation of the gain orifice. This research has also shown that the bending of the needle has an impact on the vapor generated during injection, but the needle displacement tends to reduce the vapor generated which is beneficial to part robustness.

REFERENCES

[1] Lindstrom, M., 2009, "Injector Nozzle Hole Parameters and their Influence on Real DI DIesel Performance," Licentiate Thesis, Sweden, Royal Institute of Technology.
[2] Montgomery, D., Chan,M. , Chang, C. ,Farrell,P., et al., 1996, "Effect of Injector Nozzle Hole Size and Number on Spray Characteristics and the Performance of a Heavy Duty D.I. Diesel Engine," SAE Technical Paper 962002.
[3] Flynn, P., Durret, R., Hunter, G., Loye, A., Akinyemi, O., Dec, J., Westbrook, C., 1999, "Diesel Combustion: An Integrated View Combining Laser Diagnostics, Chemical Kinetics, and Empirical Validation," SAE Technical Paper 1999-01-0509.
[4] Vijayakumar, T., Rajagopal,T. K. R., and Kasianantham, N.,, 2011, "Numerical Investigation on the Effect of Injection Pressure on the Internal Flow Characteristics for Diethyl ether, Dimethyl Ether and Diesel Fuel Injectors using CFD," J. Thermal Science, 15(4), pp. 1123-1130.
[5] Yanagihara, H., Sato, Y., and Mizuta, J. i., 1997, "A Study of DI Diesel Combustion under Uniform Higher-Dispersed Mixture Formation," JSAE Review, 18(4), pp. 361-367.
[6] Morgan, R., Wray, J., Kennaird, D., Crua, C. et al., 2001, "The Influence of Injector Parameters on the Formation and Break-Up of a Diesel Spray," SAE Technical Paper 2001-01-0529.
[7] Benajes, J., Payri, R., Molina, S., and Soare, V., 2005, "Investigation of the Influence of Injection Rate Shaping on the Spray Characteristics in a Diesel Common Rail System Equipped with a Piston Amplifier," Journal of Fluids Engineering, 127(6), pp. 1102-1110.
[8] Benajes, J., Pastor, J. V., Payri, R., and Plazas, A. H., 2004, "Analysis of the Influence of Diesel Nozzle Geometry in the Injection Rate Characteristic," Journal of Fluids Engineering, 126(1), pp. 63-71.
[9] Kastengren, A. L., Powell, C. F., Riedel, T., Cheong, S. K., Im, K. S., Liu, X., Wang, Y. J., and Wang, J., 2008, "Nozzle Geometry and Injection Duration Effects on Diesel Sprays Measured by X-Ray Radiography," Journal of Fluids Engineering, 130(4), pp. 041301-041301.
[10] Chaves, H., Knapp, M., Kubitzek, A., Obermeier, F. et al., 1995, "Experimental Study of Cavitation in the Nozzle Hole of Diesel Injectors Using Transparent Nozzles," SAE Technical Paper 950290.
[11] Hiroyasu, H., 2000, "Spray Breakup Mechanism from The Hole-Type Nozzle and its Applications," Atomization and Sprays, 10(3-5), pp. 511-527.
[12] He, L., and Ruiz, F., 1995, "Effect of Cavitation on Flow and Turbulence in Plain Orifices for High-Speed Atomization " Atomization and Sprays, 5(6), pp. 569-584.
[13] Baritaud, T., Heinze, T., and Le Coz, J., 1994, "Spray and Self-Ignition Visualization in a DI Diesel Engine," SAE Technical Paper 940681.
[14] Bruneaux, G., Verhoeven, D., and Baritaud, T., 1999, "High Pressure Diesel Spray and Combustion Visualization in a Transparent Model Diesel Engine," SAE Technical Paper 1999-01-3648.

[15] Dec, J., 1997, "A Conceptual Model of DI Diesel Combustion Based on Laser-Sheet Imaging," SAE Technical Paper 970873.
[16] Arcoumanis, C., Flora, H., Gavaises, M., and Badami, M., 2000, "Cavitation in Real-Size Multi-Hole Diesel Injector Nozzles," SAE Technical Paper 2000-01-1249.
[17] Carey, V. P., 1992, *Liquid-Vapor Phase Change Phenomena*, Hemoshre Publishing Corporation.
[18] Abraham, F. F., 1974, *Homogeneous Nucleation Theory*, Academic Press.
[19] Knapp, R. T., Daily J.W., Hammit F.G., 1970, *Cavitation*, McGraw Hill Book Company.
[20] Brennan, C. E., 1995, *Cavitation and Bubble Dynamics*, Oxford University Press.
[21] Badock C, W. R., Tropea C., "The Influence of Hydro-Grinding on Cavitation Inside a Diesel Injection Nozzle and Primary Break-Up Under Unsteady Pressure Conditions," Proc. fifteenth ILASS-Europe 99.
[22] Ohrn, T. R., Senser, D. W., and Lefebvre, A. H., 1991, "Geometrical Effects on Discharge Coefficients for Plain-Orifice Atomizers," Atomization and Sprays, 1(2), pp. 137-153.
[23] Payri, R., Margot, X., and Salvador, F., 2002, "A Numerical Study of the Influence of Diesel Nozzle Geometry on the Inner Cavitating Flow," SAE Technical Paper 2002-01-0215.
[24] Nurick, W. H., 1976, "Orifice Cavitation and Its Effect on Spray Mixing," ASME J Fluids Eng, 98(4), pp. 681-687.
[25] Macian, V., Payri, R., Margot, X., and Salvador, F. J., 2003, "A Cfd Analysis of the Influence of Diesel Nozzle Geometry on the Inception of Cavitation," Atomization and Sprays, 13(5&6), pp. 579-604.
[26] Zhang, Z., 1999, "Compromise Orifice Geometry to Minimize Pressure Drop," Journal of Hydraulic Engineering, 125(11).
[27] Gavaises, M. a. A., A., 2006, "Cavitation Inside Multi-hole Injectors for Large Diesel Engines and Its Effect on the Near-nozzle Spray Structure," SAE Technical Paper 2006-01-1114.
[28] Som, S., El-Hannouny, E. M., Longman, D. E., and Aggarwal, S. K., 2010, "Investigation of Nozzle Flow and Cavitation Characteristics in a Diesel Injector," Journal of Engineering for Gas Turbines and Power, 132(4), pp. 042802-042802.
[29] Bunnell, R. A., and Heister, S. D., 1999, "Three-Dimensional Unsteady Simulation of Cavitating Flows in Injector Passages," Journal of Fluids Engineering, 122(4), pp. 791-797.
[30] Pan, Y., and Suga, K., 2006, "A Numerical Study on the Breakup Process of Laminar LiquidJets Into a Gas," Physics of Fluids, 18(5), p. 052101.
[31] Powell, C. F., Kastengren, A. L., Liu, Z., and Fezzaa, K., 2010, "The Effects of Diesel Injector Needle Motion on Spray Structure," Journal of Engineering for Gas Turbines and Power, 133(1).
[32] Kilic A., S. L., Tschöke H., 2006, "Influence of Nozzle Parameters on Single Jet Flow Quantities of Multi-Hole Diesel Injection Nozzles," SAE Technical Paper 2006-01-1983.
[33] Battistoni, M., Xue, Q., Som, S., and Pomraning, E.,, 2014, ""Effect of Off-Axis Needle Motion on Internal Nozzle and Near Exit Flow in a Multi-Hole Diesel Injector,"" SAE Int. J. Fuels Lubr., 7(1), pp. 167-182.

[34] Salvador, F. J., Martínez-López, J., Romero, J. V., and Roselló, M. D., 2013, "Study of the Influence of the Needle Eccentricity on the Internal Flow in Diesel Injector Nozzles By Computational Fluid Dynamics Calculations," International Journal of Computer Mathematics, 91(1), pp. 24-31.
[35] Schmidt, D. P., 1997, "Cavitation in Diesel Fuel Injector Nozzles," University of Wisconsin-Madison.
[36] Giannadakis, E., Gavaises, M., and Arcoumanis, C., , 2008, "Modelling of Cavitation in Diesel Injector Nozzles," ASME J Fluids Eng, 616, pp. 153-193.
[37] Constantinescu, G. S., and Squires, K. D., 2003, "LES and DES Investigations of Turbulent Flow over a Sphere at Re = 10,000," Flow, Turbulence and Combustion, 70(1-4), pp. 267-298.
[38] Constantinescu, G., Chapelet, M., and Squires, K., 2003, "Turbulence Modeling Applied to Flow over a Sphere," AIAA Journal, 41(9), pp. 1733-1742.
[39] Payri, R., Tormos, B., Gimeno, J., and Bracho, G., 2010, "The potential of Large Eddy Simulation (LES) code for the modeling of flow in diesel injectors," Mathematical and Computer Modelling, 52(7–8), pp. 1151-1160.
[40] M. Darwish, F. M. B. S., 2001, "A UNIFIED FORMULATION OF THE SEGREGATED CLASS OF ALGORITHMS FOR MULTIFLUID FLOW AT ALL SPEEDS," Numerical Heat Transfer, Part B: Fundamentals, 40(2), pp. 99-137.
[41] Raithby, J. P. V. D. a. G. D., 1984, "Enhancements of the SIMPLE Method for Predicting Incompressible Fluid Flows," Numerical Heat Transfer, 7(2).
[42] S.V. Patankar, a. D. B. S., 1972, "A Calculation Procedure for Heat, Mass and Momentum Transfer in Three-Dimensional Parabolic Flows," International Journal of Heat and Mass Transfer, 15, pp. 1787-1806.
[43] Caretto, L. S., Gosman, A. D., Patankar, S. V., and Spalding, D. B., 1973, "Two calculation procedures for steady, three-dimensional flows with recirculation," Proceedings of the Third International Conference on Numerical Methods in Fluid Mechanics, H. Cabannes, and R. Temam, eds., Springer Berlin Heidelberg, pp. 60-68.
[44] Rhie, C. M., and Chow, W. L., 1983, "Numerical study of the turbulent flow past an airfoil with trailing edge separation," AIAA Journal, 21(11), pp. 1525-1532.
[45] Zang, Y., Street, R. L., and Koseff, J. R., 1994, "A Non-staggered Grid, Fractional Step Method for Time-Dependent Incompressible Navier-Stokes Equations in Curvilinear Coordinates," Journal of Computational Physics, 114(1), pp. 18-33.
[46] Van Doormaal, J. P., and Raithby, G. D., 1984, "Enhancements of the Simple Method for Predicting Incompressible Fluid Flows," Numerical Heat Transfer, 7(2), pp. 147-163.
[47] Jang, D. S., Jetli, R., and Acharya, S., 1986, "COMPARISON OF THE PISO, SIMPLER, AND SIMPLEC ALGORITHMS FOR THE TREATMENT OF THE PRESSURE-VELOCITY COUPLING IN STEADY FLOW PROBLEMS," Numerical Heat Transfer, 10(3), pp. 209-228.
[48] Inc, A., 2014, *ANSYS FLUENT Theory Guide*.
[49] Agency, J. A. E., 2009, "Cavitation and Boiling,"http://www.aero.jaxa.jp/eng/publication/magazine/sora/2005_no09/ss2005no09_01.html.
[50] Alajbegovic, A., Grogger, H.A., Philipp, H, 1999, "Calculation of transient cavitation in nozzle using the two-fluid model," Proc. ILASS-Americas'99 Annual Conf.

[51] Dellanoy, Y., and Kueny, J.L, 1990, "Two phase flow approach in unsteady cavitation modelling," ASME Cavitation and Multiphase Forum, ASME FED, pp. 153-158.
[52] Avva, R. K., Singhal, A., and Gibson, D.H., 1995, " An enthalpy based model of cavitation," ASME.
[53] Dumont, N., Simonin, O., and Habchi, C., 2001, "Numerical simulation of cavitatingn flows in Diesel injectors by a homogeneous equilibrium modelling approach," 4 th Int. Symposium on Cavitation.
[54] Wallis, G. B., 1969, One-Dimensional Two=Phase Flow, mcGraw-Hill.
[55] Chen, Y. a. H., S.D. , 1995, " Two-phase modelling of cavitated flows," Computational Fluids, 24(7), pp. 799-806.
[56] Kunz, R. F., Boger, D.A., Stinebring, D.R., et al., 2000, " A preconditioned Navier-Stokes method for two-phase flows with application to cavitation prediction.," Computer and Fluids, 29, pp. 849-875.
[57] Ahuja, V., Hosangadi, A. and Arunajatesan, S., 2001, "Simulations of caviting flows using hybrid unstructured meshes," Journal of Fluid Engineering, 123, pp. 331-339.
[58] Yuan, W., Sauer, J., and Schnerr, G. H., 2001, "Modeling and computation of unsteady cavitation flows in injection nozzles," Mécanique & Industries, 2(5), pp. 383-394.
[59] Singhal A.K., A., M., LI H.Y., and Y.J., 2002, "Mathmatical Basis and Validation of the Full Cavitation Model," Journal of Fluid Engineering, 124, pp. 617-624.
[60] Sauer, J., 2000, "Unsteady Cavitating Flows - A New Model Based on Front Capturing (VOF) and Bubble Dynamics," Karlsruher Institut for Technologies.
[61] Rayleigh, L., 1917, "On the Pressure Devoloped in a Liquid During the Collapse of a Spherical Cavity," Philosophical Magazine Series 6, 34(200), pp. 94-98.
[62] Schneer, G. H. a. S., J., 2001, " Physical and numerical modeling of unsteady cavitation dynamics," 4th International Conference on Multiphase FlowsNew Orleans, United States.
[63] Kozubková, M., Rautová, J., and Bojko, M., 2012, "Mathematical Model of Cavitation and Modelling of Fluid Flow in Cone," Procedia Engineering, 39(0), pp. 9-18.
[64] Bily D., a. K., M.,, 2011, "Dynamics Behaviour of the Cavitation Field," Journal of Applied Science in the Thermodynamics and Fluid Mechanics, 9(2).
[65] Shih T., L. W., Shabbir A., Yang Z., and Zhu J., 1995, "A new k-epsilon eddy viscosity model for high reynolds number turbulent flows," Journal of Computers and Fluids.
[66] Jones, W. P., and Launder, B. E., 1973, "The calculation of low-Reynolds-number phenomena with a two-equation model of turbulence," International Journal of Heat and Mass Transfer, 16(6), pp. 1119-1130.
[67] Launder, B. E., and Spalding, D. B., 1974, "The numerical computation of turbulent flows," Computer Methods in Applied Mechanics and Engineering, 3(2), pp. 269-289.
[68] Shih, T. H., and Lumley, J. L., 1993, "Remarks on turbulent constitutive relations," Mathematical and Computer Modelling, 18(2), pp. 9-16.
[69] Carruthers, J. C. R. H. a. D. J., 1990, "Rapid Distortion Theory and the ‘Problems’ of Turbulence," Journal of Fluid Mechanics, 212, pp. 497-532.
[70] Speziale, C., Abid, R., and Durbin, P., 1994, "On the realizability of reynolds stress turbulence closures," J Sci Comput, 9(4), pp. 369-403.
[71] Lumley, J. L., 1978, "Computational Modeling of Turbulent Flows," Advanced Applied Mechanics, 18, pp. 124-176.

[72] Schumann, U., 1977, "Realizability of Reynolds Stress Turbulence Models," Physics of Fluids, 20, pp. 721-725.
[73] Smagorinsky, J., 1963, "General Circulation Experiments with the Primitive Equations," Monthly Weather Review, 91(3), pp. 99-164.
[74] Spalart, P. R., Deck, S., Shur, M. L., Squires, K. D., Strelets, M. K., and Travin, A., 2006, "A New Version of Detached-eddy Simulation, Resistant to Ambiguous Grid Densities," Theoret. Comput. Fluid Dynamics, 20(3), pp. 181-195.
[75] Spalart, P., 2001, "Young Person's Guide to Detached-Eddy Simulation Grids," NASA/CR-2001-211032.
[76] Hilber, H., Thomas, J., Hughes, R., Taylor, R., 1977, "Improved Numerical Dissipation For Time Integration Algorithims in Structural Synamics," Earthquake Engineering and Structural Dynamics, 5, pp. 283-292.
[77] Newmark, N. M., 1959, "A method of computation for structural dynamics," Journal of the Engineering Mechanics Division, 85.
[78] Spears, R. E., Jensen, S.R>, 2009, "Title."
[79] Farhat, C., Lesoinne, M., and Le Tallec, P., 1998, "Load and motion transfer algorithms for fluid/structure interaction problems with non-matching discrete interfaces: Momentum and energy conservation, optimal discretization and application to aeroelasticity," Computer Methods in Applied Mechanics and Engineering, 157(1–2), pp. 95-114.
[80] Beckert, A., and Wendland, H., 2001, "Multivariate interpolation for fluid-structure-interaction problems using radial basis functions," Aerospace Science and Technology, 5(2), pp. 125-134.
[81] de Boer, A., van Zuijlen, A. H., and Bijl, H., 2007, "Review of coupling methods for non-matching meshes," Computer Methods in Applied Mechanics and Engineering, 196(8), pp. 1515-1525.
[82] Thévenza, P., Blu, T., Unser M., 2000, "Interpolation revisisted," IEEE Trans. Med. Imaging, 19(17), pp. 739-758.
[83] Cebral, J. R., and Lohner, R., 1997, "Conservative Load Projection and Tracking for Fluid-Structure Problems," AIAA Journal, 35(4), pp. 687-692.
[84] Smith, M., Cesnik, C., and Hodges, D., 2000, "Evaluation of Some Data Transfer Algorithms for Noncontiguous Meshes," Journal of Aerospace Engineering, 13(2), pp. 52-58.
[85] Travin, A., Shur, M., Strelets, M., and Spalart, P., 2000, "Detached-Eddy Simulations Past a Circular Cylinder," Flow, Turbulence and Combustion, 63(1-4), pp. 293-313.
[86] Spalart, P. R., 2008, "Detached-Eddy Simulation," Annual Review of Fluid Mechanics, 41(1), pp. 181-202.
[87] Clarke, D. A. J. a. D. B., 2008, "Simulation of Flow Past a Sphere using the Fluent Code," Maritime Platforms Division, Defence Sceience and Technology Organisation, DSTRO-TR-2232.
[88] Kim, S. E., 2004, "Large Eddy Simulation Using Unstructured Meshes and Dynamic Subgrid Scale Turbulance Models," 34th AIAA Fluid Dynamics Conference and ExhibitPortland Oreggon.
[89] E., A., 1974, "Vortex Shedding From Spheres," Journal of Fluid Mechanics, 62, pp. 209-221.

[90] Jeong, J., and Hussain, F., 1995, "On the identification of a vortex," Journal of Fluid Mechanics, 285, pp. 69-94.
[91] Kastengren, A. L., Tilocco, F.Z., Powell, C.F., Manin, J., Pickett,, and L.M., P., R., and Bazyn, T., 2013, "Engine combustion network (ECN):
measurements of nozzle geometry and hydraulic behavior," Atomization and Sprays, 22(12), pp. 1011-1052.
[92] Kastengren, A., Powell, C. F., Liu, Z., Fezzaa, K., and Wang, J., "High-speed x-ray imaging of diesel injector motion," Proc. Proc. of the
ASME Internal Combustion Engine Division Spring Technical
Conference.
[93] Battistoni, M., Xue, Q., Som, S., and Pomraning, E.,, 2014, "Effect of Off-Axis Needle Motion on Internal Nozzle and Near Exit Flow in a Multi-Hole Diesel Injector," SAE Int. J. Fuels Lubr., 7(1), pp. 167-182.

APPENDICES

C_1,C_2	Model closure coefficient
D	Diameter
$\vec{F}$	External body forces
Fe, Fc	Evaporation, condensation coefficient
G_k	Generation of turbulence kinetic energy
I	Turbulence intensity
k	Turbulent kinetic energy
K	K factor
L	Length
M_t	Turbulent Mach number
P	Pressure
P_v	Vaporization Pressure
R	Mass transfer rate
R_B	Bubble radius
Re	Reynolds number
S	Source term in the flow field
t	Time
$\vec{u}$	Velocity vector
x	spatial coordinate
Y_m	dilation dissipation term
α	Volume fraction
α_{nuc}	nucleation Volume fraction
ε	turbulent dissipation
ρ	Density
σ	Stress tensor from molecular viscosity
σ_k, σ_ε	Turbulent Prandtl number for k,ε

τ Subgrid scale stress

μ Viscosity

μ_t Turbulent eddy viscosity

Subscripts

L liquid

i,j,k directional vector component

K Single phase of the mixture

M Mixture

v Vapor

CURRICULUM VITA

NAME: Russell Prater

ADDRESS: 3395 Edgefield Place
Columbus, Indiana, 47203

DOB: Columbus, Ohio – December 28, 1987

EDUCATION
& TRAINING:

B.S., Mechanical Engineering
University of Louisville
2005-2011

M.S. Mechanical Engineering
University of Louisville
2005-2011

Ph.D., Mechanical Engineering
University of Louisville
2011-2022

PUBLICATIONS: DES Simulation of Asymmetrical Flow in a High-Pressure Diesel Injector